EFFICIENT NUMERICAL ANALYSIS OF PERIODIC STRUCTURES USING THE THEORY OF CHARACTERISTIC MODES

A THESIS SUBMITTED TO
THE GRADUATE SCHOOL OF NATURAL AND APPLIED SCIENCES
OF
MIDDLE EAST TECHNICAL UNIVERSITY

BY

YİĞİT HAYKIR

IN PARTIAL FULFILLMENT OF THE REQUIREMENTS
FOR
THE DEGREE OF DOCTOR OF PHILOSOPHY
IN
ELECTRICAL AND ELECTRONICS ENGINEERING

DECEMBER 2022

Approval of the thesis:

EFFICIENT NUMERICAL ANALYSIS OF PERIODIC STRUCTURES USING THE THEORY OF CHARACTERISTIC MODES

submitted by **YİĞİT HAYKIR** in partial fulfillment of the requirements for the degree of **Doctor of Philosophy in Electrical and Electronics Engineering Department, Middle East Technical University** by,

Prof. Dr. Halil Kalıpçılar
Dean, Graduate School of **Natural and Applied Sciences** ________________

Prof. Dr. İlkay Ulusoy
Head of Department, **Electrical and Electronics Engineering** ________________

Prof. Dr. Özlem Aydın Çivi
Supervisor, **Electrical and Electronics Engineering, METU** ________________

Examining Committee Members:

Prof. Dr. Seyit Sencer Koç
Electrical and Electronics Engineering, METU ________________

Prof. Dr. Özlem Aydın Çivi
Electrical and Electronics Engineering, METU ________________

Assoc. Prof. Dr. Lale Alatan
Electrical and Electronics Engineering, METU ________________

Prof. Dr. Vakur Behçet Ertürk
Electrical and Electronics Engineering, Bilkent University ________________

Prof. Dr. Özlem Özgün
Electrical and Electronics Engineering, Hacettepe University ________________

Date: 02.12.2022

I hereby declare that all information in this document has been obtained and presented in accordance with academic rules and ethical conduct. I also declare that, as required by these rules and conduct, I have fully cited and referenced all material and results that are not original to this work.

Name, Surname: Yiğit Haykır

Signature :

ABSTRACT

EFFICIENT NUMERICAL ANALYSIS OF PERIODIC STRUCTURES USING THE THEORY OF CHARACTERISTIC MODES

Haykır, Yiğit
Doctor of Philosophy, Electrical and Electronic Engineering
Supervisor : Prof. Dr. Özlem Aydın Çivi

December 2022, 154 pages

The characteristic mode analysis has become a popular and versatile tool in antenna design and analysis. This analysis provides useful information about radiation characteristics of scatterers and offers physical insight into the radiation problem. Hence it can also be exploited in the solution of periodic structures. In this work, an integral based simulation program has been developed to perform the modal analysis of periodic structures. This dissertation consists of three interrelated parts. In the first part, the characteristic mode analysis is extended to the periodic unit cell solution. This analysis yields distinct perspective to the analysis of the reflectarray problem. In the second part, the resonance behavior of the mode of interest is modified by applying continuous load distribution over the unit cell element. However since such loading is hard to realize, an approach has been developed to reduce the load distribution on the ring-type unit cell element into two discrete loads. Subsequently, a novel method is introduced that allows to find the reactive load values in advance that shift the reflection band of the ring-type frequency selective surface element to desired frequency. Thus, the need for optimization-based methods that increase the solution cost has been eliminated. In the last part, the finite array solution is evaluated in which characteristic modes are used as macro basis functions. Afterwards, a multilevel matrix reduction method is presented for the array of differently sized elements using characteristic modes. This thesis work leads efficient and original analysis of large periodic structures using the theory of characteristic modes.

Keywords: Characteristic mode analysis, periodic unit cell, reactive loading, macro basis functions.

ÖZ

PERİYODİK YAPILARIN KARAKTERİSTİK MODLAR TEORİSİNİ KULLANARAK VERİMLİ NÜMERİK ANALİZİ

Haykır, Yiğit
Doktora, Elektrik ve Elektronik Mühendisliği
Tez Yöneticisi: Prof. Dr. Özlem Aydın Çivi

Aralık 2022, 154 sayfa

Karakteristik mod analizi, anten tasarımı ve analizinde popüler ve çok yönlü bir araç haline gelmiştir. Bu analiz, saçıcıların ışıma özellikleri hakkında faydalı bilgiler sağlamakta ve ışıma problemine fiziksel bir bakış açısı sunmaktadır. Dolayısıyla periyodik yapıların çözümünde de kullanılabilir. Bu çalışmada, periyodik yapıların modal analizini gerçekleştirmek için integral tabanlı bir simülasyon programı geliştirilmiştir. Bu tez birbiriyle ilişkili üç bölümden oluşmaktadır. İlk bölümde, karakteristik mod analizi periyodik birim hücre çözümüne genişletilmektedir. Bu analiz, yansıtmalı dizi probleminin analizine farklı bir bakış açısı getirmektedir. İkinci bölümde ilgili modun rezonans davranışı, birim hücre elemanı üzerinde sürekli yük dağılımı uygulanarak değiştirilir. Ancak böyle bir yüklemenin gerçekleştirilmesi zor olduğundan, halka tipi birim hücre elemanı üzerindeki yük dağılımını iki ayrı yüke indirgemek için bir yaklaşım geliştirilmiştir. Sonrasında ise halka tipi frekans seçici yüzey elemanının yansıma bandını istenen frekansa kaydıran reaktif yük değerlerinin önceden bulunmasını sağlayan yeni bir yöntem tanıtılmıştır. Böylece çözüm maliyetini arttıran optimizasyon tabanlı yöntemlere olan ihtiyaç giderilmiştir. Son bölümde ise karakteristik modların makro tabanlı fonksiyonlar olarak kullanıldığı sonlu dizi çözümü değerlendirilmiştir. Daha sonra karakteristik modlar kullanılarak farklı büyüklükteki elemanlar dizisi için çok seviyeli bir matris indirgeme yöntemi sunulmuştur. Bu tez çalışması, karakteristik modlar teorisini kullanarak büyük periyodik yapıların verimli ve özgün analizine öncülük etmektedir.

Anahtar Kelimeler: Karakteristik mod analizi, periyodik birim hücre, reaktif yükleme, makro temel fonksiyonlar.

Dedicated to my family.

ACKNOWLEDGMENTS

I would like to thank Prof. Dr. Özlem Aydın Çivi for the supervision of the thesis. I would also like to thank Prof. Dr. Sencer Koç for his advices throughout my thesis monitoring period.

I would like to express my sincere appreciation to Prof. Dr. Vakur Ertürk and Assoc. Prof. Dr. Lale Alatan for providing supportive feedbacks and contributing to the quality of my thesis.

I would like to express my profound gratitude to Prof. Dr. Adnan Köksal, who was my advisor during my MSc studies and also participated in my thesis committee until his retirement. He played a major role in my academic development and encouraged me to pursue this doctorate.

It was a challenging process to carry out a doctoral study while working full time. In this respect, I would like to express my sincere appreciation to Prof. Dr. Şimşek Demir. He gave me the opportunity to develop myself as an RF design engineer and provided an efficient working environment that also enabled me to carry out my academic studies. I am very grateful for his support, confidence and friendly encouragement.

I would also like to acknowledge my gratitude to my colleagues in PRF-ARGE. I especially want to thank Habib Özer Öz for his profound support and valuable friendship. I would also like to thank Fatih Erdem, Aydoğa Kallem and Mükremin Barış Şahin for their exchange of ideas at work.

Finally, I would like to express my deepest gratitude to my parents for their endless love and support.

TABLE OF CONTENTS

CHAPTERS

LIST OF TABLES

TABLES

LIST OF FIGURES

FIGURES

LIST OF ABBREVIATIONS

2D	2 Dimensional
3D	3 Dimensional
EFIE	Electric Field Integral Equation
MoM	Method of Moments
PEC	Perfectly Electric Conductor
RWG	Rao-Wilton-Glisson
CMA	Characteristic Mode Analysis
CM	Characteristic Mode
MS	Modal Significance
NCM	Network Characteristic Modes
CBFM	Characteristic Basis Function Method
FSS	Frequency Selective Surface
PBG	Photonic Band Gap
PGF	Periodic Green’s Function
FMM	Fast Multipole Method
MLFMA	Multilevel Fast Multipole Method
AIM	Adaptive Integral Method
ACA	Adaptive Cross Approximation
CBF	Characteristic Basis Function
MBF	Macro Basis Function
SVD	Singular Value Decomposition
MLCBFM	Multilevel Characteristic Basis Function Method

CHAPTER 1

INTRODUCTION

Large periodic arrays are utilized in many applications. Especially optical filters including frequency selective surface (FSS) [1] and photonic band gap (PBG) [2] structures have become popular research topics. In these applications, the shape of the unit cell element and its periodicity is determined such that they allow transmission and reflection of electromagnetic waves only at certain frequencies. Similarly metamaterial absorbers and artificial impedance surfaces such as mushroom-type texture surfaces also utilize arrays of 2D periodic elements. In recent years, reflectarray antennas become very popular due to their advantages over phased arrays and reflector antennas [3]. Unlike phased arrays, reflectarray antennas do not require a complicated and lossy feeding network. Moreover, they are low profile, light and easy to fabricate antennas which are also advantageous features compared to the reflector antenna. In the reflectarray design, certain element parameters are modified so that the reflected electric field provides desired reflection phase response. Hence, the overall phase distribution on the aperture can yield desired radiation behavior.

Since there are many applications of periodic structures, the analysis of the radiation and scattering from periodic elements has become an important area of the computational electromagnetics. Due to the increasing number of elements in large periodic arrays, unit cell solution is adopted to reduce the computational burden. Hence solution of large arrays of periodic elements can be performed quickly and efficiently by defining periodic boundary conditions on the edges of the unit cell. Unit cell solution is also needed in the design of reflectarray antennas since the reflection phase of each element is obtained from the solution of each element inside the periodic boundary. Periodic boundary conditions can be applied for different computational methods such as finite element method and finite difference. Hybrid method of finite element boundary integrals (FEBI) [4] incorporates Floquet modes into the finite element solution and implements integral solutions on top and bottom sides of the unit cell. Nevertheless, use of periodic Green's function in the context of the method of moment (MoM) [5] provides simple, and yet efficient solution for the unit cell problem.

Method of moments is a versatile method for the solution of conducting elements within the unit cell as well as at open boundaries. Especially for arbitrary geometries, Rao-Wilton-Glisson (RWG) [6] functions along with triangular discretization on the conducting surface pave the way for flexible and accurate solutions. The periodic Green's function (PGF) can be utilized in the solution of unit cell element within the MoM. Since a large number of terms that come from the periodic Green's function must be included into the integral equation, Ewald's transformation [7] can be implemented to reduce the computational burden.

In recent years, characteristic mode analysis has also become very popular tool in the solution of antenna and scattering problem. In analysis of characteristic modes within the method of moments, applying the generalized eigenvalue equation over the impedance matrix yields a set of orthogonal modes [8, 9]. These modes yield physical insight about the radiation and scattering behavior of conducting and dielectric bodies. They can be excited by different illuminations and feedings. Besides that, the theory of the characteristic modes has also emerged as a method that facilitates the use of reactive loads and calculates loading values to alter radiation characteristics of an antenna [10]. However, since this method suggests using as many loads as the number of basis functions, it has evolved into a method that utilizes network characteristic modes (NCM) by turning the antenna problem into a network problem [11–14].

Moreover, the characteristic modes can also be utilized as macro basis functions (MBFs) over large scattering bodies as well as finite array structures. Macro basis function approach provides fast solutions of large structures by decomposing domains into large subdomains. Using basis functions over each subdomain, the number of unknowns can be reduced which paves the way for cost and time efficient integral solutions [15]. The characteristic basis function method (CBFM) [16, 17] is a well-known approach that employs MBFs, also known as characteristic basis functions (CBFs) to achieve matrix reduction. Within this method, finite array structures can be solved by expanding basis functions over the array elements. To reduce the number of unknowns even further, the multilevel CBFM (MLCBFM) has also been suggested [18, 19]. It utilizes hierarchical partitioning to achieve faster solutions in electrically very large structures.

The characteristic modes make very efficient macro basis functions over finite array elements due to their excitation-free nature [20]. Especially in the problem of finite arrays consisting of identical elements, the characteristic modes that obtained over a single and isolated array element can be applied over all array elements regardless of the excitation. In recent years, characteristic modes have been utilized as macro basis functions in the solution of the reflectarray, and it has been shown that the same modes can be used on differently sized elements [21].

In summary, the characteristic mode analysis can become very useful in the unit cell solution as well as the solution of finite array. The physical insight that characteristic mode analysis brings to the antenna and scattering problem can be extended to the unit cell problem. Besides that, the modal approach to obtain reactive load matrix on antenna elements can be utilized in the unit cell problem to achieve shift in reflection and transmission band of the unit cell element. Moreover in the finite array problem, the characteristic modes can be exploited as macro basis functions to speed up the numerical analysis.

1.1 Motivation and Problem Definition

The characteristic modes yield orthogonal basis functions that model the surface current in the radiation and scattering problem. Moreover they can be expressed in terms of other modal expansion functions. For instance spherical modes in dipole and loop element can be modeled using characteristic modes [22] and similarly, the cavity modes in a microstrip patch element can be associated with the characteristic modes [23]. However since characteristic mode analysis of the unit cell element has not been fully investigated, the relationship between the characteristic modes and the

Floquet modes of the unit cell element has remained unclear. In fact, the characteristic modes of the unit cell element would yield the reflection and transmission properties of Floquet modes. Therefore the useful features of characteristic modes, especially utilized in antenna problems, can also be exploited for the unit cell problem.

Secondly, the characteristic mode analysis makes the use of reactive loads very convenient. Using continuous loading on the scattering element, the mode-of-interest can be made resonant at any frequency [10]. Although changing the resonant frequency in this way can simplify the antenna design, it has been discussed that physical implementation of such loading would be hard since it requires the application of reactive loads over set of basis functions [24]. Especially in the unit cell problem, using predetermined loads to change reflection and transmission characteristics of the unit cell element would have been paved the way for an efficient design methodology. If it were possible to reduce the load distribution on the unit cell element to few loads, the design of loaded unit cell element could have been performed without the need for optimization algorithms that increase the computational cost and complexity.

Thirdly, excitation-independent nature of the characteristic modes makes them very convenient to be utilized as macro basis functions. Although there is already a reflectarray analysis method using CMs as macro basis functions [21], further analyses are also needed to fully exploit excitation-free nature of the CM basis functions. In the macro basis function approach, the goal is to reduce the size of the impedance matrix, however too many CMs may be needed to ensure the solution accuracy in the near field. Especially in very large array structures, using multiple characteristic modes may not yield the desired amount of reduction, hence multilevel matrix reduction can be considered to adequately reduce the degree of freedom. Therefore, in addition to the multilevel version of the conventional CBFM [18, 19], a similar approach of multilevel reduction can also be considered using characteristic modes as macro basis functions.

1.2 Proposed Methods and Models

This dissertation consists of three interrelated topics that address the ideas summarized in Section 1.1. In the first part, an efficient tool has been developed on MATLAB in order to perform MoM-based solution of the periodic unit cell element as well as the analysis of the characteristic modes. After verifying the accuracy of the developed program by comparing with commercial EM simulation tools, the characteristic mode analysis of an FSS element is demonstrated. The reflection response of the element is discussed with respect to the angle of incidence through characteristic modes. The reflectarray element is also analyzed, and the phase responses of the unit cell elements are interpreted in terms of the characteristic modes.

In the second part, a design methodology for the unit cell element has been sought by exploiting the theory of characteristic modes. In this respect, reactive load distribution over the ring-type FSS element is calculated to shift the resonance frequency of the mode of interest to any desired frequency. It has been seen that this method can also be implemented to shift the reflection band of the FSS element as desired. Since it is not practical, if not impossible, to apply a continuous load distribution on the FSS element, an original method has been proposed for ring-type FSS elements that takes the average of the continuous load distribution and reduces it to two discrete lumped elements. Applying the pre-calculated lumped elements on the unit cell element, it has become possible with sufficient accuracy to shift reflection band of the ring-type FSS element to any desired frequency.

The third part of this work differs from the first two parts as this time, the characteristic mode analysis is not performed on the unit cell element but performed on isolated array elements at open boundary conditions. Then the characteristic modes are utilized as macro basis functions for large finite arrays. In addition, additional basis functions induced by modal currents on the neighboring elements are also incorporated into the solution as secondary basis functions, and the outcomes are evaluated. Finally, a multilevel matrix reduction method is proposed in which the characteristic modes are used as basis functions in the first level, which is then followed by the conventional CBFM technique in the second level.

Note that since the MoM program is developed for only conducting surfaces, metal-only elements are considered in all analyses and solutions. However it is still possible to realize such array structures by applying metal layers on styrofoam-like materials that have very low dielectric constant.

1.3 Contributions and Novelties

Our contributions are as follows:

- The application area of the characteristic mode analysis has been extended to the solution of periodic unit cell.
- It has been contributed that characteristic mode analysis can yield insights to understand the phase response of reflectarray elements.
- A novel method is proposed based on the characteristic mode analysis of the unit cell element to calculate lumped element values beforehand that shifts total reflection and transmission band of the ring-type FSS element to the desired frequency with sufficient accuracy. Therefore, load values can be calculated efficiently without the need for optimization-based methods that increase the computational time and cost.
- In addition to the use of characteristic modes as macro basis functions in the finite array solution, the use of secondary basis functions, coming from element interactions, is also demonstrated.
- Similar to the MLCBFM, a multilevel matrix reduction method is recommended that utilizes characteristic modes as macro basis functions at Level-1, and followed by the conventional CBFM at Level-2.

1.4 The Outline of the Thesis

The organization of this dissertation is as follows: Chapter 2 is dedicated to the numerical computation method utilized throughout this work. Hence the Method of

Moment solution of the integral equation using RWG basis functions is given. The computational aspects including the mesh definition and the numerical evaluation of singularities are also explained in detail. Besides, the theory of the characteristic mode is presented and the mode tracking algorithm developed for this work is demonstrated.

In Chapter 3, the periodic unit cell solution is given within the MoM solution. Floquet analysis of 2D periodic elements in spectral domain is discussed, and the computational aspects including Ewald's transformation and handling the continuity on the unit cell boundaries are thoroughly explained. After that, the characteristic mode analysis of the unit cell element is performed on the FSS element of Jerusalem cross. The modes obtained from the CMA are interpreted together with the reflection behavior. Then metal-only reflectarray elements are investigated using the characteristic modes. The relation between the characteristic modes and the phase response for several reflectarray elements are discussed.

In Chapter 4, the reactive loading concept is introduced in the context of the CMA for the ring-type FSS element. After finding the load distribution that shifts the resonance band of the mode-of-interest to the desired frequency, the method of reducing the continuous load distribution into two discrete lumped elements is given. Then the application of the same solution to the complementary slot element is presented based on the duality principle. After that, the proposed method for calculating the required load values to shift the reflection band of the unit cell element to the desired frequency is summarized in a flowchart. The method has been demonstrated on metal ring-type as well as slot ring-type elements of different geometries.

In the beginning of Chapter 5, it has been shown that characteristic modes can be used as basis functions. Then the matrix reduction method using macro basis functions is explained in the context of the conventional CBFM. After that, incorporation of the characteristic modes is demonstrated as macro basis functions. In the second part of this chapter, the multilevel matrix reduction with CM basis functions is given and demonstrated for large arrays consisting of randomly scaled elements.

Chapter 6 provides the conclusion and emphasizes on the possible future work.

CHAPTER 2

NUMERICAL COMPUTATION METHOD

In this chapter, the electric field integral equation (EFIE) is explained for electromagnetic scattering from the surface of perfectly electric conductors (PECs). General aspects of the Method of Moments (MoM) is discussed for the solution of 3D arbitrary scatterers. MoM provides an accurate numerical computation environment for the solution of linear integral equations. Within this method, a conducting surface is discretized into subdomains, and the surface current on each subdomain is modeled by weighted basis functions. Subsequently taking the inner product of the equations with test functions yields a set of linear equations in the form of matrix vector multiplication. As the solution of the matrix equation yields weighting coefficients for the basis functions, the surface current can be calculated.

The basis functions can be defined such that each function exists over only a subdomain. The basis function of this type is known as the subdomain basis function [5]. In the solution of the EFIE, basis functions such as rooftop functions [25] and Rao-Wilton-Glisson (RWG) functions [6] are popular choices for rectangular and triangular discretization, respectively. Since triangular discretization provides flexibility and high accuracy, RWG basis functions are utilized in this work. Basic examples of the triangular mesh discretization are depicted in Fig. 2.1.

Using the Method of Moments, a set of orthogonal modes can be obtained by utilizing the generalized eigenvalue equation [8, 9]. The solution of such equation yields characteristic modes, which are basically a weighted set of orthogonal modes that model the current density on the conducting surface. The computational aspects of the characteristic modes with an efficient mode tracking algorithm are also given in this chapter.

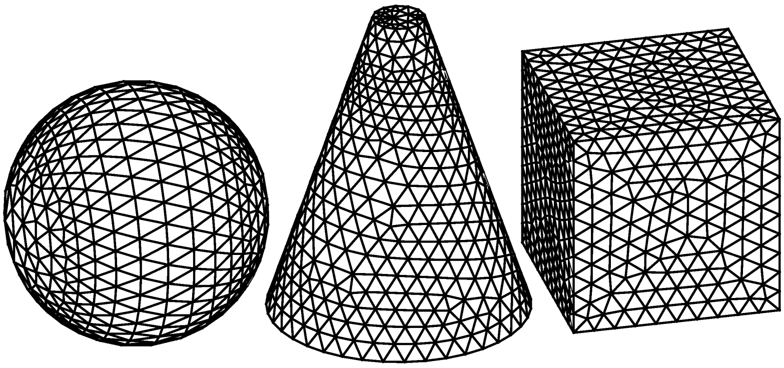

Figure 2.1: Examples for the triangular surface discretization.

In this thesis study, an in-house code is developed on MATLAB, and thus an efficient computational tool is obtained. Using this tool, the MoM solution as well as the characteristic mode analysis are performed. In order to reduce the execution time, the scripts associated with the filling of the MoM matrix are generated in the form of C++ MEX-scripts, with the help of MATLAB Coder [26].

2.1 The Integro-Differential Equation

The electric field integral equation provides the relation between the excitation and the induced current by enforcing boundary conditions for tangential electric field. The solution of the equation with the Method of Moments yields the induced current density on the conducting surface. Then the scattered and total radiating fields can be calculated in the post-processing stage. In this section, expression of the EFIE is given for the general solution of conducting elements. Metallic losses are neglected for simplicity, hence the surfaces are considered as PEC. $e^{j\omega t}$ time dependence is assumed throughout the formulation.

The total tangential electric field, $\mathbf{E}^t$, on a conducting surface is zero, thus

$$\widehat{\mathbf{n}} \times \mathbf{E}^t = \widehat{\mathbf{n}} \times (\mathbf{E}^i + \mathbf{E}^s) = 0 \tag{2.1}$$

where $\widehat{\mathbf{n}}$ is the outward unit vector normal to the conducting surface, $\mathbf{E}^i$ is the incident electric field and $\mathbf{E}^s$ is the scattered electric field. (2.1) can also be expressed as

$$\widehat{\mathbf{n}} \times \mathbf{E^i} = -\widehat{\mathbf{n}} \times \mathbf{E^s}. \tag{2.2}$$

In the scattering problem, as the incident field impinges on a scatterer, an electrical current is induced, thus radiates the scattered field. The scattered electric field can be calculated using the vector potential $\mathbf{A}$ and the scalar potential ϕ as

$$\mathbf{E} = -\nabla\phi - j\omega\mathbf{A}. \tag{2.3}$$

By substituting Lorentz Gauge, i.e., $\phi = -\nabla\cdot\mathbf{A}/(j\omega\mu\epsilon)$, the equation in (2.3) reduces to

$$\mathbf{E}^s = -j\frac{1}{\omega\mu\epsilon}\nabla(\nabla\cdot\mathbf{A}) - j\omega\mathbf{A}. \tag{2.4}$$

If $\mathbf{J}$ represents the current density over the surface, the solution for the vector potential can be defined as

$$\mathbf{A} = \mu\int_S \mathbf{J}(\mathbf{r}')G\left(\mathbf{r},\mathbf{r}'\right)d\mathbf{r}' \tag{2.5}$$

where $G\left(\mathbf{r},\mathbf{r}'\right)$ is the Green's function, $\mathbf{r}'$ refers to the source point over the surface S, and $\mathbf{r}$ is the observation point. Substituting (2.5) into (2.4) and defining the divergence operation on the current source yields

$$\mathbf{E}^{\mathrm{s}} = -j\frac{1}{\omega\epsilon}\nabla\int_S \nabla'\cdot\mathbf{J}(\mathbf{r}')G\left(\mathbf{r},\mathbf{r}'\right)d\mathbf{r}' - j\omega\mu\int_S \mathbf{J}(\mathbf{r}')G\left(\mathbf{r},\mathbf{r}'\right)d\mathbf{r}'. \tag{2.6}$$

where ∇ and ∇' are gradient and divergence operators applied over observation and source coordinates, respectively. As the observation point is chosen on the conducting surface such that $\mathbf{r} = \mathbf{r}_s$, substituting (2.6) into (2.2) yields the electric field integral equation, i.e.,

$$\begin{aligned}\widehat{n}\times\mathbf{E}^i(\mathbf{r}=\mathbf{r}_s) = \widehat{n}\times\Bigg[j\frac{1}{\omega\epsilon}\nabla\int_S \nabla'\cdot\mathbf{J}(\mathbf{r}')G\left(\mathbf{r}_s,\mathbf{r}'\right)d\mathbf{r}' \\ +j\omega\mu\int_S \mathbf{J}(\mathbf{r}')G\left(\mathbf{r}_s,\mathbf{r}'\right)d\mathbf{r}'\Bigg].\end{aligned} \tag{2.7}$$

As can be seen from (2.7), the integro-differential equation provides the direct relation between the incident electric field applied on the conductor, and the induced current on its surface. To calculate the surface current density over the conduction surface in the free space, 3D spatial free-space Green's function can be utilized within the EFIE as

$$G\left(\mathbf{r},\mathbf{r}'\right) = \frac{e^{-jkR}}{4\pi R} \tag{2.8a}$$

$$R = \left|\mathbf{r}-\mathbf{r}'\right| \tag{2.8b}$$

where k is the wavenumber. In the free space, wavenumber holds the dispersion relation $k = \omega\sqrt{\epsilon\mu}$ where permittivity $\epsilon = \epsilon_0 \approx 8.854 \times 10^{-12}$ F/m and the permeability $\mu = \mu_0 \approx 4\pi \times 10^{-7}$ H/m. Note that the intrinsic impedance in the free space becomes $\eta = \eta_0 = \sqrt{\mu_0/\epsilon_0} \approx 120\pi\,\Omega$.

2.2 The Application of the Method of Moments

The integro-differential operator can be expressed such that

$$\mathcal{L}\left\{\mathbf{X}(\mathbf{r}')\right\} = j\frac{1}{\omega\epsilon}\nabla \int_S \nabla' \cdot \mathbf{X}(\mathbf{r}') G\left(\mathbf{r}, \mathbf{r}'\right) d\mathbf{r}' + j\omega\mu \int_S \mathbf{X}(\mathbf{r}') G\left(\mathbf{r}, \mathbf{r}'\right) d\mathbf{r}' \quad (2.9)$$

and thus the electric field integral equation can be simply defined as

$$\widehat{\mathbf{n}} \times \left(\mathcal{L}\left\{\mathbf{J}(\mathbf{r}')\right\} - \mathbf{E}^i(\mathbf{r})\right) = 0. \quad (2.10)$$

In order to solve the equation, the unknown surface current density, $\mathbf{J}(\mathbf{r}')$, is approximated as a weighted sum of N basis functions $\mathbf{f}_n(\mathbf{r}')$ as

$$\mathbf{J}(\mathbf{r}') \approx \sum_{n=1}^{N} \alpha_n \mathbf{f}_n(\mathbf{r}'). \quad (2.11)$$

Thus (2.10) can be expressed in terms of the basis functions as

$$\mathbf{R} = \widehat{\mathbf{n}} \times \left\{ \left[\sum_{n=1}^{N} \alpha_n \mathcal{L}\left\{\mathbf{f}_n(\mathbf{r}')\right\} \right] - \mathbf{E}^i(\mathbf{r}) \right\} \quad (2.12)$$

where $\mathbf{R}$ is the residual function that comes from the approximation of the surface current with basis functions. To minimize the residual, an inner product between the residual function and a test function, $\mathbf{f}_m(\mathbf{r})$ is formed. In such formulation, both basis and test functions can be chosen of the same type, which is known as Galerkin's method [5]. The inner product of (2.12) can be assumed to be zero as shown in (2.13).

$$< \mathbf{f}_m(\mathbf{r}), \widehat{n} \times \left\{ \left[\sum_{n=1}^{N} \alpha_n \mathcal{L}\left\{\mathbf{f}_\mathbf{n}(\mathbf{r}')\right\} \right] - \mathbf{E}^i(\mathbf{r}) \right\} >= 0 \quad (2.13)$$

Note that m and n correspond to the basis and test functions, respectively. Since the test function is defined on the surface, it is tangential by the definition. Therefore, (2.13) can be expressed as

$$< \mathbf{f}_m(\mathbf{r}), \sum_{n=1}^{N} \alpha_n \mathcal{L}\left\{\mathbf{f}_n(\mathbf{r}')\right\} >=< \mathbf{f}_m(\mathbf{r}), \mathbf{E}^i(\mathbf{r}) > . \quad (2.14)$$

Because the summation in (2.14) is not depended on the test function, the equation can also be expressed as

$$\sum_{n=1}^{N} \alpha_n < \mathbf{f}_m(\mathbf{r}), \mathcal{L}\left\{\mathbf{f}_n(\mathbf{r}')\right\} >=< \mathbf{f}_m(\mathbf{r}), \mathbf{E}^i(\mathbf{r}) > . \tag{2.15}$$

Using same number of test functions as the basis functions, a linear set of N equations can be defined to calculate N unknowns, hence the MoM equation is formed as given in (2.16).

$$\mathbf{ZI} = \mathbf{V} \tag{2.16a}$$

$$Z_{mn} =< \mathbf{f}_m(\mathbf{r}), \mathcal{L}\left\{\mathbf{f}_n(\mathbf{r}')\right\} > \tag{2.16b}$$

$$V_m =< \mathbf{f}_m(\mathbf{r}), \mathbf{E}^i(\mathbf{r}) > \tag{2.16c}$$

$$I_n = \alpha_n \tag{2.16d}$$

Once the MoM impedance matrix, $\mathbf{Z}$, and the excitation vector, $\mathbf{V}$, is filled by solving (2.16b) and (2.16c), respectively, the matrix equation in (2.16a) can be constructed.

2.2.1 The Use of RWG Basis Functions

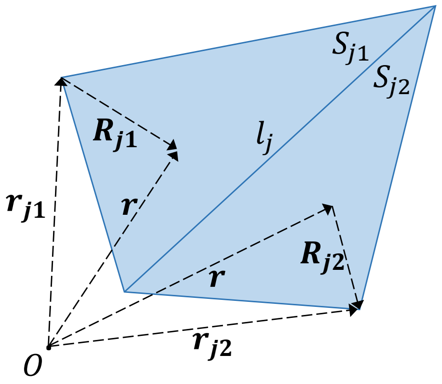

Figure 2.2: Defining parameters of an RWG basis function.

Rao-Wilton-Glisson [6] functions are edge-based vector basis functions. Because RWG vector elements are very flexible and easy to implement, they have become a popular choice in the solution of 3D arbitrary structures. RWG functions are defined on triangular subdomains such that each pair of triangles that share a common edge form an RWG. Defining parameters for jth RWG function is depicted in Fig. 2.2.

The mathematical definition can be given as

$$\mathbf{f}_j(\mathbf{r}) = \begin{cases} \dfrac{l_j \mathbf{R}_{j1}}{2A_{j1}}, & \mathbf{r} \in S_{j1} \\ \dfrac{l_j \mathbf{R}_{j2}}{2A_{j2}}, & \mathbf{r} \in S_{j2} \\ \quad 0 \ , & \text{otherwise} \end{cases} \tag{2.17a}$$

$$\mathbf{R}_{j1} = \mathbf{r} - \mathbf{r}_{j1} \tag{2.17b}$$

$$\mathbf{R}_{j2} = \mathbf{r}_{j2} - \mathbf{r} \tag{2.17c}$$

where A_{j1} and A_{j2} defines the surface area of triangular subdomains S_{j1} and S_{j2}, respectively. l_j is the length of the common edge of both triangles. Direction of the RWG vector function defined on the first triangular surface S_{j1} is from the free vertex of the first triangle, $\mathbf{r}_{j1}$, to any point observed on S_{j1}. On the contrary, the function on the second triangular surface S_{j2} is directed from any point observed on its surface to the free vertex of the second triangle, $\mathbf{r}_{j2}$. Therefore the vector distribution is expressed from one free vertex to another, with magnitude of zero at free vertices while the magnitude is increasing towards the common edge. Within the Method of Moments, such vector distribution is utilized to model surface current density on each RWG vector element. Each triangle is tabulated to be used by minimum one and maximum three different RWG functions. Once coefficients corresponding to each basis RWGs are calculated through matrix-vector multiplication of (2.16a), the surface current on each triangular subdomain can be calculated.

One of the many advantages of RWG basis functions is that they are divergence conforming in nature. It means that the divergence of the RGW function is finite and can be expressed as

$$\nabla \cdot \mathbf{f}_j(\mathbf{r}) = \begin{cases} \dfrac{l_j}{A_{j1}}, & \mathbf{r} \in S_{j1} \\ -\dfrac{l_j}{A_{j2}}, & \mathbf{r} \in S_{j1} \\ \quad 0 \ , & \text{otherwise} \end{cases} \tag{2.18}$$

which turns out to be very useful in the solution of the EFIE. As inner products in the impedance matrix elements and the voltage vector elements are defined on triangular subdomains S_m, (2.16b) and (2.16c) can be expressed as

$$Z_{mn} = \int_{Sm} d\mathbf{r}\, \mathbf{f}_m(\mathbf{r}) \cdot \mathcal{L}\left\{\mathbf{f}_n(\mathbf{r}')\right\} \tag{2.19a}$$

$$V_m = \int_{Sm} d\mathbf{r}\, \mathbf{f}_m(\mathbf{r}) \cdot \mathbf{E}^i(\mathbf{r}) \tag{2.19b}$$

Substituting integro-differential operator in (2.9) into (2.19a) yields

$$\begin{aligned} Z_{mn} = j\frac{1}{\omega\epsilon} \int_{Sm} d\mathbf{r}\, \mathbf{f}_m(\mathbf{r}) \cdot \nabla \int_{Sn} d\mathbf{r}'\, \nabla' \cdot \mathbf{f}_n(\mathbf{r}') G\left(\mathbf{r}, \mathbf{r}'\right) \\ + j\omega\mu \int_{Sm} d\mathbf{r}\, \mathbf{f}_m(\mathbf{r}) \cdot \int_{Sn} d\mathbf{r}' \mathbf{f}_n(\mathbf{r}') G\left(\mathbf{r}, \mathbf{r}'\right). \end{aligned} \tag{2.20}$$

In order to exploit divergence conforming nature of the RWG vector, the product rule of the vector identity can be applied. Since there is no source at the boundaries, the product rule can be expressed as in (2.21).

$$\int_S \mathbf{A} \cdot \nabla \phi ds = \int_S \left\{ \nabla \cdot (\phi \mathbf{A}) - \phi \nabla \cdot \mathbf{A} \right\} ds = - \int_S \phi \nabla \cdot \mathbf{A} ds \tag{2.21}$$

Applying this rule on the first term of (2.20), the entries of the impedance matrix can be expressed as

$$\begin{aligned} Z_{mn} = \frac{1}{j\omega\epsilon} \int_{Sm} d\mathbf{r}\ \left[\nabla \cdot \mathbf{f}_m(\mathbf{r})\right] \int_{Sn} d\mathbf{r}'\, \nabla' \cdot \mathbf{f}_n(\mathbf{r}') G\left(\mathbf{r}, \mathbf{r}'\right) \\ + j\omega\mu \int_{Sm} d\mathbf{r}\, \mathbf{f}_m(\mathbf{r}) \cdot \int_{Sn} d\mathbf{r}' \mathbf{f}_n(\mathbf{r}') G\left(\mathbf{r}, \mathbf{r}'\right). \end{aligned} \tag{2.22}$$

By expanding RWG functions in (2.22), it becomes

$$\begin{aligned} Z_{mn} = \sum_{p=1}^{2} \sum_{q=1}^{2} l_m l_n \zeta_{mp} \zeta_{nq} \left\{ \frac{1}{j\omega\epsilon} \frac{1}{A_{mp}} \int_{Smp} d\mathbf{r}\, \frac{1}{A_{nq}} \int_{Snq} d\mathbf{r}' G\left(\mathbf{r}, \mathbf{r}'\right) \right. \\ \left. + \frac{j\omega\mu}{4} \frac{1}{A_{mp}} \int_{Smp} d\mathbf{r}\, (\mathbf{r} - \mathbf{r}_{mp}) \cdot \frac{1}{A_{nq}} \int_{Snq} d\mathbf{r}' (\mathbf{r}' - \mathbf{r}_{nq}) G\left(\mathbf{r}, \mathbf{r}'\right) \right\} \end{aligned} \tag{2.23}$$

where $\zeta_{j1} = 1$ and $\zeta_{j2} = -1$ as $p = 1$ and $q = 1$ corresponds to the first (positive) triangle of the test and basis functions of jth RWG, respectively. Similarly, $p = 2$ and $q = 2$ corresponds to the second (negative) triangle of the test and basis functions, respectively. The integrals over the observation surface, which is defined with unprimed coordinates, can be easily handled by testing only at the center of the triangle $\mathbf{r}^c_{mp}$, thus

$$\begin{aligned} Z_{mn} = \sum_{p=1}^{2} \sum_{q=1}^{2} l_m l_n \zeta_{mp} \zeta_{nq} \left\{ \frac{1}{j\omega\epsilon} \frac{1}{A_{nq}} \int_{Snq} d\mathbf{r}' G(\mathbf{r}^c_{mp}, \mathbf{r}') \right. \\ \left. + \frac{j\omega\mu}{4} (\mathbf{r}^c_{mp} - \mathbf{r}_{mp}) \cdot \frac{1}{A_{nq}} \int_{Snq} d\mathbf{r}' (\mathbf{r}' - \mathbf{r}_{nq}) G(\mathbf{r}^c_{mp}, \mathbf{r}') \right\}. \end{aligned} \tag{2.24}$$

In order to extract the singularity and to be able to solve it analytically, the vector subtractions in the second term of (2.24) can also be defined in terms of their projections on the surface. If $\widehat{\mathbf{n}}$ is the unit normal vector defined on the triangle surface, the projection of r onto the surface of the triangle can be defined as $\boldsymbol{\rho} = \mathbf{r} - \widehat{\mathbf{n}}\left(\widehat{\mathbf{n}} \cdot \mathbf{r}\right)$. Using vector projections, (2.24) can also be defined as

$$Z_{mn} = \sum_{p=1}^{2}\sum_{q=1}^{2} l_m l_n \zeta_{mp}\zeta_{nq} \left\{ \frac{j\omega\mu}{4}(\boldsymbol{\rho}^c_{mp} - \boldsymbol{\rho}_{mp}) \cdot \frac{1}{A_{nq}} \int_{Snq} d\mathbf{r}'(\boldsymbol{\rho}' - \boldsymbol{\rho}^c_{mp}) G(\mathbf{r}^c_{mp}, \mathbf{r}') \right.$$
$$\left. + \left[\frac{1}{j\omega\epsilon} + \frac{j\omega\mu}{4}(\boldsymbol{\rho}^c_{mp} - \boldsymbol{\rho}_{mp}) \cdot (\boldsymbol{\rho}^c_{mp} - \boldsymbol{\rho}_{nq}) \right] \frac{1}{A_{nq}} \int_{Snq} d\mathbf{r}' G(\mathbf{r}^c_{mp}, \mathbf{r}') \right\}. \tag{2.25}$$

2.2.2 Numerical Evaluation of the Non-singular Integrals

The solution of the integral equations is challenging due to the singular nature of the Green's function. The free-space Green's function, as expressed in (2.8), goes to infinity when the source and the observation points are in the close vicinity of each other, i.e., $R = |\mathbf{r} - \mathbf{r}'| \approx 0$. Therefore a special treatment is needed to deal with the singular behavior of the Green's function. In order to circumvent this pitfall, (2.8) is expressed as the sum of non-singular and singular terms, hence

$$G\left(\mathbf{r}, \mathbf{r}'\right) = G^{\text{ns}}\left(\mathbf{r}, \mathbf{r}'\right) + G^{\text{s}}\left(\mathbf{r}, \mathbf{r}'\right) = \frac{e^{-jkR} - 1}{4\pi R} + \frac{1}{4\pi R}. \tag{2.26}$$

Substituting the non-singular term, $G^{\text{ns}}\left(\mathbf{r}, \mathbf{r}'\right)$, into (2.25), integrals can be computed numerically using Gaussian quadrature method [27]. In order to apply Gaussian quadrature over the triangular area, coordinates of the three vertices of the triangle are converted into simplex coordinates of the natural triangle, as depicted in Fig. 2.3.

A mapping transformation between the node coordinates of the triangle in Cartesian coordinate system, $\mathbf{r}_1$, $\mathbf{r}_2$, and $\mathbf{r}_3$, and the simplex coordinates of the natural coordinate system, s_x, s_y, and s_z, can be formed when simplex coordinates satisfy

$$s_{x,p} + s_{y,p} + s_{z,p} = 1 \tag{2.27}$$

where p is index of the sample point. Using such transformation, the integral over a triangle can be approximated in simplex coordinates as

$$\frac{1}{A}\int_S x(\mathbf{r})d\mathbf{r} \approx \sum_{t=1}^{T} w_t x(\mathbf{r}^s_t) \tag{2.28}$$

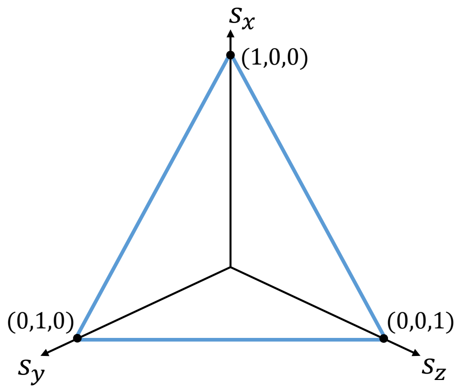

Figure 2.3: Natural triangle in simplex coordinates.

Table 2.1: Simplex coordinates and weights for 3-point Gaussian quadrature.

t	w_t	$s_{x,t}$	$s_{y,t}$	$s_{z,t}$
1	1/3	2/3	1/6	1/6
2	1/3	1/6	2/3	1/6
3	1/3	1/6	1/6	2/3

where

$$\mathbf{r}_t^s = s_{x,t}\mathbf{r}_1 + s_{y,t}\mathbf{r}_2 + s_{z,t}\mathbf{r}_3 \tag{2.29}$$

is the location of the tth sample point in simplex coordinates. T is the number of sample points used in Gaussian quadrature, and w_t is the weight that corresponds to each quadrature point. For 3-point Gaussian quadrature, i.e., $T = 3$, natural simplex coordinates and corresponding weights for sample points are given in Table 2.1. The first term in (2.26) that refers to the non-singular part of the Green's function,

$$\mathrm{G}^{\mathrm{ns}} = \frac{e^{-jkR} - 1}{4\pi R} \tag{2.30}$$

can be handled with the numerical integration. When the source and observation points are very close to each other, it can be simplified using L'Hôpital's rule as given in (2.31).

$$\lim_{R\to 0} \mathrm{G}^{\mathrm{ns}} = \lim_{R\to 0} \frac{e^{-jkR} - 1}{4\pi R} = \frac{-jk}{4\pi} \tag{2.31}$$

Therefore the integral equations in (2.25) for the non-singular part of the free space Green's function can be evaluated as shown in (2.32) and (2.33),

$$\frac{1}{A_{nq}}\int_{Snq} d\mathbf{r}' G^{\mathrm{ns}}(\mathbf{r}^c_{mp},\mathbf{r}') = \begin{cases} \displaystyle\sum_{t=1}^{T} w_t \frac{e^{-jk|\mathbf{r}^c_{mp}-\mathbf{r}'^s_t|}-1}{4\pi|\mathbf{r}^c_{mp}-\mathbf{r}'^s_t|}, & R \gg 0 \\ \displaystyle\sum_{t=1}^{T} w_t \frac{-jk}{4\pi}, & R \approx 0 \end{cases} \tag{2.32}$$

$$\begin{aligned} &\frac{1}{A_{nq}}\int_{Snq} d\mathbf{r}'(\mathbf{r}'-\mathbf{r}^c_{mp}) G^{\mathrm{ns}}(\mathbf{r}^c_{mp},\mathbf{r}') \\ &\quad = \begin{cases} \displaystyle\sum_{t=1}^{T} w_t \frac{e^{-jk|\mathbf{r}^c_{mp}-\mathbf{r}'^s_t|}-1}{4\pi|\mathbf{r}^c_{mp}-\mathbf{r}'^{\mathbf{s}}_{\mathbf{t}}|}(\mathbf{r}'^s_t-\mathbf{r}^c_{mp}), & R \gg 0 \\ \displaystyle\sum_{t=1}^{T} w_t \frac{-jk}{4\pi}(\mathbf{r}'^s_t-\mathbf{r}^c_{mp}), & R \approx 0 \end{cases} \end{aligned} \tag{2.33}$$

where

$$\mathbf{r}'^s_t = s_{x,t}\mathbf{r}'_1 - s_{y,t}\mathbf{r}'_2 - s_{z,t}\mathbf{r}'_3. \tag{2.34}$$

2.2.3 Analytical Evaluation of the Singular Part of the Green's Function

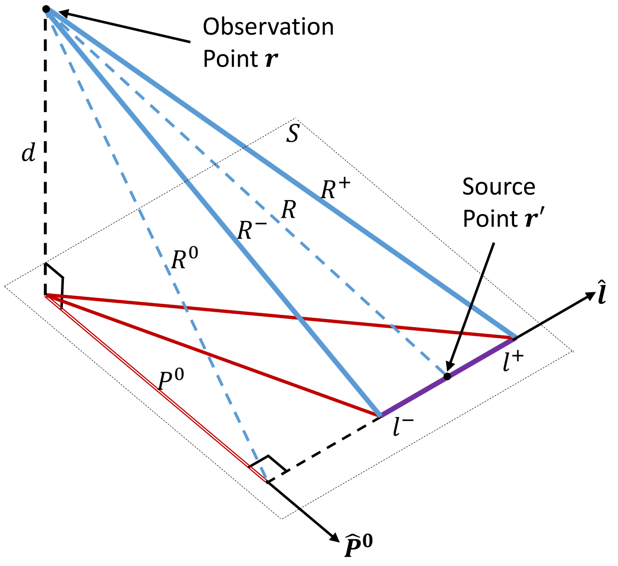

Figure 2.4: Illustration of geometric quantities in the analytical solution of singular integrals.

The computation of the singular part of Green's function can be performed using the method given in [28]. In this method, the observation point is projected onto S, as shown in Fig. 2.4. The observation point, $\mathbf{r}$, and the source point, $\mathbf{r}'$, that are projected on S can be defined as ρ and ρ', respectively. Therefore if vertices of a triangle edge are defined in S as $\mathbf{r}^-$ and $\mathbf{r}^+$, the projection of these points can be defined as ρ^- and ρ^+, and thus,

$$\boldsymbol{\rho}^{\pm} = \mathbf{r}^{\pm} - \widehat{\mathbf{n}}\left(\widehat{\mathbf{n}} \cdot \mathbf{r}^{\pm}\right). \tag{2.35}$$

As following the notation in [29] and based on Fig. 2.4, the necessary parameters can be calculated as given in (2.36).

$$\boldsymbol{\rho}^{\pm} = \mathbf{r}^{\pm} - \widehat{\mathbf{n}}\left(\widehat{\mathbf{n}} \cdot \mathbf{r}^{\pm}\right) \tag{2.36a}$$

$$\widehat{\mathbf{l}} = \frac{\rho^+ - \rho^-}{|\rho^+ - \rho^-|} \tag{2.36b}$$

$$\widehat{\mathbf{u}} = \widehat{\mathbf{l}} \times \widehat{\mathbf{n}} \tag{2.36c}$$

$$l^{\pm} = \left(\boldsymbol{\rho}^{\pm} - \boldsymbol{\rho}\right) \cdot \widehat{\mathbf{l}} \tag{2.36d}$$

$$P^0 = \left|\left(\boldsymbol{\rho}^{\pm} - \boldsymbol{\rho}\right) \cdot \widehat{\mathbf{u}}\right| \tag{2.36e}$$

$$P^{\pm} = \left|\left(\boldsymbol{\rho}^{\pm} - \boldsymbol{\rho}\right)\right| = \left[(P^0)^2 + (l^{\pm})^2\right]^{1/2} \tag{2.36f}$$

$$\widehat{\mathbf{P}}^0 = \frac{\left(\boldsymbol{\rho}^{\pm} - \boldsymbol{\rho}\right) - l^{\pm}\widehat{\mathbf{l}}}{P^0} \tag{2.36g}$$

$$d = \widehat{\mathbf{n}} \cdot \left(\mathbf{r} - \mathbf{r}^{\pm}\right) \tag{2.36h}$$

$$R^0 = \left[(P^0)^2 + d^2\right]^{1/2} \tag{2.36i}$$

$$R^{\pm} = \left[(P^{\pm})^2 + d^2\right]^{1/2} \tag{2.36j}$$

In order to evaluate the integral in (2.25) for the singular part of the Green's function, $\rho = \rho_p^c$ can be used in (2.36) since the testing is performed at the center of the triangle. Therefore the singular integrals of the integral equation can be evaluated as shown in (2.37) and (2.38).

$$\int_{Snq} \frac{\boldsymbol{\rho}' - \boldsymbol{\rho}_p^c}{R} d\mathbf{r}' = \frac{1}{2}\sum_{i=1}^{3} \widehat{\mathbf{u}}_{\mathbf{i}} \left[\left(R_i^0\right)^2 \log\frac{R_i^+ + l_i^+}{R_i^- + l_i^-} + l_i^+ R_i^+ - l_i^- R_i^-\right] \tag{2.37}$$

$$\begin{aligned} \int_{Snq} \frac{1}{R} d\mathbf{r}' = \sum_{i=1}^{3} \widehat{\mathbf{P}}_i^0 \cdot \widehat{\mathbf{u}}_i \Bigg[P_i^0 \log\frac{R_i^+ + l_i^+}{R_i^- + l_i^-} - \\ |d| \tan^{-1}\left(\frac{P_i^0 l_i^+}{\left(R_i^0\right)^2 + |d|\, R_i^+} - \frac{P_i^0 l_i^-}{\left(R_i^0\right)^2 + |d|\, R_i^-}\right)\Bigg] \end{aligned} \tag{2.38}$$

2.2.4 Triangular Discretization Aspects

Domain discretization is an important aspect of numerical computations regarding the solution accuracy and computational cost. Using larger triangular subdomains would reduce the number of subsectional basis functions, hence smaller matrices and fast solutions can be achieved. However the size of the triangles must be electrically small in order to achieve accurate results. Although there is no exact rule for determining the correct dimension for discretization, it is common to choose the triangle size between $\lambda/10$ and $\lambda/20$ in order to guarantee the accuracy of the solution. The geometry of the surface and the excitation also affect the mesh size and the mesh density. Meshes smaller than $\lambda/20$ can also be defined if there are fine details on the solution surface. Especially in radiation problems in which the feeding must be defined on the element surface, discretization must be done carefully around the feed location to achieve good accuracy.

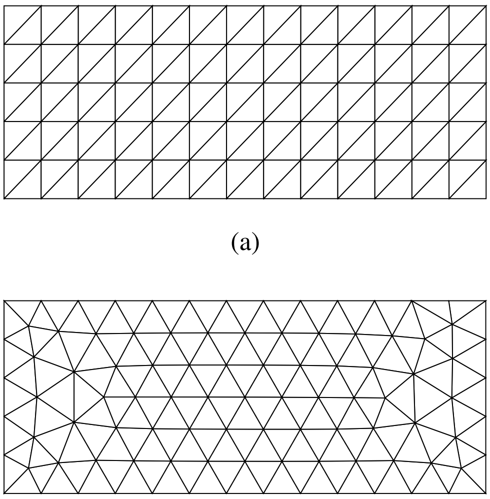

(a)

(b)

Figure 2.5: Mesh types. (a) Structured mesh. (b) Unstructured mesh.

In this work, *Siemens NX 10*, a computer aided engineering software, is utilized in order to construct triangular subdomains. The discretization can be performed with either structured or unstructured meshes. To create a structured mesh, the software divides the surface of interest repeatedly into smaller surfaces to create subdomains. Unlike this type of subdivision, an unstructured mesh can also be formed by the paving technique as given in [30]. As an illustration, a rectangular plate is discretized by both structured and unstructured mesh as depicted in Fig. 2.5. Using the software, the node coordinates of each triangle are obtained in the first step, and then RWG functions that correspond to each pair of triangles are formed. Finally RWG functions are arranged according to their index numbers. Hence each RWG vector function is defined in terms of its index, as well as the surface area, vector direction and the edge length common for the corresponding pair of triangles. For instance in Fig. 2.6, 51 RWG elements are constructed using 40 triangles over an unstructured triangular mesh.

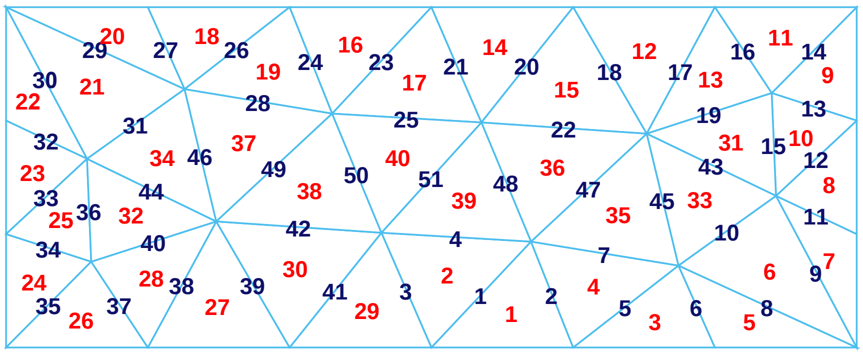

Figure 2.6: Definition of triangles (red) and RWGs (blue)

2.3 The Characteristic Mode Analysis

The impedance matrix obtained by the MoM solution can be utilized directly in the analysis of characteristic modes. As described in [8, 9], the impedance matrix can be presented as

$$\mathbf{Z} = \mathbf{R} + j\mathbf{X} \tag{2.39}$$

where $\mathbf{R}$ and $\mathbf{X}$ are the real and imaginary parts of the impedance matrix, respectively. Both $\mathbf{R}$ and $\mathbf{X}$ are real Hermitian matrices. Theoretically $\mathbf{R}$ is also a positive semi-definite matrix. The generalized eigenvalue equation for the characteristic mode decomposition is defined as

$$\mathbf{X}\mathbf{J_n} = \lambda_n \mathbf{R}\mathbf{J_n} \tag{2.40}$$

where λ_n are the eigenvalues and $\mathbf{J_n}$ are the eigenvectors. Eigenvalues are real, where the corresponding eigenvectors are also real and orthogonal to each other. MATLAB routine *eig* is employed in the solution of the eigenvalue equation. The solution is normalized as

$$< \mathbf{J_n^*}, \mathbf{RJ_n} >= 1 \tag{2.41}$$

which is the criterion for the unit radiation power. Therefore orthogonality properties of the characteristic modes are defined as

$$< \mathbf{J_m^*}, \mathbf{RJ_n} > = \delta_{mn} \tag{2.42a}$$

$$< \mathbf{J_m^*}, \mathbf{XJ_n} > = \lambda_n \delta_{mn} \tag{2.42b}$$

$$< \mathbf{J_m^*}, \mathbf{ZJ_n} > = (1 + j\lambda_n)\delta_{mn} \tag{2.42c}$$

where δ_{mn} is Kronecker delta function given by

$$\delta_{mn} = \begin{cases} 1, & m = n \\ 0, & m \neq n. \end{cases} \tag{2.43}$$

Since eigenvectors are real, conjugate operators in (2.41) and (2.42) can be neglected. The governing equation in (2.40) is not depended on the excitation, so are the characteristic modes. Thus characteristic modes solely depend on the shape of the scatterer and its physical dimensions in terms of the wavelength.

Since eigenvectors are interpreted as entire domain basis vectors of the current density over the conducting surface, they can be called as eigencurrents. Each eigencurrent radiates power orthogonal to one another. Therefore the induced surface current on the conducting surface can be expressed as weighted sum of eigencurents as

$$\mathbf{J} = \sum_n a_n \mathbf{J_n}. \tag{2.44}$$

Note that since the induced current on the conducting surface radiates and produces the fields, the total far field can also be expressed as weighted sum of modal fields as shown in (2.45).

$$\mathbf{E} = \sum_n a_n \mathbf{E_n} \tag{2.45a}$$

$$\mathbf{H} = \sum_n a_n \mathbf{H_n} \tag{2.45b}$$

By substituting (2.44) into electric field integral equation in (2.10) yields

$$\widehat{\mathbf{n}} \times \left(\mathcal{L}\left\{ \sum_{n} a_n \mathbf{J_n} \right\} - \mathbf{E}^i(\mathbf{r}) \right) = 0. \tag{2.46}$$

The numerical solution of (2.46) can be formulated by utilizing eigencurrents as entire domain basis functions in the context of the Method of Moments. Therefore the inner product equation in (2.15) can be defined as

$$\sum_{n=1}^{N} a_n < \mathbf{J_m}, \mathbf{Z}\mathbf{J_n} >=< \mathbf{J_m}, \mathbf{E^i} > \tag{2.47}$$

where $m = 1, 2, ..., M$. The substitution of (2.42c) into (2.47) leads

$$\sum_{n=1}^{N} a_n (1 + j\lambda_n)\delta_{mn} =< \mathbf{J_m}, \mathbf{E^i} > . \tag{2.48}$$

Because only the term $m = n$ exists on the left hand side of (2.48) due to the Kronecker delta function, (2.48) becomes

$$a_n(1 + j\lambda_n) =< \mathbf{J_n}, \mathbf{E^i} > \tag{2.49}$$

where $n = 1, 2, ..., N$. The right hand side of (2.49) is known as the modal excitation coefficient, V_n, hence can be presented as

$$V_n =< \mathbf{J_n}, \mathbf{E}^i(\mathbf{r}) >= \int_n \mathbf{J_n} \cdot \mathbf{E^i} ds. \tag{2.50}$$

The modal excitation coefficient indicates the interaction between the mode and the excitation that applied over the conducting body. The scatterer can be illuminated by a plane wave, in which case the incidence angle, polarization, magnitude and phase of the incident wave influence the modal excitation coefficients. In radiation problems, the type of the feed and its location on the surface also affect the value of the excitation coefficient. In fact the induced surface current also depends on the eigenvalues of the generalized eigenvalue equation. As shown in (2.44), modal weighting coefficients, a_n, are defined such that the weighted sum of the eigencurrents yields the induced current on the conducting surface. From (2.49), the modal weighting coefficients, a_n, are expressed as

$$a_n = \frac{V_n}{(1 + j\lambda_n)}. \tag{2.51}$$

The absolute value of the term that relates modal excitation coefficient to modal weighting coefficient is known as the modal significance (MS),

$$\mathrm{MS}_n = \frac{1}{|1 + j\lambda_n|}. \tag{2.52}$$

Modal significance is independent of the excitation, hence expresses the intrinsic nature of the characteristic modes. Since the values of the eigenvalue range from $-\infty$ to ∞, modal significance values provide a better representation of the eigenvalues as they range from 0 to 1. There is also another way of representing eigenvalues in terms of characteristic angles, ϑ_n,

$$\vartheta_n = 180^\circ - \tan^{-1}(\lambda_n) \tag{2.53}$$

which determines the phase difference between the eigencurrent $\mathbf{J_n}$ and the tangential component of modal field $\mathbf{E_n}$ on the conducting surface.

The physical interpretation of the characteristic modes can be done by sorting eigenvalues. In the theory of the characteristic mode, the stored electromagnetic energy of each mode is related to the magnitude of the eigenvalues. This phenomena can be understood by expressing modal fields within Poynting's theorem [31]. Since the total power must be conserved, the supplied complex power in radiation and scattering problems becomes equal to the sum of the total power that exits from the system, the complex stored power and dissipated real power. By neglecting ohmic power loss by assuming the surface PEC, and omitting magnetic current sources in the general formulation because the formulation is defined on the conducting surface, the Poynting's equation for the impressed current density, $\mathbf{J}$, can be expressed as

$$-\int_V \mathbf{E} \cdot \mathbf{J}^* dV = \oint_S (\mathbf{E} \times \mathbf{H}^*)\, dS + j\omega \int_V \left(\mu\, |\mathbf{H}|^2 - \epsilon\, |\mathbf{E}|^2\right) dV \tag{2.54}$$

where the term on the left hand side represents the supplied power, the first term on the right hand side is the total exiting power and the second terms corresponds to the stored magnetic energy and electric energy. The expression of the supplied power as the function of the induced current can also be expressed in terms of $\mathbf{Z}$ matrix notation, thus

$$< \mathbf{Z} \cdot \mathbf{J}, \mathbf{J}^* >= \oint_S (\mathbf{E} \times \mathbf{H}^*)\, dS + j\omega \int_V \left(\mu\, |\mathbf{H}|^2 - \epsilon\, |\mathbf{E}|^2\right) dV. \tag{2.55}$$

Since (2.55) can be expressed in terms of characteristic modes, incorporating modal fields and eigencurrents into the solution and exploiting (2.42c) yields

$$(1 + j\lambda_n)\delta_{mn} = \oint_S (\mathbf{E_m} \times \mathbf{H_n^*})\, dS + j\omega \int_V (\mu\mathbf{H_m} \cdot \mathbf{H_n^*} - \epsilon\mathbf{E_m} \cdot \mathbf{E_n^*})\, dV. \quad (2.56)$$

One can interchange the indices m and n of the equation in (2.56) and then take the complex conjugate of both sides. Subtracting the resulting equation from (2.56) would yield

$$\omega \int_V (\mu\mathbf{H_m} \cdot \mathbf{H_n^*} - \epsilon\mathbf{E_m} \cdot \mathbf{E_n^*})\, dV = \lambda_n\delta_{mn} \quad (2.57)$$

which shows the relation between eigenvalues and the energy stored by the characteristic modes. If $\lambda_n = 0$, the stored electric and magnetic field energy cancels each other which means that the corresponding mode is at resonance. Thus as the eigenvalue is smaller, the mode radiates more efficiently. $\lambda_n > 0$ means that the magnetic energy is being stored more than the electric energy. Such modes can be called as inductive modes. Similarly, modes of $\lambda_n < 0$ are capacitive modes since the electric energy is being stored more than the magnetic energy. This phenomenon can also be interpreted using the values of the characteristic angle. As can be extrapolated from (2.53), the characteristic mode is at resonance when $\vartheta_n = 180°$, an inductive mode when $90° < \vartheta_n < 180°$, and a capacitive mode when $180° < \vartheta_n < 270°$. Moreover modal significance also indicates if a characteristic mode is at resonance. The associated mode is resonant when $\text{MS}_n = 1$. After the eigenvalue equation is solved at any frequency, the modes are sorted by their closeness to the resonance. Thus the mode having the modal significance value closest to 1 is regarded as the most significant mode, or the first mode. Therefore modes are indexed as the first mode, second mode, third mode, etc., according to their MS value being close to 1. Since $\text{MS}_n \in [0, 1]$, a 3-dB bandwidth for characteristic modes can also be defined. The modal bandwidth can be expressed for the range of the frequency to satisfy $\text{MS}_n > 0.707$.

2.3.1 The Mode Tracking

MoM solution and subsequent characteristic mode analysis should be repeated for many frequency samples to observe the wideband properties of the characteristic modes. However when characteristic modes are calculated over a frequency band, the mode indices may not follow the same physical mode as the frequency increases. The reason is that as the frequency changes, the eigenvalue of the modes will also change, hence approaching or moving away from the resonance. If the frequency-of-interest is closest to the resonant frequency of the first mode, such mode can be regarded as the first mode. However such mode may not be the first mode at a different frequency where the resonance frequency of another mode is closest to that frequency. Therefore, to avoid the confusion of interpreting characteristic modes over a frequency band, modes must be tracked according to a reference frequency.

In this study, a simple mode tracking algorithm is implemented to ensure that characteristic modes follow the same current and radiation pattern at different frequencies. It is basically performed by exploiting the orthogonality properties of the characteristic modes and correlating eigenvectors at adjacent frequencies. This algorithm consists of three stages [32]. In the first stage, all eigenvectors are normalized to meet the orthogonality criteria. Then the correlation coefficient matrix is calculated between two adjacent frequency samples. In the last step, the eigenvectors are being matched by gradually reducing the correlation matrix. Further details can be found in [32].

In order to demonstrate the mode tracking algorithm, the rectangular PEC plate of 10 cm $\times$ 4 cm is solved from 0.5 to 5 GHz. At first, modal significance values for the first 6 modes are calculated across the frequency band without implementing the mode tracking algorithm. As can be seen from Fig. 2.7a, there are abrupt changes on the curves which indicate that depicted modes do not follow the same physical pattern throughout the band. Modal significance values after applying the mode tracking algorithm is given in Fig. 2.7b. As can be seen from the figure, utilization of the algorithm makes the curves vary smoothly.

The accuracy of the MATLAB code has been validated by comparisons with commercial EM simulation tool *FEKO* [33] throughout the study. In Fig. 2.8, the magnitude of the eigenvalues for the previous example is compared with FEKO's results. As can be seen from the figure, the results obtained from the MoM code follows FEKO's results very closely. Moreover in 2018, a cross-validation study is performed with research groups from different institutions. As initiated by *The Special Interest Group on Theory of Characteristic Modes, (SIG TCM)* [34], a benchmarking work is conducted for the CM solution of three different geometries [35]. The first problem is a rectangular PEC plate of 10 cm × 4 cm, as already discussed above. The second and third geometries are a PEC circular disc with 10 cm radius and a PEC sphere with 20 cm radius, respectively. In [35], the solutions produced from this study are labeled as "METU" on the legend charts of the graphics. Figures of [35] indicate that the solutions produced by the in-house code are in accordance with the solutions of other participants.

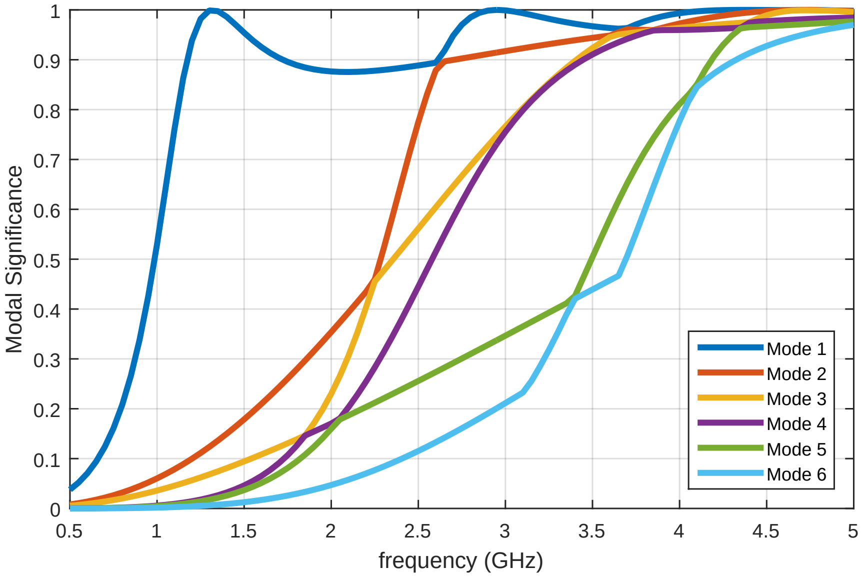

(a)

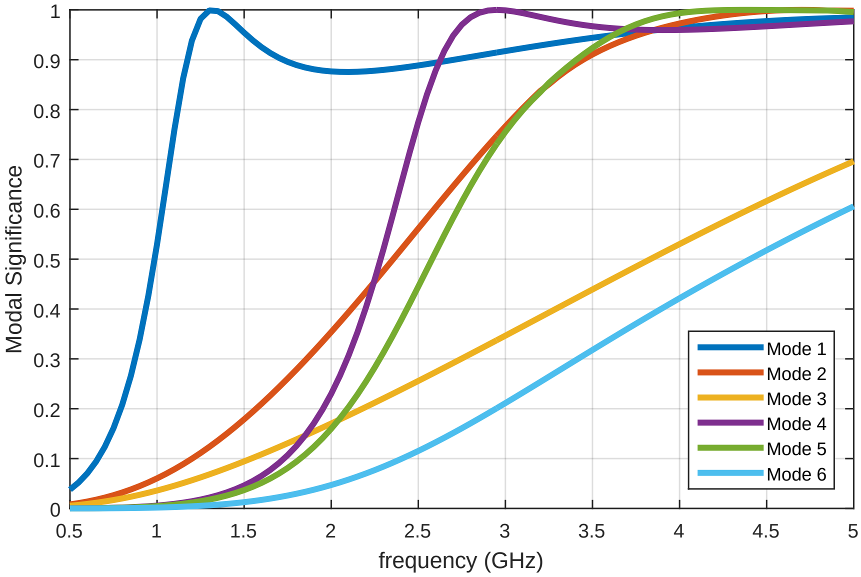

(b)

Figure 2.7: Characteristic modes of the rectangular PEC plate of 10 cm × 4 cm. (a) MS of the first 6 modes without mode tracking. (b) MS of the first 6 modes with mode tracking.

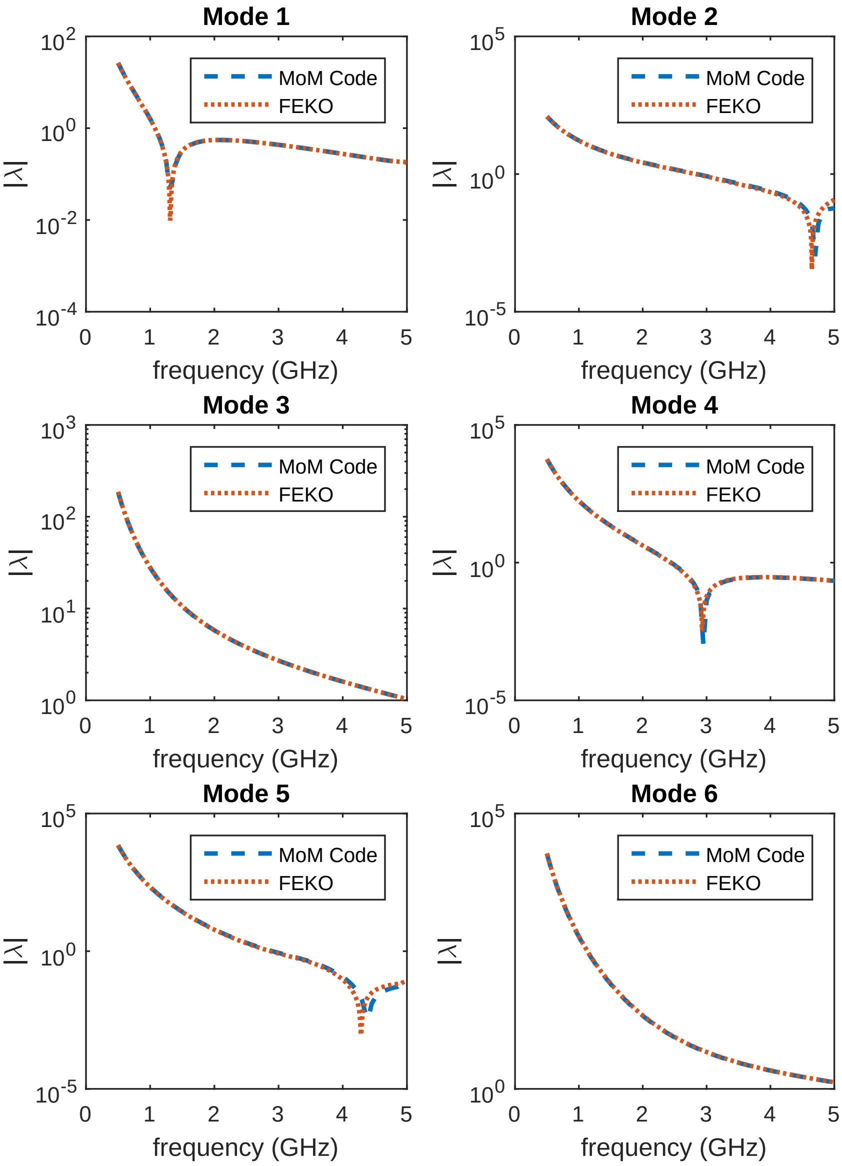

Figure 2.8: Absolute values of the eigenvalues for 10 cm × 4 cm rectangular PEC plate, compared with FEKO's results.

CHAPTER 3

UNIT CELL SOLUTION

The solution of large array structures requires special attention. Since array elements are either identical or very similar to each other and lined up with a repeating pattern, fast and effective solution methods can be exploited. Although the far field in the array antennas can be estimated with some accuracy by simply multiplying the array factor with the element factor, it is often necessary to take into account mutual interactions between array elements.

In this work, method of moment solution of the infinitely large periodic structures is implemented using the periodic Green's function (PGF). The Method of Moments provides simple and effective solution for arbitrary elements in a 2D periodic unit cell. Since purely spatial periodic Green's function, as well as purely spectral periodic Green's function converges very slowly, Ewald's transformation [7] is implemented. In recent years, characteristic mode decomposition of the reflectarray element phase is mentioned [36]. However apart from this introductory conference paper, characteristic mode analysis has not been considered for the unit cell problem. Nevertheless this thesis work yields a comprehensive analysis of the unit cell solution using characteristic modes.

In this chapter, the solution of the periodic Green's function for the metal-only element is demonstrated. The modal analysis of the unit cell element is performed for metal-only FSS and reflectarray elements. It is discussed that advantages of the characteristic mode theory can be exploited in the design and analysis of the large periodic structures.

3.1 Periodic Green's Function

3.1.1 Spatial Form of the Periodic Green's Function

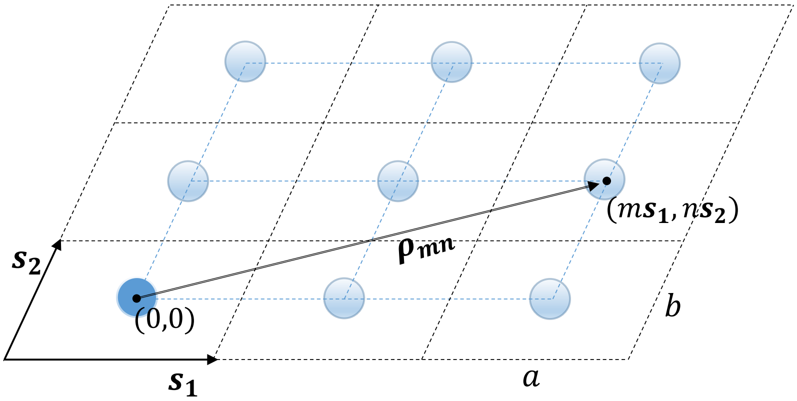

Figure 3.1: Unit lattice cell.

The spatial form of the periodic Green's function (PGF) can be expressed as

$$G_p(\mathbf{r}, \mathbf{r}') = \frac{1}{4\pi} \sum_{m=-\infty}^{\infty} \sum_{n=-\infty}^{\infty} e^{-j\mathbf{k}_{t00}\cdot\rho_{mn}} \frac{e^{-jkR_{mn}}}{R_{mn}} \tag{3.1}$$

where $\mathbf{k}_{t00}$ is the transverse component of the incident wave vector that corresponds to the incident wave of (θ_i, ϕ_i) as

$$\mathbf{k}_{t00} = \hat{\mathbf{x}} k_0 sin\theta_i \cos\phi_i + \hat{\mathbf{y}} k_0 \sin\theta_i \sin\phi_i. \tag{3.2}$$

The translation vector, ρ_{mn}, can be expressed as

$$\boldsymbol{\rho}_{mn} = m\mathrm{s}_1 + n\mathrm{s}_2 \tag{3.3}$$

where s_1 and s_2 are vectors defining the unit lattice cell, as illustrated in Fig.3.1. Hence the distance between source and observation points become

$$R_{mn} = |\mathbf{R} - \boldsymbol{\rho}_{mn}| = |\mathbf{r} - \mathbf{r}' - \boldsymbol{\rho}_{mn}|. \tag{3.4}$$

As long as the rectangular unit lattice cell is concerned, it can be aligned with the $x - y$ coordinate system, thus

$$\mathrm{s}_1 = a\hat{\mathbf{x}} \tag{3.5a}$$

$$\mathrm{s}_2 = b\hat{\mathbf{y}} \tag{3.5b}$$

where a and b are unit cell dimensions in x and y directions, respectively.

3.1.2 Floquet Analysis in Spectral Domain

The periodic Green's function in spatial domain can also be defined in the spectral domain. In this case, the surface current in the unit cell can be represented as the sum of Floquet modes [37, 38]. Floquet modes can be regarded as plane waves that depend on the direction of the propagation, the frequency and the shape of the unit cell element. The transverse wave vector for the Floquet mode of (m, n) can be expressed as

$$\mathbf{k}_{tmn} = k_{xm}\hat{\mathbf{x}} + k_{yn}\hat{\mathbf{y}} \tag{3.6}$$

where

$$k_{xm} = k \sin\theta_i \cos\phi_i + 2\pi m/a \tag{3.7a}$$

$$k_{yn} = k \sin\theta_i \sin\phi_i + 2\pi n/b \tag{3.7b}$$

The z component of the wave number for the corresponding mode becomes

$$k_{zmn} = \sqrt{k^2 - {k_{tmn}}^2} \tag{3.8}$$

where $k_{tmn}^2 = |\mathbf{k}_{tmn} \cdot \mathbf{k}_{tmn}|$. Note that k_{zmn} is real when the wavenumber $k > k_{tmn}$. This is the case when the Floquet mode of (m, n) is a propagating mode. Otherwise, the mode is an evanescent mode that does not propagate but decays in the z direction. By taking squares of the terms in (3.7) and adding them together, an inequality can be obtained for the propagating mode as [39]

$$\left(k_{xm} - \frac{2m\pi}{a}\right)^2 + \left(k_{yn} - \frac{2n\pi}{b}\right)^2 = k^2 \sin^2\theta_i \leq k^2. \tag{3.9}$$

This inequality defines infinitely many circular regions over rectangular unit cell grids as depicted in Fig. 3.2. Each circle, that has a center at $(2m\pi/a, 2n\pi/a)$ and radius k, represents a Floquet mode of (m, n). The Floquet modes can be defined as vector modal functions of either TE_{mn}^z or TM_{mn}^z. The dominant Floquet mode is illustrated in Fig.3.2 by the shaded area where $m = n = 0$. The shaded area is called as the visible scan region [39]. A Floquet mode propagates along the z direction when the corresponding points reside inside the visible scan region. As can be seen from Fig. 3.2, mode circles would not intersect if $\pi/a > k$ and $\pi/b > k$ regardless of the angle

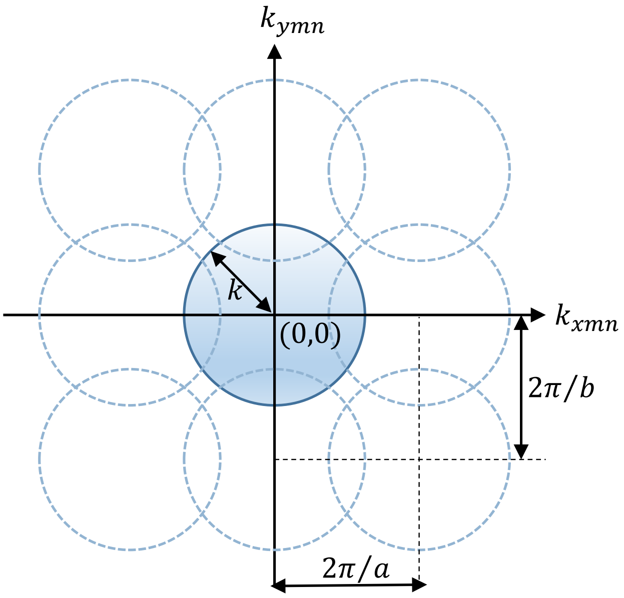

Figure 3.2: Floquet modes in the spectral domain.

of the incidence. Otherwise, grating beams are observed in the visible scan region. Hence it can be inferred that higher order modes do not cause grating beams when $a, b < \lambda/2$. For the special case of the normal incidence, i.e. $\theta_i = 0$, $a, b < \lambda$ must hold, however grating beams would still occur at oblique incidences. For an oblique incidence, it must satisfy

$$k \sin \theta_i < \frac{2\pi}{a} - k \tag{3.10a}$$

$$k \sin \theta_i < \frac{2\pi}{b} - k \tag{3.10b}$$

so that higher order circles do not intersect the circular area inside the shaded region with the radius of $|k \sin \theta_i|$. Hence a general condition for grating beams not occurring in the visible scan region can be expressed by modifying (3.10) as

$$a, b < \frac{\lambda}{(1 + \sin \theta_i)}. \tag{3.11}$$

Using (3.7) and (3.8), the periodic Green's function can be expressed in terms of Floquet modal functions in the spectral domain as [40]

$$G_p(\mathbf{r}, \mathbf{r}') = \sum_{m=-\infty}^{\infty} \sum_{n=-\infty}^{\infty} \frac{e^{-j\mathbf{k}_{tmn} \cdot (\boldsymbol{\rho} - \boldsymbol{\rho}') - jk_{zmn}|z - z'|}}{j2abk_{zmn}}. \tag{3.12}$$

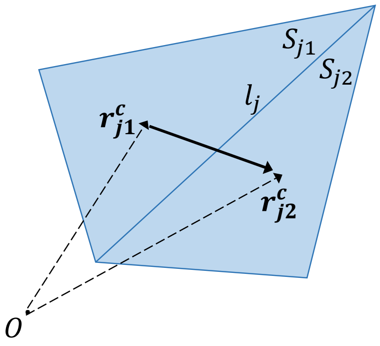

Figure 3.3: Dipole moment vector on an RWG element.

Spectral form of the periodic Green's function can be used in order to calculate the reflected field. Neglecting higher order components of (2.4) in the far field region, the reflected electric field can be expressed as

$$\mathbf{E}^r = -j\omega\mathbf{A}. \tag{3.13}$$

After the current density is calculated by the Method of Moments, the distribution of the surface current over basis functions can be approximated by infinitesimal dipole elements. This approach is known as the dipole modeling [41]. The value of the dipole moment of jth RWG becomes

$$\mathbf{m}_j = \alpha_j l_j (\mathbf{r}^c_{2j} - \mathbf{r}^c_{1j}) \tag{3.14}$$

where α_j is the unknown coefficient of the jth basis function. As illustrated in Fig. 3.3, $\mathbf{r}^c_{1j}$ and $\mathbf{r}^c_{2j}$ are center coordinates of the first (positive) and second (negative) triangles of the jth RWG, respectively. In this way, the dipole vector distribution can be calculated on the unit cell element. Using the sum of dipole moments over the unit cell element, the magnetic vector potential can be written as

$$\mathbf{A} = \mu \sum_{j=1}^{N} \mathbf{m}_j G_p\left(\mathbf{r}, \mathbf{r}'\right). \tag{3.15}$$

Substituting (3.12) into (3.15), the reflected electric field in (3.13) becomes

$$\mathbf{E}^r = -j\omega\mu \sum_{j=1}^{N} \mathbf{m}_j \sum_{m=-\infty}^{\infty} \sum_{n=-\infty}^{\infty} \frac{e^{-j\mathbf{k}_{tmn}\cdot(\boldsymbol{\rho}-\boldsymbol{\rho}'_j)-jk_{zmn}|z-z'_j|}}{j2abk_{zmn}} \tag{3.16}$$

where (x'_j, y'_j, z'_j) can be chosen as the midpoint coordinates of the common edge of the jth RWG function. Moreover if the center of the unit cell is at the origin of the coordinate system, the reflection coefficient of the Floquet mode of (m, n) [38] can be expressed as

$$\mathbf{\Gamma}(m,n) = -j\omega\mu \sum_{j=1}^{N} \mathbf{m}_j \frac{e^{jk_{xm}x'+jk_{yn}y'+jk_{zmn}|z'|}}{j2abk_{zmn}}. \tag{3.17}$$

3.1.3 Ewald's Transformation

Although periodic Green's function is an infinite series, finite number of terms should be chosen to be able to fill the MoM matrix. Hence a trade off must be made between the solution accuracy and the computational cost by choosing an optimal truncation number. In order to cope with huge computational burden, Ewald's transformation is incorporated into the solution. Using the Ewald's transformation, the solution can be accelerated by expressing periodic Green's function as a sum of spatial and spectral series,

$$G_p\left(\mathbf{r},\mathbf{r}'\right) = \sum_{m=-\infty}^{\infty}\sum_{n=-\infty}^{\infty} G_{mn}^{\text{spatial}}\left(\mathbf{r},\mathbf{r}'\right) + \sum_{m=-\infty}^{\infty}\sum_{n=-\infty}^{\infty} G_{mn}^{\text{spectral}}\left(\mathbf{r},\mathbf{r}'\right). \tag{3.18}$$

The convergence of the Ewald's method depends on a splitting parameter. Using either a larger or a smaller splitting parameter would increase the convergence rate of spatial or spectral series, respectively [42]. An optimum splitting parameter, E, is chosen as

$$E = \max\left\{\sqrt{\frac{\pi}{A}}, \frac{k}{2H}\right\} \tag{3.19}$$

where H is the maximum value of the exponent of the series [42]. In this study, $H = 3$ is chosen. For the propagating modes that satisfy $k_{zmn}^2 > 0$, the spectral term, G_{mn}^{spectral}, can be defined as [43]

$$\begin{aligned} G_{mn}^{\text{spectral}}\left(\mathbf{r},\mathbf{r}'\right) =& \frac{e^{-j\mathbf{k}_{tmn}\cdot(\rho-\rho')}}{2Ak_{zmn}}\Bigg[e^{-k_{zmn}(z-z')} + e^{-(k_{zmn}/(2E))^2-((z-z')E)^2} \\ & \times j\text{Im}\left\{\text{w}\left(\frac{jk_{zmn}}{2E} + j(z-z')E\right)\right\}\Bigg]. \end{aligned} \tag{3.20}$$

For the evanescent modes that satisfy $k_{zmn}^2 < 0$, it becomes [43]

$$\begin{aligned} G_{mn}^{\text{spectral}}\left(\mathbf{r},\mathbf{r}'\right) =& \frac{e^{-j\mathbf{k}_{tmn}\cdot(\rho-\rho')}}{4Ak_{zmn}}\Bigg[\text{erfc}\left(\frac{k_{zmn}}{2E} + (z-z')E\right)e^{k_{zmn}(z-z')} \\ & + \text{erfc}\left(\frac{k_{zmn}}{2E} - (z-z')E\right)e^{-k_{zmn}(z-z')}\Bigg]. \end{aligned} \tag{3.21}$$

In these equations, $\mathrm{erfc}(z)$ is the complementary error function, and $\mathrm{w}(z)$ is called Faddeeva function, a modified type of the complementary error function such that

$$\mathrm{erfc}(z) = e^{-z^2}\mathrm{w}(jz). \tag{3.22}$$

The spatial term for the periodic Green's function of Ewald's series, G_{mn}^{spatial}, also becomes [43]

$$\begin{aligned} G_{mn}^{\text{spatial}}(\mathbf{r},\mathbf{r}') = {} & \frac{e^{-j\mathbf{k}_{t00}\cdot\rho_{mn}}}{8\pi R_{mn}} e^{-(R_{mn}E)^2+(k/(2E))^2} \\ & \times \left[\mathrm{w}\left(jR_{mn}E - \frac{k}{2E}\right) + \mathrm{w}\left(jR_{mn}E + \frac{k}{2E}\right)\right]. \end{aligned} \tag{3.23}$$

As can be expected, there is a singularity in the spatial term when $m = n = 0$ and the source point is in vicinity of the observation point, i.e., $\mathbf{r} \approx \mathbf{r}'$. The first exponential term in (3.23) vanishes when there is singularity due to the fact that $\rho_{00} = 0$. The singularity can be extracted by dividing (3.23) into two terms as

$$\begin{aligned} G_{mn}^{\text{spatial}}(\mathbf{r},\mathbf{r}') = {} & \frac{1}{8\pi R_{mn}}\left\{e^{-(R_{mn}E)^2+(k/(2E))^2}\left[\mathrm{w}\left(jR_{mn}E - \frac{k}{2E}\right)\right.\right. \\ & \left.\left. + \mathrm{w}\left(jR_{mn}E + \frac{k}{2E}\right)\right] - 2\right\} + \frac{1}{4\pi R_{mn}} \\ = {} & \tilde{G}_{mn} + \frac{1}{4\pi R_{mn}}. \end{aligned} \tag{3.24}$$

The second term in (3.24) can be solved analytically as discussed in Chapter 2. The singularity of the first term in (3.24) can be handled when $R_{mn} \to 0$ as

$$\lim_{Rmn \to 0}\left\{\tilde{G}_{mn}\right\} = \frac{1}{4\pi}\left\{e^{(k/(2E))^2}\left[jk\mathrm{w}\left(\frac{-k}{2E}\right) - \frac{2E}{\sqrt{\pi}}\right] - jk\right\}. \tag{3.25}$$

The convergence of the Ewald's transformation of the periodic Green's function is compared with the convergence of the spatial domain periodic Green's function for the FSS element of Jerusalem cross. Dimensions of the unit cell geometry is obtained from [44] and shown in Fig. 3.4. In this comparison, the reflection coefficient of the fundamental mode of Jerusalem cross unit cell is calculated as a function of T, which is the truncation number of the infinite double summation. Note that since summation limits from $-\infty$ to $+\infty$ are approximated as from $-T$ to $+T$, there are $(2T + 1)^2$ terms left in the series. In Fig. 3.5a, the reflection coefficient is calculated at 6 GHz, under y-polarized normal incidence with spatial domain periodic Green's function.

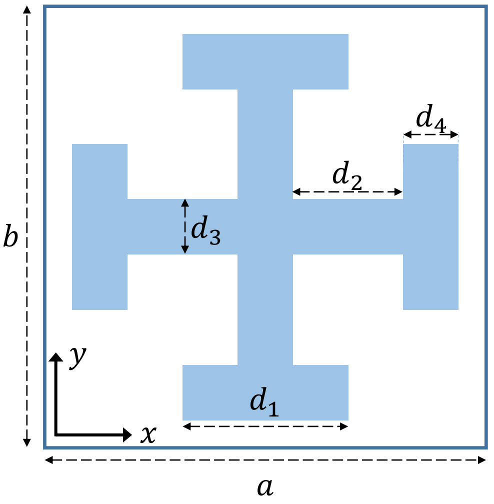

Figure 3.4: Frequency selective surface element of Jerusalem cross with dimensions $d_1 = 5.7$ mm, $d_2 = 3.8$ mm, $d_3 = d_4 = 1.9$ mm, inside square unit cell of $a = b = 15.2$ mm.

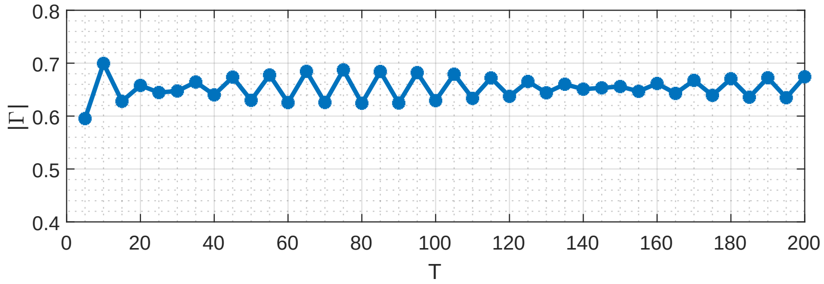

(a)

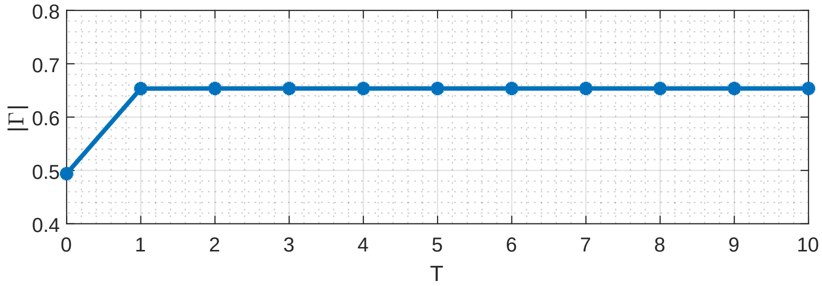

(b)

Figure 3.5: Reflection coefficient of Jerusalem cross unit cell at 6 GHz, as a function of T (a) Spatial domain periodic Green's function. (b) Ewald's transformation of periodic Green's function.

On the other hand in Fig. 3.5b, the solution is performed with Ewald's transformation of the periodic Green's function. The convergence of the reflection coefficient found with spatial Green's function seems very slow compared to the solution with Ewald's method. Ewald's transformation prevents a large computational burden since the double summation already converges at $T = 1$ which corresponds to sum of only 9 terms. Therefore Ewald's periodic Green's function is utilized in the analysis of the unit cell problem throughout this work.

In order to validate the accuracy of the unit cell analysis, the solution of the FSS element of Jerusalem cross illuminated by x-polarized normal incidence is compared with FEKO's results at the frequency range of 1 to 14 GHz. As seen from Fig. 3.6, the result from the MoM solution of the periodic unit cell with Ewald's method is in agreement with the result obtained from the commercial simulation tool.

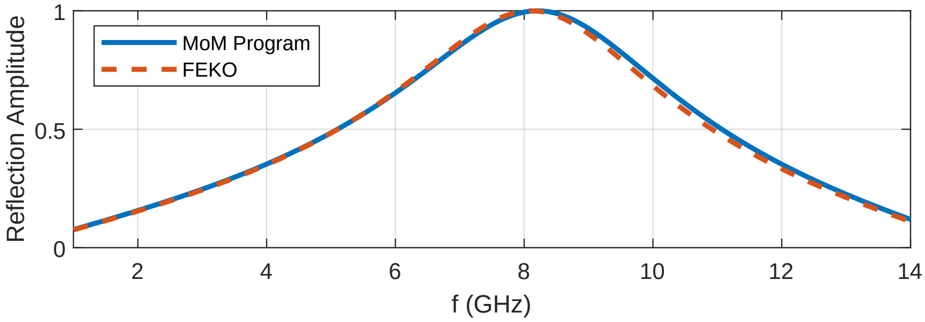

(a)

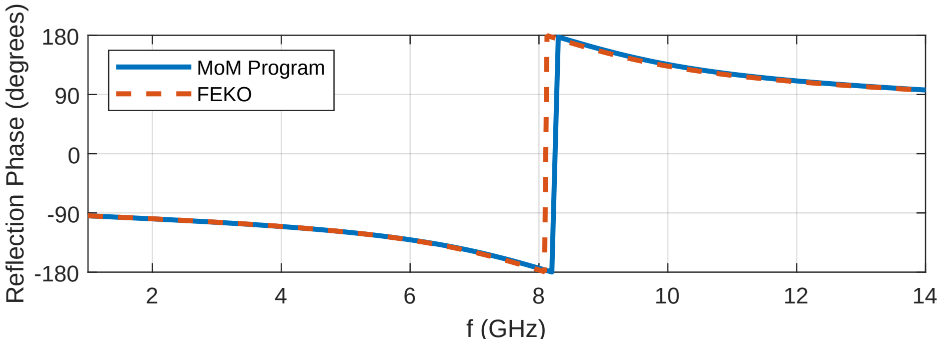

(b)

Figure 3.6: Reflection coefficient of Jerusalem cross unit cell element illuminated by x-polarized normal incidence, compared with FEKO's results. (a) Magnitude. (b) Phase.

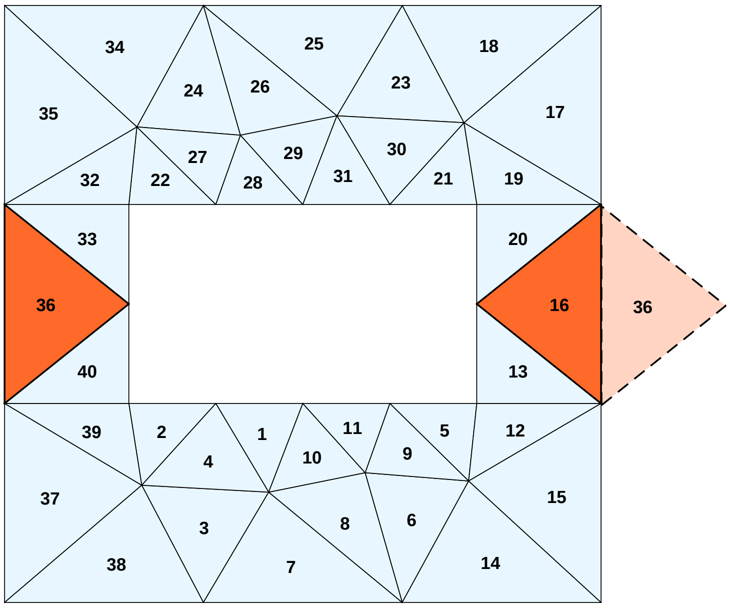

Figure 3.7: Triangular mesh connections on the periodic boundary.

3.1.4 Continuity on the Unit Cell Boundary

In the unit cell solution, unless the elements touch the periodic boundary, the element discretization can be done as discussed in Section 2.2.4. However as the triangular mesh resides on the periodic boundary, a special treatment is needed to satisfy the continuity of the surface current on the unit cell boundary.

In order to maintain the continuity, the triangular mesh residing on the boundary is constructed such that edges of triangles coinciding with the opposite sides of boundary are defined in equal lengths and in mirror symmetry [45]. Therefore additional basis functions can be defined with triangles on the opposite sides of the unit cell. As illustrated in Fig. 3.7, an additional RWG element can be defined with 36th triangle on the left and 16th triangle on the right. In this very specific example, 6 additional RWG elements must be formed by triangles of opposite sides and utilized along with the rest of RWG elements that defined inside the unit cell.

3.2 Characteristic Mode Analysis of the Unit Cell

Since the generalized equation in (2.40) is independent of the excitation, the characteristic mode analysis of finite elements is also free of excitation as discussed in Section 2.3. However since the periodic Green's function is dependent on the excitation due to the transverse component of the wave vector, the MoM impedance matrix has also become dependent on the excitation. Therefore the characteristic mode analysis of the unit cell solution is not only dependent on the element shape and wavelength, but also the incident wave impinging over the unit cell element.

In the characteristic mode analysis of Jerusalem cross unit cell element for the x-polarized normal incidence, the eigenvalues, modal significance values and the characteristic angles for the first 2 characteristic modes within the band of 1 to 14 GHz are depicted in Fig. 3.8. Because 3rd and higher order modes have very large eigenvalues and negligibly small modal weighting coefficients for the given excitation, such higher order modes can be omitted from this analysis.

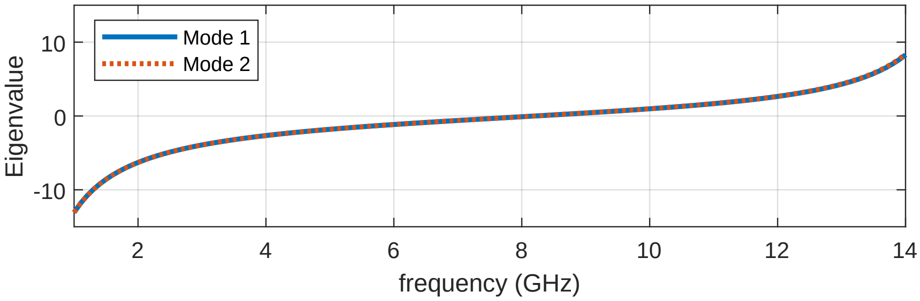

(a)

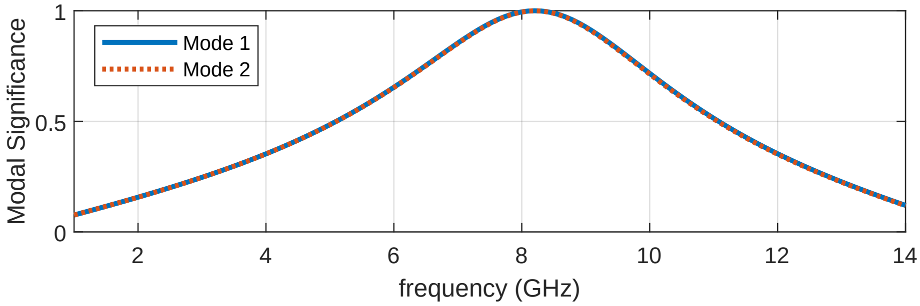

(b)

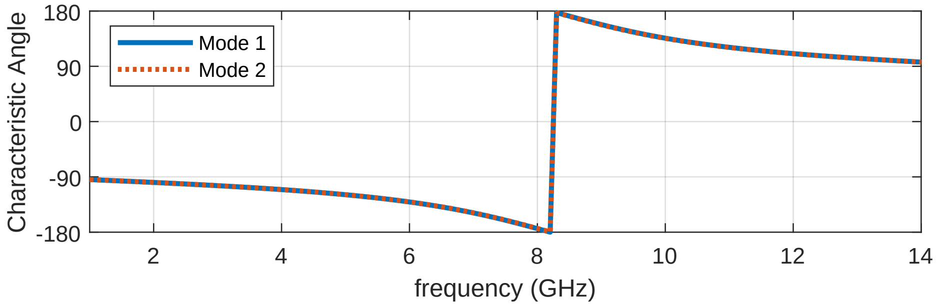

(c)

Figure 3.8: The first 2 modes of Jerusalem cross unit cell element, illuminated by x-polarized normal incidence. (a) Eigenvalues. (b) Modal significance values. (c) Characteristic angles.

As reflection coefficient values in Fig. 3.6 and the first 2 modes in Fig. 3.8 are compared, one can observe that modal significance values of the first 2 modes are exactly equal to the magnitude of the reflection coefficient. Similarly characteristic angles of the first 2 modes yield the phase of the reflection coefficient. These preliminary results indicate that characteristic modes can be exploited in Floquet analysis of periodic unit cell element.

In the solution of Jerusalem cross, a symmetrical element with respect to x and y coordinates, is utilized within the square unit cell. Besides that, it is also illuminated by normal incidence, i.e. $\theta_i = 0$, which is also a symmetrical excitation with respect to x and y coordinates. For this reason, two characteristic modes have exactly the same real eigenvalues over the frequency band. Since both modes share the same eigenvalues, they can be referred as degenerate modes. Modal surface currents of two degenerate modes under y-polarized normal incidence is given in Fig. 3.9. As can be inferred from the directions of the current flow, the modes are $90°$ out of phase.

In order to deepen the analysis, same unit cell element given in Fig. 3.4 is solved for an oblique incidence. In this case, a plane wave of $\theta_i = 30°$ is utilized as

$$\mathbf{E^i}(\mathbf{r}) = \left(-\hat{\mathbf{x}}\cos\theta_i + \hat{\mathbf{z}}\sin\theta_i\right) e^{jkx\sin\theta_i + jkz\cos\theta_i}. \tag{3.26}$$

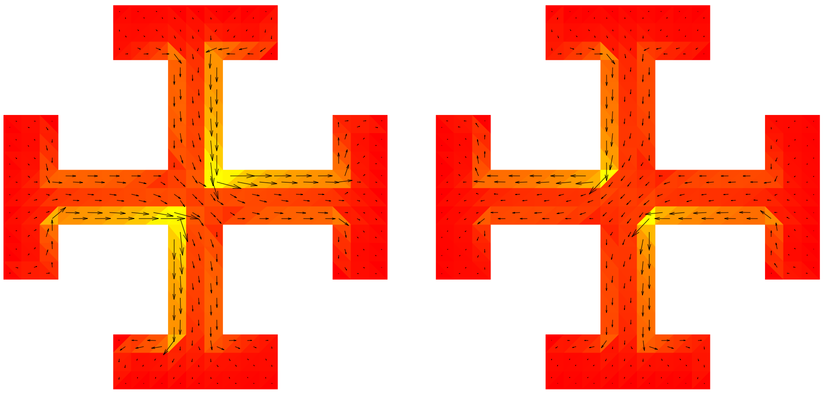

(a) (b)

Figure 3.9: Modal current on Jerusalem cross unit cell element, illuminated by y-polarized normal incidence. (a) 1st mode. (b) 2nd mode.

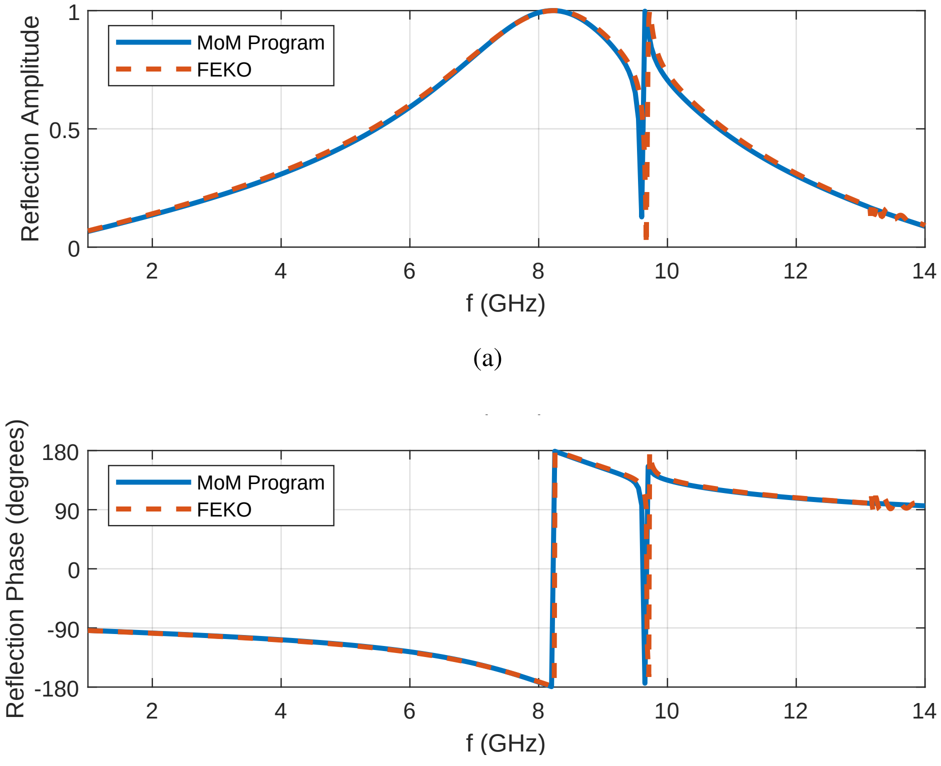

(a)

(b)

Figure 3.10: Reflection coefficient of Jerusalem cross unit cell element, illuminated by (3.26) with $\theta_i = 30°$. (a) Magnitude. (b) Phase.

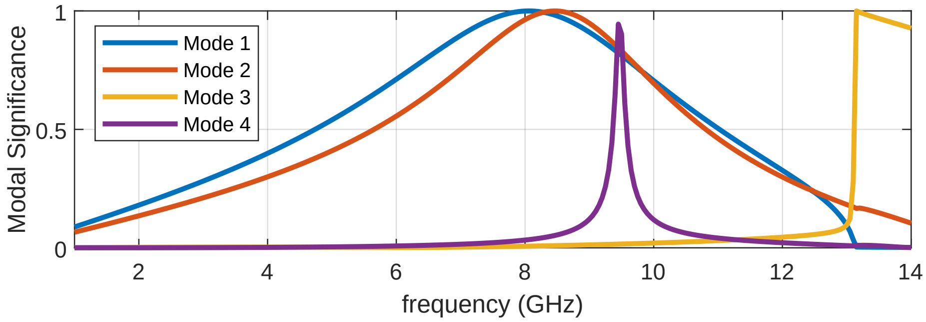

(a)

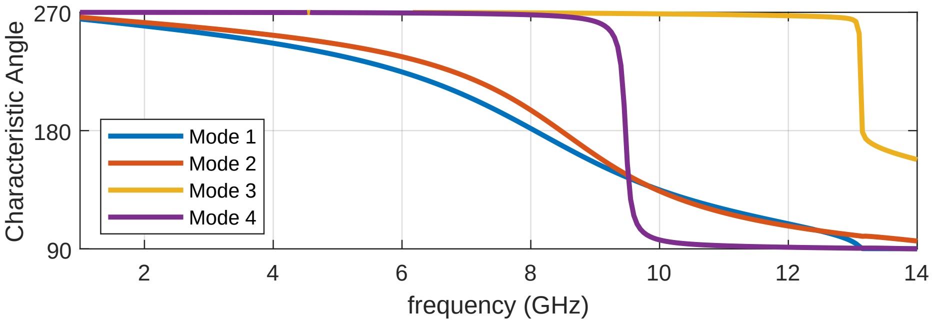

(b)

Figure 3.11: The first 2 modes of Jerusalem cross unit cell element, illuminated by (3.26) with $\theta_i = 30°$. (a) Eigenvalues. (b) Modal significance values. (c) Characteristic angles.

The reflection coefficient for the oblique incidence is given in Fig. 3.10 at the band of 1 to 14 GHz. The solution is also validated for the oblique case by comparing results with FEKO's results in the same figure. Since the electric field is along the direction of propagation due to the definition in (2.26), Floquet mode of TM00 is excited. The most obvious outcome of the oblique incidence is the abrupt change of the reflection behavior around 9.7 GHz.

In order to understand this behavior, the characteristic mode analysis is performed. The modal significance values as well as the characteristic angles for the first 4 modes are given in Fig. 3.11. Similar to the case of normal incidence, the first 2 modes are dominant modes almost the entire band. Because of the unsymmetrical nature of the problem due to the oblique excitation, eigenvalues of these two modes are not exactly the same but slightly different. The 3rd mode can also be neglected up to

13 GHz since the contribution to the solution is very small. On the other hand, 4th mode becomes resonant around 9.7 GHz. Although the bandwidth of the 4th mode is very narrow, it affects the reflection performance of the FSS element in the case of oblique incidence, hence explains the abrupt change of the reflection at this frequency. Moreover, the behavior of the all 4 characteristic modes is completely changed at 13.16 GHz. The reason is the higher order Floquet modes. As discussed in Section 3.1.2, circles that represent higher order modes are intersecting with the inner circle of the dominant mode having the radius of $|k \sin \theta_i|$, thus the inequalities in (3.10) no longer hold at frequencies higher than 13.16 GHz. Because higher order modes are also contributing to the surface current induced on the unit cell element above their cut-off frequency, reflection behavior of the unit cell changes, so does the behavior of the characteristic modes in the unit cell.

In the design of large periodic structures such as frequency selective surfaces, metamaterial absorbers and artificial impedance surfaces, the goal is to provide the desired reflection and transmission properties over the desired frequency band. However since such structures are expected to provide the desired performance not only at the case of normal incidence but also at oblique incidences up to some degree, it is important to understand the change of reflection and transmission properties as the scan angle varies. As demonstrated above with the FSS element of Jerusalem cross, the change of the incidence angle from 0 to 30° excites the 4th characteristic mode. This example indicates that the performance of the unit cell element illuminated by incident fields of varying angles can be analyzed with the help of the characteristic mode analysis. For instance, in order to make the FSS structure of Jerusalem cross yield the same reflection results for both scan angles of $\theta_i = 30^\circ$ and $\theta_i = 0$, one can consider suppressing the excitation of the 4th characteristic mode. As the suppression of the characteristic modes has already been studied for antenna problems by utilizing inductive loads [46] and metasurfaces [47], such methods can also be extended into the periodic unit cell problem.

3.2.1 Modal Analysis of Reflectarray Elements

In this section, the characteristic mode analysis of periodic unit cell elements is investigated for the design and analysis of reflectarray elements. In the reflectarray antenna, the goal is to produce a pencil beam towards the desired direction. Thus a phase distribution must be created on the antenna surface accordingly. To do this, the geometrical parameters of the elements can be adjusted so that the incident wave impinging on each element reflects with a specific phase.

Usually the reflectarray elements are chosen to provide a phase range of minimum $360°$. The reflectarray element can consist of either 2-layer as a single layer of element backed by a ground plane, or multilayer of elements in which each element acts as a resonant circuit thus a phase range larger than $360°$ can be achieved [48]. In the following examples, characteristic mode analyses for ground backed metal-only slot-type elements are given to discuss the modal characteristics of the reflectarray elements. Unlike the FSS examples above, the behavior of the modes are evaluated not according to the frequency but the tuning parameter that adjusts the phase response of the element. Hence the mode tracking algorithm discussed in Section 2.3.1 is implemented with respect to the tuning parameter. The work demonstrated in this section has also been presented in [49] and [50].

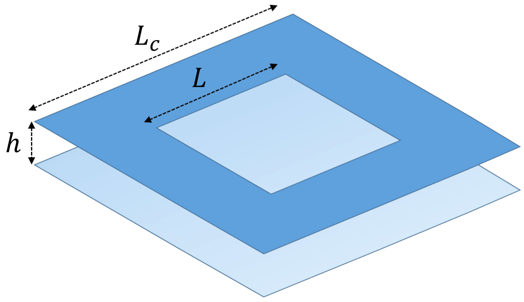

Figure 3.12: Geometry of the square slot reflectarray unit cell element.

The first example of the reflectarray unit cell element is a square slot that is depicted in Fig. 3.12 [51]. Desired phase distribution with such type of element is obtained by adjusting the slot dimension. The unit cell problem is solved at 12.5 GHz inside the square unit cell of $L_c = 12$ mm, under y-polarized normal incidence. The phase response of the element is given in Fig. 3.13 as a function of the slot size of L and

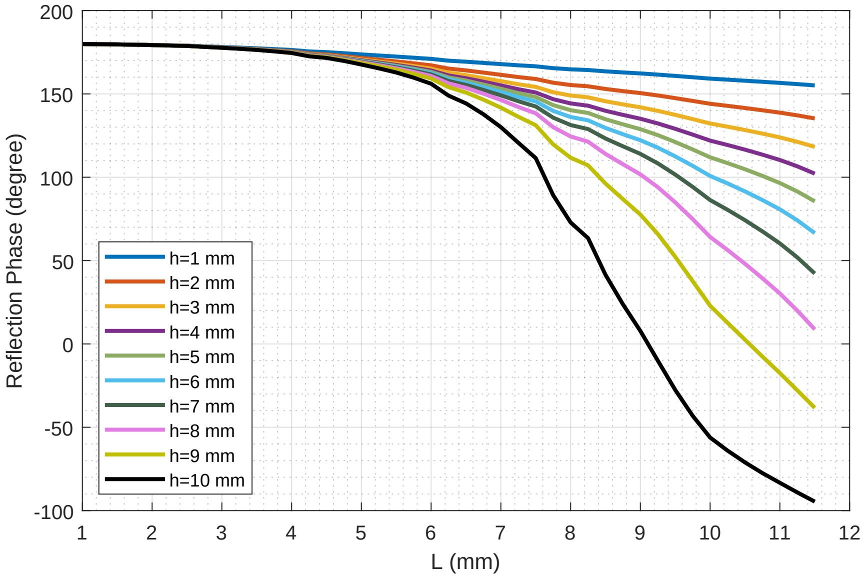

Figure 3.13: Reflection phase of the square-slot unit cell reflectarray element illuminated by normal incidence as a function of the slot dimension.

varying ground heights, h, from 1 mm to 10 mm. The results indicate that when the slot is very small, the reflection phase is 180° regardless of the height, as if the wave is reflected from an infinite ground plane. As the slot dimension increases, the reflection phase begins to vary. Although the phase range increases as the height from the ground plane increases, the total range from $L = 1$ to 11.5 mm is still 275° at $h = 10$ mm, which is not sufficient for the reflectarray antenna design since minimum 360° of range is required for a proper design. Note that since the metal element is PEC and no dielectric material is included, neither metallic nor dielectric losses affect the results. Hence the magnitude of the reflection coefficient becomes equal to 1. Although there is no substrate between the ground plane and the slot element, it can be physically realized by printing copper elements on styrofoam-like materials that have very low relative permittivity.

It can be recalled from the previous section that only the first 2 characteristic modes can be excited on the Jerusalem cross element in the visible scan region where only the fundamental Floquet modes are allowed to propagate. However in the solution of the square-slot reflectarray element, the first 4 characteristic modes can be excited due to the 2-layer structure.

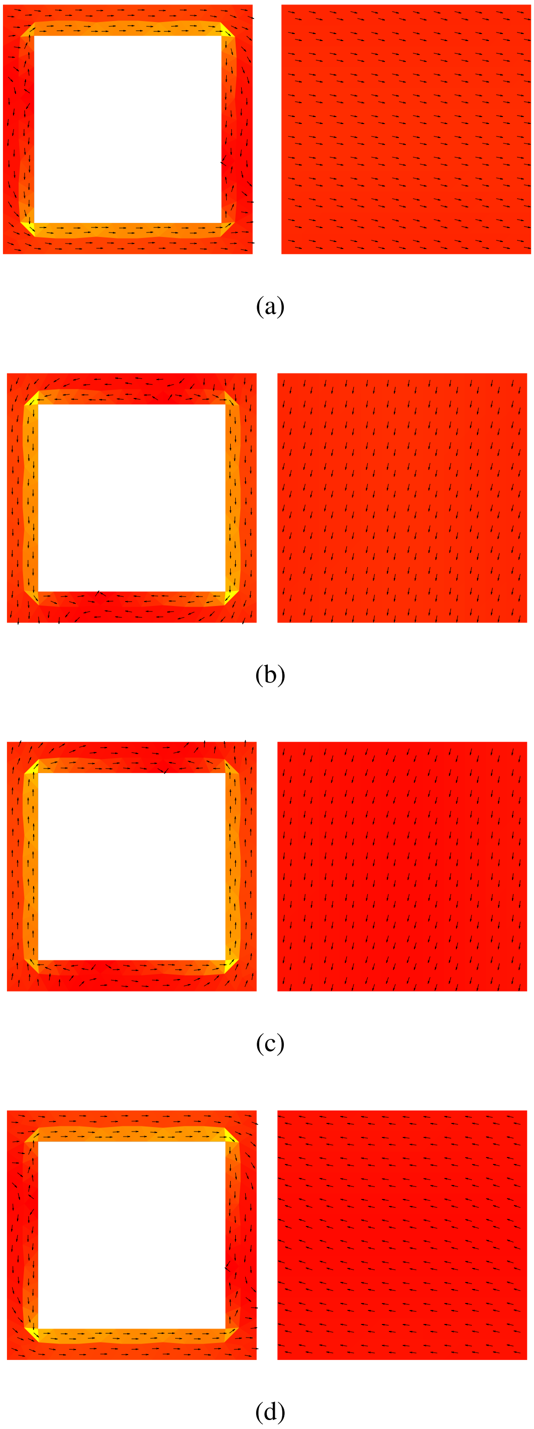

Figure 3.14: Modal currents on the square slot reflectarray element for the case of $h = 5$ mm $L = 9$ mm.. (a) Mode 1. (b) Mode 2. (c) Mode 3. (d) Mode 4.

Due to the mirror symmetry of the element with respect to the x and y coordinates, as well as the normal incidence, the 1st and 2nd modes, and similarly the 3rd and 4th modes yield the same eigenvalues. It means that the first 4 characteristic modes are obtained as 2 pairs of degenerate modes. To provide a better insight, the modal currents associated with these modes are depicted in Fig. 3.14 when $h = 5$ mm and $L = 9$ mm. Note that in these depictions, the sizes of the arrows are kept particularly equal to emphasize the direction of the current flows on both layers.

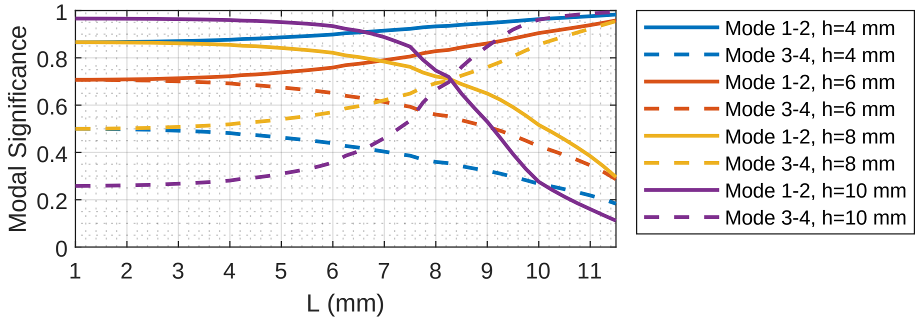

(a)

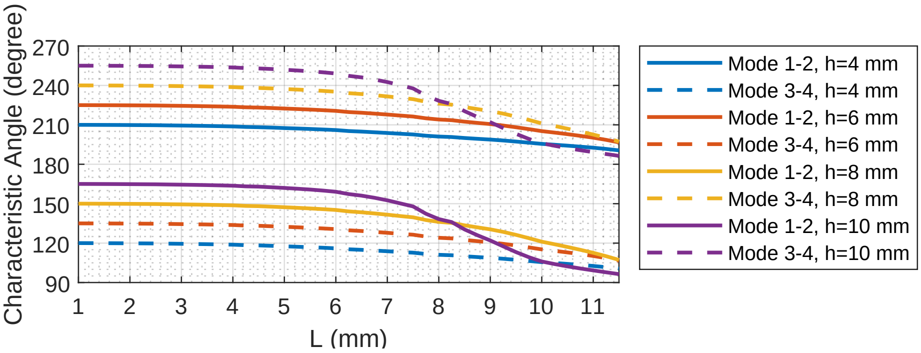

(b)

Figure 3.15: The first 4 modes of the square-slot unit cell element, illuminated by normal incidence as a function of the slot dimension. (a) Modal significance values. (b) Characteristic angles.

In Fig. 3.15a and 3.15b, the modal significance values and the characteristic angles associated with these 4 modes are plotted, respectively, as a function of the slot dimension for different heights. It can be deduced from the results that the height of the elements from ground plane as well as the size of the square slot dramatically affect the eigenvalues of the solution. When the height is 4 mm, the modal significance values of the first two modes are closer to 1, and the next two modes are close to 0. Moreover, characteristic angles are varying very slowly similar to the phase of the reflected field. However as the height increases from 4 mm to 10 mm, eigenvalues change more rapidly as a function of L. At the case of $h = 10$ mm, the modal significance values intersect at some point around $L = 8.5$ mm. Therefore we can conclude that as the reflection phase varies more rapidly as a function of L, so do the eigenvalues of the excited modes. Unlike the single layer Jerusalem Cross FSS element, the values of modal significance and characteristic angle do not yield the magnitude and phase of the reflected field, respectively. However as can be observed from Fig. 3.15, the modal significance values for the two-layer reflectarray elements satisfy

$$\sqrt{\mathrm{MS}_{1,2}^2 + \mathrm{MS}_{3,4}^2} = 1 \tag{3.27a}$$

$$|\vartheta_{1,2} - \vartheta_{3,4}| = 90^\circ. \tag{3.27b}$$

These equations indicate that 1st and 3rd modes as well as 2nd and 4th modes can be considered as the components of the dominant Floquet modes. Although the solution is performed under the y-polarized illumination, the square-slot element would yield the same reflection phase for either x-polarized or y-polarized incidence due to the symmetry with respect to the x and y coordinates and resulting 2 pairs of degenerate modes.

In order to observe 4 distinct characteristic modes of different eigenvalues as well as different reflection responses according to the polarization, one can disturb the symmetry of the geometry by simply implementing a rectangle-slot element instead of the square-slot. In the next example, square-slot element illuminated by a y-polarized normal incidence is compared with a rectangle-slot element which is illuminated by the x and y polarized normal incidences to observe the effect of the polarization over the reflected field as well. Again the solution is performed inside the square unit cell of $L_c = 12$ mm at 12.5 GHz. The rectangle slot is $L + 2$ mm along the x coordinate and L mm along the y coordinate. Both solutions for the rectangle and square slots are performed when the height of the elements from the ground plane, h, is 10 mm. The results are presented in Fig. 3.16. It can be seen from the figure that the reflection phase of the rectangle slot becomes equal to the square slot element as long as the slot edge lengths are equal in the direction perpendicular to the polarization.

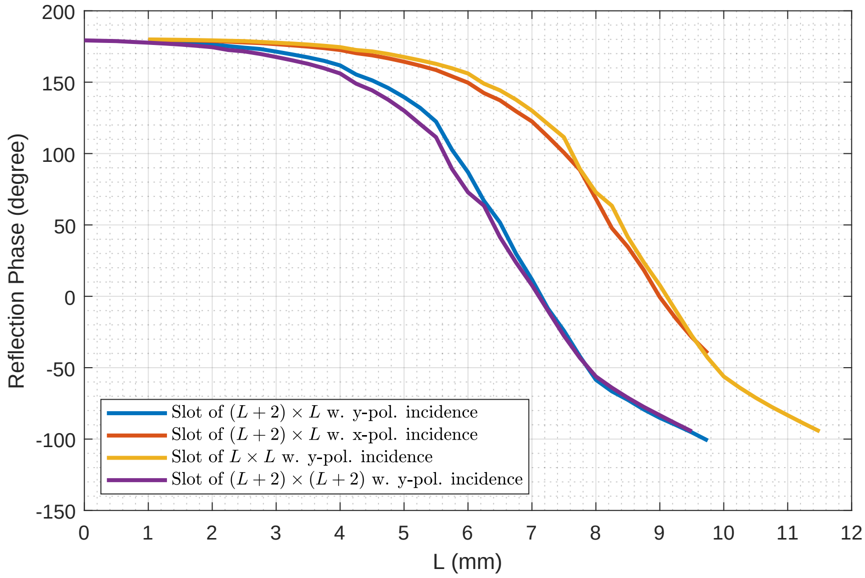

Figure 3.16: Comparison of the reflection phase for the rectangular-slot and square-slot elements, illuminated by normal incidence, as the function of the slot size.

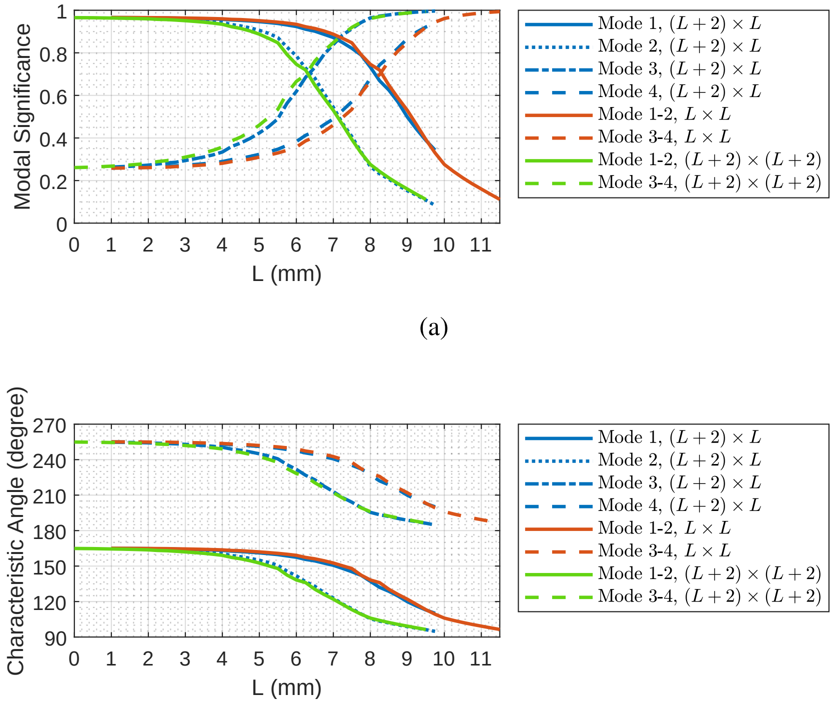

(a)

(b)

Figure 3.17: Comparison of the characteristic modes for the rectangular-slot and square-slot elements illuminated by normal incidence as a function of the slot size. (a) Modal significance values. (b) Characteristic angles.

In Fig. 3.17, the modal significance values as well as the characteristic angles for the first 4 distinct eigenvalues of the rectangle-slot element are compared with degenerate modes of the square-slot element. It can be seen that the 1st and the 4th mode of the rectangle-slot element is aligned with first 2 and the next 2 degenerate modes of the $L \times L$ square-slot element. Similarly the 2nd and the 3rd mode of the rectangle-slot element is aligned with first 2 and the next 2 degenerate modes of $(L+2) \times (L+2)$ square-slot element. This analysis indicates that the difference between the 1st and the 2nd mode as well as the difference between the 3rd and the 4th mode comes from the dimensions of the slot edges observed along the x and y directions.

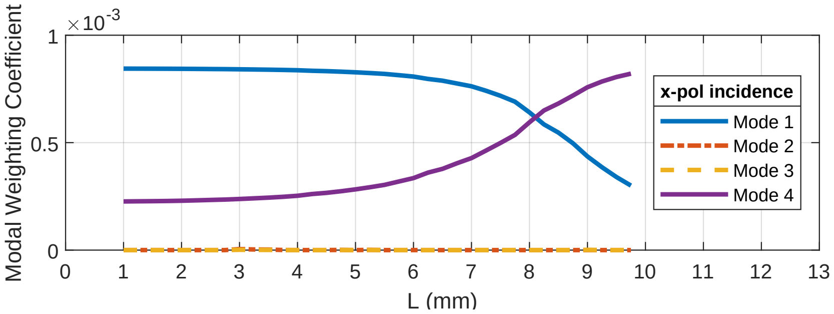

(a)

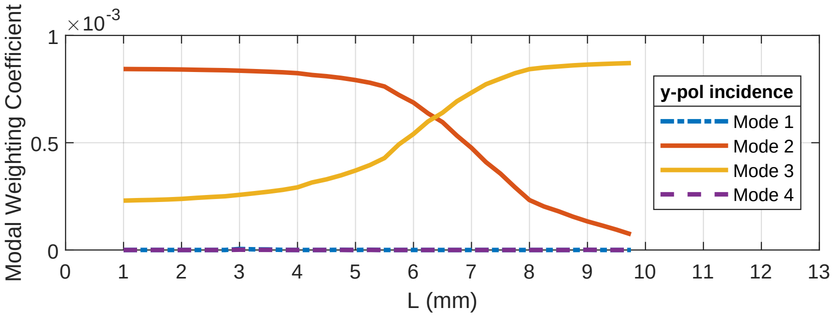

(b)

Figure 3.18: Modal weighting coefficients of the rectangle-slot unit cell element as a function of the slot size. (a) Illuminated by x-polarized normal incidence. (b) Illuminated by y-polarized normal incidence.

Depending on the polarization of the incident electric field, only one of the first 2 modes and one of the next 2 modes model the surface current on the unit cell elements. More specifically, as the rectangle-slot element of $(L+2) \times L$ is illuminated by the

x-polarized normal incidence, the modes of the rectangle slot elements are aligned with the square-slot of $L \times L$. Hence in the case of x-polarization, the 1st and the 4th CMs of the rectangle slot element are excited. Similarly the 2nd and the 3rd modes are excited when the incidence is y-polarized. This can also be observed from the modal weighting coefficients of the corresponding modes, which are also given in Fig. 3.18.

In the last example of the reflectarray unit cell element, the square-slot element is modified by adding a square ring element in the middle of the slot to obtain the double-slot unit cell element, as depicted in Fig. 3.19. Similar to the previous example, the unit cell is a square of $L_c = 12$ mm, and solved under normal incidence at 12.5 GHz. The thickness of the ring is chosen as $w = 0.5$ mm. The phase shifting parameter is the edge length of the square ring element, L. The purpose of this element is to enhance the phase range, which makes it more convenient in a reflectrarray design. It is also possible to incorporate an additional square patch at the middle of the ring, hence not only the edge length of the ring element, but also the size of the patch, as well as the thickness of the ring element can become the phase-shifting parameter. In fact, such element is a well known reflectarray element, known as Phoenix element [51, 52]. However using only an additional ring element without the additional patch is also sufficient to yield the desired phase range in this analysis.

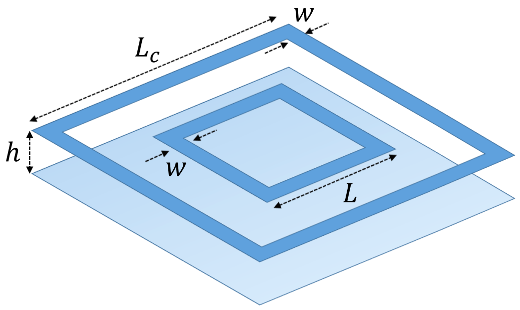

Figure 3.19: Geometry of the double-slot unit cell element.

In Fig. 3.20, the reflection phase of the double slot element is given for different heights from the ground plane. Unlike the single slot-type element, the phase range is $360°$ regardless of the element height from the ground plane. However as the height increases, the phase curves are getting flatter. Since reflectarray element design with

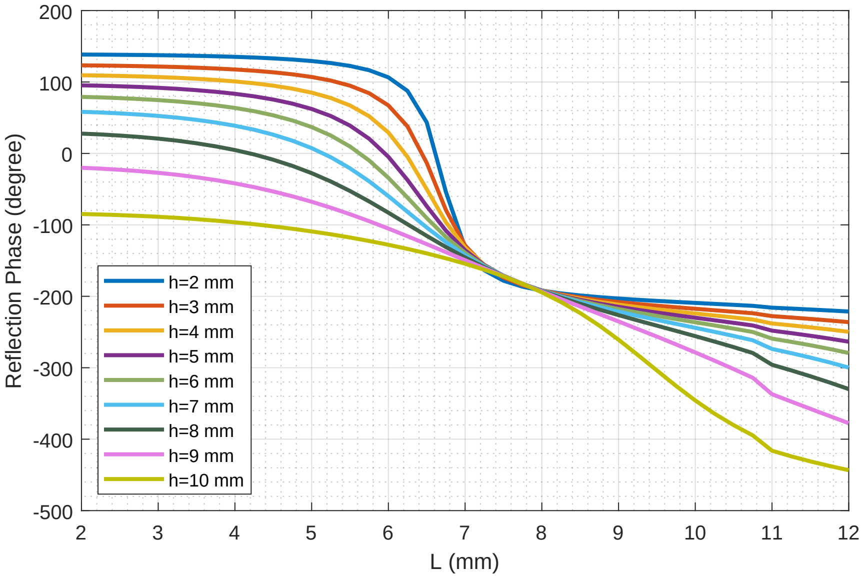

Figure 3.20: Reflection phase of the double-slot unit cell element, illuminated by normal incidence as a function of the edge length.

steep phase slopes would reduce the design accuracy and makes the structure more dependent on manufacturing tolerances, larger h seems more advantageous to make the phase response curves flatter. Similar behavior can also be observed in eigenvalues as a function of the phase shifting parameter. As shown in Fig. 3.21, there are 4 excited modes in which the first two and the next two modes are degenerate characteristic modes that satisfy (3.27). In this analysis, as the height from the ground plane increases, the variation of the modal significance values between 0 and 1 becomes smoother. Therefore similar behavior between the variation of the character-

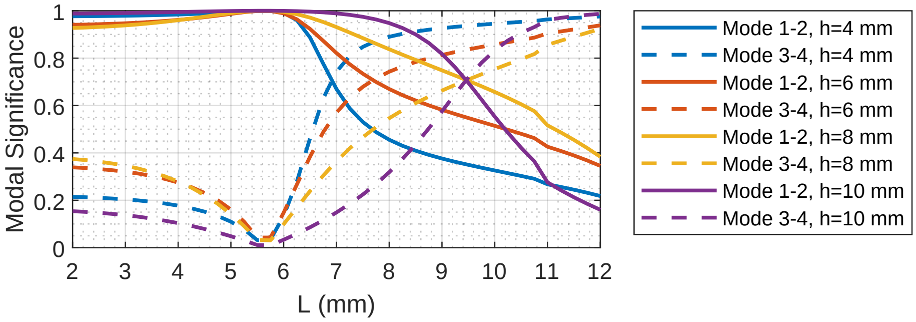

Figure 3.21: Modal significance values of the double-slot unit cell element, illuminated by normal incidence, as a function of the edge length.

istic modes and variation of the phase response depending on the tune parameter can also be observed in the double-slot element.

As a conclusion, both single and double slot-type elements indicate that the characteristic mode analysis of the unit cell can be performed to understand the behavior of the reflectarray unit cell elements. Since the phase range of $360°$ along with gradual phase variation is desired for a good design of reflectarray, one should excite the characteristic modes of the unit cell element such that the eigenvalues vary very gradually over a wide range of the tuning parameter. As a design methodology, it may also be considered to suppress modes with eigenvalues that do not comply with this behavior.

CHAPTER 4

REACTIVE LOADING ON UNIT CELL ELEMENTS

Reactive loading has been utilized in the antenna design for many years. Using reactive elements, scattered and radiating field from the electric conductor can be controlled [53]. In the antenna design, reactive load elements are used for various reasons including the reduction of back-scattering [54–56], adjustment of the bandwidth [57], and electronic beam-steering [58, 59]. They can be applied with lumped elements as well as stub elements, or by opening slot elements on the conductive surfaces. Especially in the design of microstrip antennas, it is possible to achieve dual-band radiation using coaxial stubs [60] and slots [61], or to adjust the input impedance by adding short-circuit loads [62].

The reactive loading using the characteristic modes is introduced by Roger F. Harrington [10]. In [10], a load matrix has been incorporated into the generalized eigenvalue equation. By calculating the load distribution that makes the eigenvalue zero, it has become possible to turn a reactive mode into a resonant mode at the desired frequency. Hence, the bandwidth and the radiation of an antenna can be tuned by exciting such mode with the help of the reactive load matrix. Nevertheless, reactive loads calculated by the load matrix must be applied over all basis functions in the solution domain, which is usually not realizable. Although implementing lumped loads on wire antennas can be considered only if few basis functions are defined in the solution domain, it is still not preferable due its difficulty in the implementation. An example of continuous loading for a thin wire dipole can be found in [63]. Although tuned stubs and slots can also be considered instead of lumped elements, it would also be very difficult, if not impossible, to apply specific reactance values this way. In order to circumvent this pitfall, such problem is usually turned into an N-port scattering problem [11, 64]. Then it is possible to express the generalized eigenvalue equation in terms of an N-port network in which few lumped elements can be realized on network ports [12,13,65]. In [14], the network characteristic modes (NCM) is utilized in order to construct desired antenna current using a finite number of impedance loads. In [66], the design of loaded pattern reconfigurable antenna is demonstrated using the characteristic mode analysis. In [67], a method is developed to modify eigenvalue behaviour of the modes using loads on the dipole element. It is usually difficult to find optimal reactive loads that yields desired electrical characteristics. To address this problem, the NCM is combined with differential evolution algorithm [68]. Although adding desired reactance values into the problem by modifying the antenna geometry is quite challenging, a design procedure is also developed to optimize slotted patch elements [69].

Besides the antenna design, reactive loads can also become useful in the design of frequency selective surfaces (FSS). In the early applications of frequency selective surfaces, capacitive and inductive responses were obtained by constructing grids and meshes in electrically small periodicity. However with the development of numerical solution methods over time, periodic structures that consist of elements in various geometries such as ring, linear dipole, cross and Jerusalem cross [70–73] are studied. Especially the analysis of such elements in terms of equivalent lumped circuit models has provided good understanding of how such elements behave under electromagnetic illumination [74]. Further analyses have also paved the way for more complicated elements including concentric rings [75], double square loop patches [76–78] and complementary arrays [79, 80]. Similarly, capacitive and inductive loading elements are also utilized on FSS elements to be able to tune reflection and transmission characteristics as well as provide an active control, or achieve element miniaturization [81–86].

A wide variety of optimization algorithm [81] can be implemented to determine not only the element parameters but also values for the load elements. In fact, commercial EM simulation tools offer many conveniences for implementing optimization algorithms. Apart from that, a systematic design method is given in [87], that yields the values for reactive elements with parameters of the structure for the desired band of operation. As an alternative to complex methods that require the use of optimization algorithms, a systematic approach has been sought to calculate discrete load values for ring-type FSS elements as well as their complementary slot-type elements using the theory of the characteristic modes.

4.1 The Continuous Loading

The generalized eigenvalue equation of (2.40) can be written as

$$(\mathbf{X} + \mathbf{X_L})\mathbf{J_n} = \lambda_n \mathbf{R}\mathbf{J_n} \tag{4.1}$$

where $\mathbf{X_L}$ is the reactive load matrix which is chosen to be a diagonal matrix within Galerkin's method,

$$\mathbf{X_L} = \begin{bmatrix} X_{L1} & 0 & 0 & ... & ... \\ 0 & X_{L2} & 0 & ... & ... \\ 0 & 0 & X_{L3} & ... & ... \\ ... & ... & ... & \ddots & ... \\ ... & ... & ... & ... & X_{LN} \end{bmatrix} \tag{4.2}$$

such that each diagonal element defines a reactive load on the corresponding basis function. As already discussed in Section 2.3, a mode becomes resonant when its eigenvalue is equal to zero. In this context, the diagonal elements can be defined to satisfy $\lambda_n = 0$ at any desired frequency. Since setting eigenvalues to zero would make the equation (4.1) equal to zero, diagonal elements can be calculated as

$$X_{Li} = -\frac{\{\mathbf{X} \cdot \mathbf{J_n}\}_i}{\{\mathbf{J_n}\}_i} \tag{4.3}$$

where $\{\quad\}_i$ defines ith entry of the vector that corresponds to the ith basis function.

In order to demonstrate this method, an FSS element of circular ring is utilized as an example. The geometry of the element is given in Fig. 4.1 in which 48 RWG elements along with 48 triangles are defined on its surface. The reflection coefficient and the modal significance values of the first 2 modes are plotted in Fig. 4.2a and 4.2b, respectively, for an x-polarized normal incidence. It can be seen that total reflection occurs at 14.8 GHz. Similar to the Jerusalem cross example, only the first 2 modes are excited and yield the same eigenvalues due to the symmetry with respect to the x and

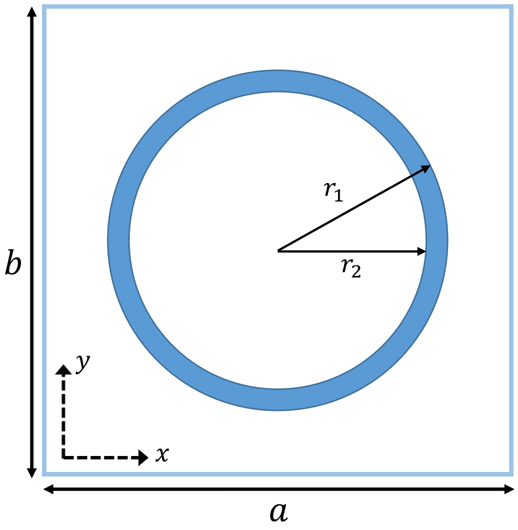

Figure 4.1: FSS element of circular ring with dimensions $r_1 = 4$ mm and $r_2 = 3.5$ mm, inside the square unit cell of $a = b = 11$ mm.

y directions. Modal significance values of the first 2 modes are exactly equal to the reflection magnitude throughout the band. It means that the generalized eigenvalue equation, (2.40), is equal to zero when there is total reflection.

Assume that the total reflection is desired to be shifted from 14.8 to 10 GHz. To do this, the first step is to observe modal currents in Fig. 4.3. It can be seen that the 1st modal current on the FSS element is in the x direction and the 2nd modal current is in the y direction. Since the problem is considered under the x-polarized incidence, the 1st mode must be modified to achieve total reflection performance at 10 GHz. In this respect, the resonance frequency of the 1st characteristic mode must be shifted from 14.8 to 10 GHz. For this purpose, the reactance load matrix which would make (4.1) equal to zero, is calculated at 10 GHz.

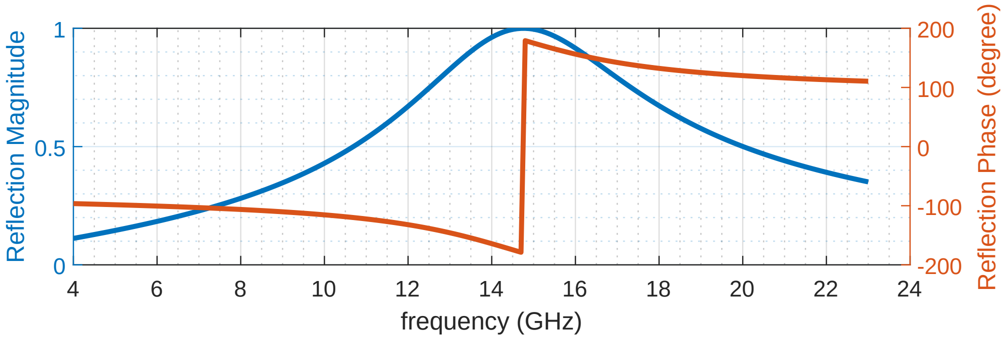

(a)

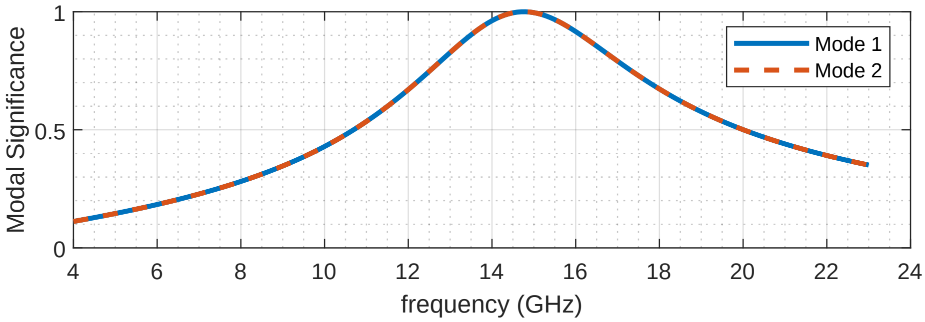

(b)

Figure 4.2: Circular ring element, illuminated by an x-polarized normal incidence. (a) Reflection coefficient. (b) Modal significance values.

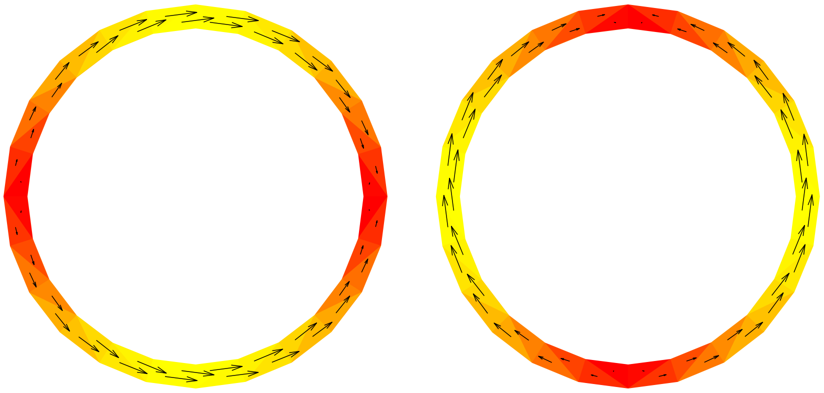

(a) (b)

Figure 4.3: Modal current on the circular ring element, illuminated by an x-polarized normal incidence at 10 GHz. (a) 1st mode. (b) 2nd mode.

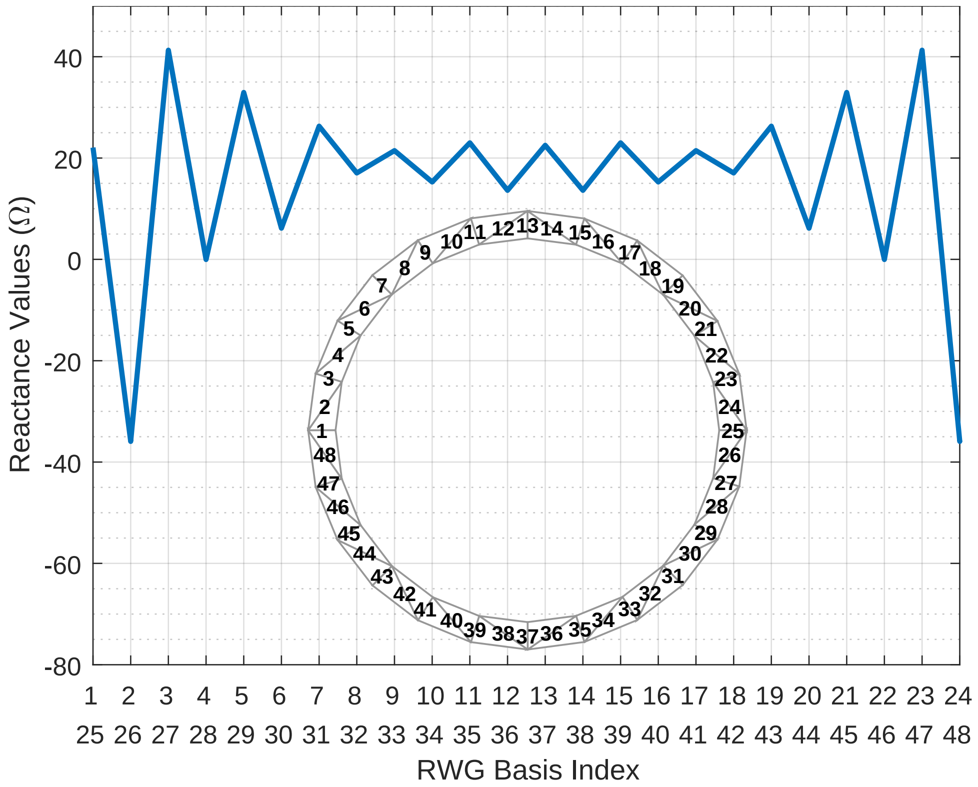

Figure 4.4: Continuous reactive loading of RWG elements.

To find the load values, the diagonal load matrix elements are divided by the square of the RWG element lengths [41] such that

$$X_i = \frac{X_{Li}}{l_i^2} \tag{4.4}$$

where X_i is the reactance value of the ith RWG and l_i is the edge length as described in Fig. 2.2. The definition of the RWG elements and the corresponding load values that would shift the total reflection point from 14.8 to 10 GHz are shown in Fig. 4.4. Assuming the center of the ring as the origin of the Cartesian coordinate system, it can be seen that load values are in mirror symmetry with respect to both x and y axes.

After applying the continuous load distribution into the impedance matrix, the modified reflection coefficient and modal significance values are obtained as in Fig. 4.5a and 4.5b, respectively. It can be seen from the figure that the first 2 modes no longer yield the same eigenvalues. The resonance frequency of the 1st and 2nd modes are shifted from 14.8 to 10 GHz and 11.3 GHz, respectively. Since the 1st mode corresponds to the x-polarized incidence, the reflection magnitude of the continuously loaded unit cell element is expected to follow the pattern of the 1st mode. Indeed

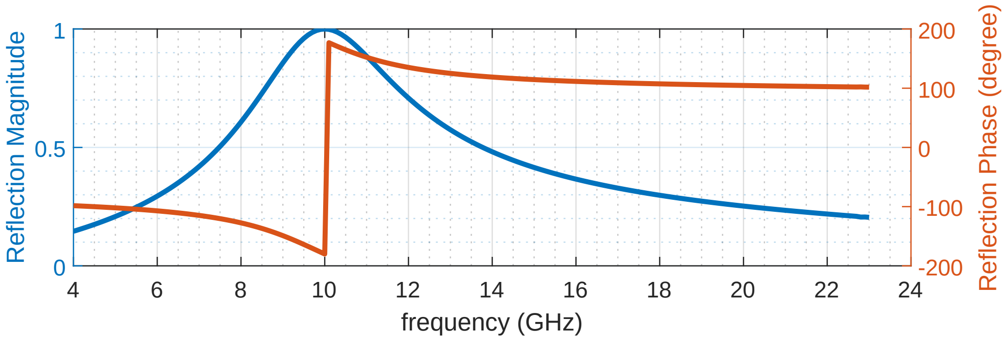

(a)

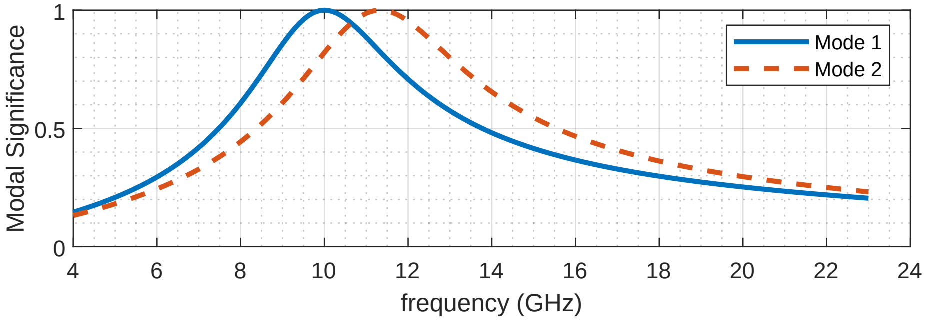

(b)

Figure 4.5: Continuously loaded circular ring element, illuminated by an x-polarized normal incidence. (a) Reflection coefficient. (b) Modal significance values.

the reflection coefficient is exactly equal to the modal significance value of the 1st mode. Therefore the shift of the total reflection frequency from 14.8 to 10 GHz is successfully demonstrated by applying the continuous loading.

Although the reflection characteristics of the unit cell element can be controlled by this method, it is not practical to use 48 lumped elements on each periodic array element. One solution is to use coarser mesh at the cost of the accuracy. However, since the lumped elements obtained on a very coarse mesh would not be sufficiently accurate, all loading values should be further optimized. Therefore load values cannot be implemented directly but can only be used as initial values for an optimization algorithm. Another approach may be etching slots on the element surface, but applying load values in terms of slots would become a very complicated task.

A more reliable solution would be to use fewer loads that will yield a similar effect of the load distribution over the unit cell element. In fact, it would be sufficient to use the reactive loads only on the locations where the magnitude of the surface current is large. In the next section, a novel approach is introduced to obtain two load values that can be applied at the nodes of the element where the magnitude of the induced current becomes maximum, due to the linearly polarized illumination.

4.2 The Discrete Loading Approach on Ring-Type Elements

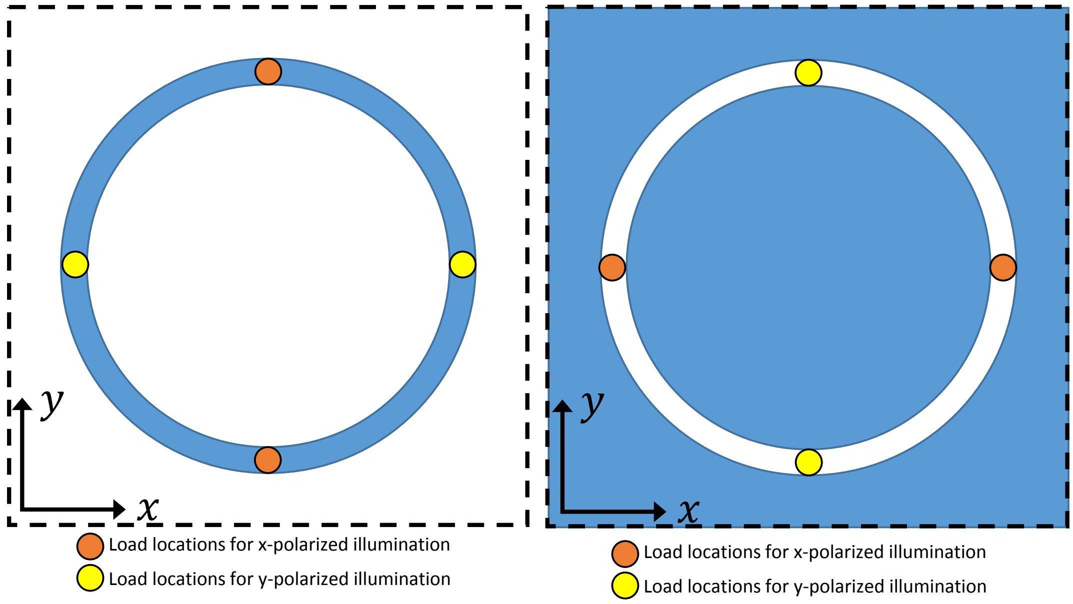

(a) (b)

Figure 4.6: Load locations for x and y-polarized plane waves (blue areas refer to the conducting surface). (a) Metal ring element. (b) Complementary problem of the metal ring element as the slot ring element.

Determining the locations of reactive loads is challenging in antenna problems. However, for periodic elements such as frequency selective surfaces, the most convenient regions to apply loads would be those with the highest currents. Since the radiation behavior of the element is determined by the induced current, loads applied to the nodes where the current peaks would affect the radiation behavior drastically. For the same reason, the effect of the loads on the radiation will be negligible when they are applied in the null regions where the current is very low.

When a ring-type element is illuminated by a linearly polarized plane wave, the maximum current occurs in the section of the element where the flowing direction is parallel to the electric field vector. Thus, as depicted in Fig. 4.6a, loads must be applied at northernmost-southernmost and easternmost-westernmost nodes of the ring element for x and y-polarized electric fields, respectively. In the complementary problem of the ring element as a slot element, the loads must be applied in the opposite nodes, as shown in Fig. 4.6b. This situation will also be discussed in the next section.

Nevertheless the main problem is to reduce the continuous load distribution into two loads that will yield the desired frequency shift of the continuous loading. Although impracticality of the continuous loading is pointed out in the literature [63], no suggestion has been made so far to reduce such load distribution into a few number of loads. However only in this study, a direct method is proposed to obtain two reactive loads using the continuous load distribution.

As the domain discretization is performed such that each triangle is used by only two RWG basis elements, it is possible to take an average of the load distribution. Note that in the case when each triangle defines only two RWGs, the total number of RWG elements becomes equal to the total number of triangles. In the case of the ring-type element where two loads are applied 180 degrees apart, the geometry can be divided into two equal semi-rings due to mirror symmetry and only one load can be approximated using half of the load distribution over the semicircle. Hence, the value for the two discrete loads can be approximated as

$$X_d = \frac{1}{2} \sum_{i=1}^{N} \delta_i X_i \tag{4.5}$$

where δ_i is the coefficient for each continuous load value. These coefficients determine how effective the continuous load values are to the radiation of the element for the given polarization.

4.2.1 Obtaining Coefficients of the Continuous Load Distribution

Undoubtedly one of the important aspects that determines the accuracy of the method is to find proper coefficients to take an average of the load distribution. The effect of the distributed loads to the unit cell performance is vastly dependent on the current density on the element surface. The load values in the region where the current is high are decisive in the frequency shift. On the other hand, load values correspond to the RWG elements located in the null regions of low current would not affect the band of the unit cell element, hence they can be omitted when finding discrete load values. Considering the x-polarized illumination as an example, the magnitude of the current induced in the x direction would increase towards northernmost and southernmost nodes. Hence, the effect of load elements would be higher if applied on the nodes that are close to the northernmost and southernmost nodes. Therefore, for the x-polarized incidence, it is preferable to choose lower coefficient values correspond to RWG elements that are close to $y = 0$ axis and higher values for elements that are far away from $y = 0$ axis.

In this respect, the values for the coefficients are calculated from the current of the mode-of-interest. To be able to use this approach, the maximum and minimum nodes of the modal current must also follow the polarization of the incidence. In other words, the direction of the surface current induced by an incident wave must be in the same direction with the modal current of the mode-of-interest. Hence, if the direction of the current of kth mode is aligned with the polarization of the incidence, the coefficients for the load distribution is formulated according to the kth mode. If $\mathbf{J_k}$ is the eigenvector, the modal current, $\mathbf{I_k}(\mathbf{r}')$, on each triangle can be calculated by multiplying corresponding RWG basis functions with corresponding eigenvector entries as

$$\mathbf{I_k}(\mathbf{r}') = \sum_{i=1}^{N} \{\mathbf{J_k}\}_i \mathbf{f_i}(\mathbf{r}') \tag{4.6}$$

where $\mathbf{r}'$ is the center coordinate of each triangle. Once the modal current is calculated on each triangle, the vector of $\bar{\mathbf{I}}_k$ is constructed. The ith entry of this vector, $\{\bar{\mathbf{I}}_k\}_i$, is defined as the arithmetic mean of the modal currents calculated on two triangles that form the ith RWG element. Then the proposed coefficients for the load distribution are calculated as the entries of the vector, $\mathbf{\Delta}$,

$$\mathbf{\Delta} = \frac{\left|\bar{\mathbf{I}}_k\right| \mathbf{J}_k}{\max\left\{\left|\bar{\mathbf{I}}_k\right| \mathbf{J}_k\right\}}. \tag{4.7}$$

Since the vector defined in the numerator of the fraction in (4.7) is divided by its largest entry, all of the coefficients range from 0 to 1.

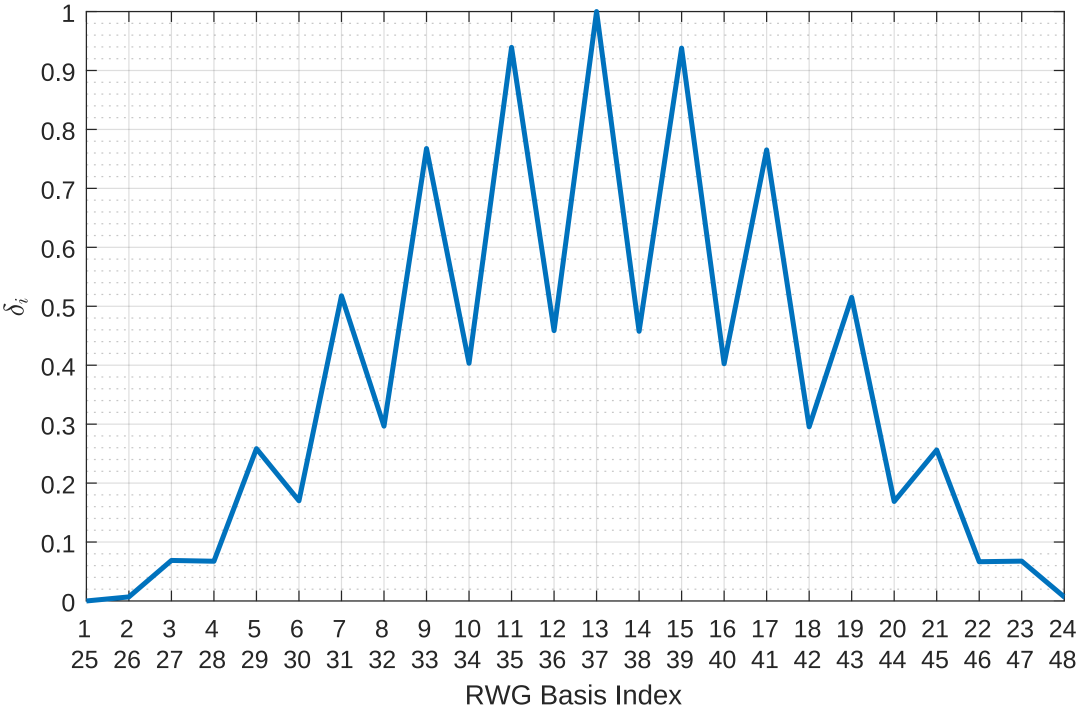

Figure 4.7: Coefficients of the continuous load distribution.

Following this procedure, coefficients of the continuous load values for the given example can be found as in Fig. 4.7. Substituting the values in Fig. 4.4 and Fig. 4.7 in the equation (4.5), $X_d = 184.85\ \Omega$ is calculated. The positive X_d can be realized as the inductance of $L_0 = X_d/\omega$, and similarly the negative X_d can be utilized as the capacitance of $C_0 = -1/(X_d\omega)$. In this example, since the sign of the reactance value is positive, it can be realized as an inductance of $L_0 = 2.942$ nH at 10 GHz.

After inductive load of $L_0 = 2.942$ nH is applied at the northernmost and southernmost nodes, the reflection coefficient as well as the modal significance values for the first two modes are calculated. The results are given in Fig. 4.8. As can be seen from the figure, the total reflection point is shifted from 14.8 to 10 GHz similar to the case of the continuous distribution. Again the magnitude of the reflection coefficient follows the pattern of the modal significance of the 1st mode. However, unlike the case of continuous loading, the modal significance of the 2nd mode has not been shifted elsewhere from 14.8 GHz. The reason is that the second mode corresponds only to the y- polarized incidence. Hence, loading only the northernmost and southernmost nodes of the ring element does not affect the 2nd mode and the reflection behavior at

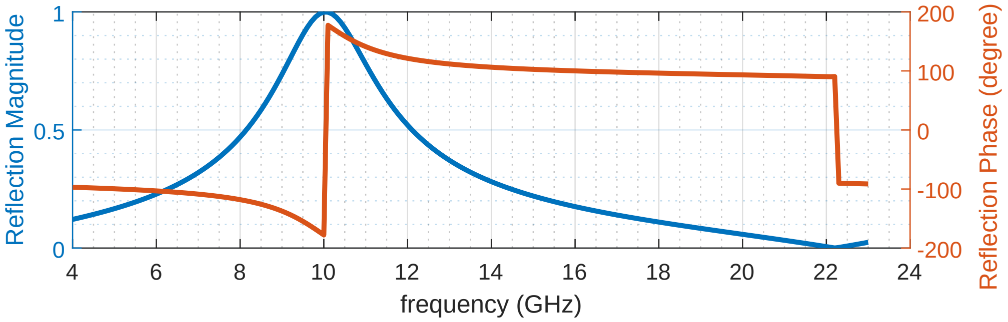

(a)

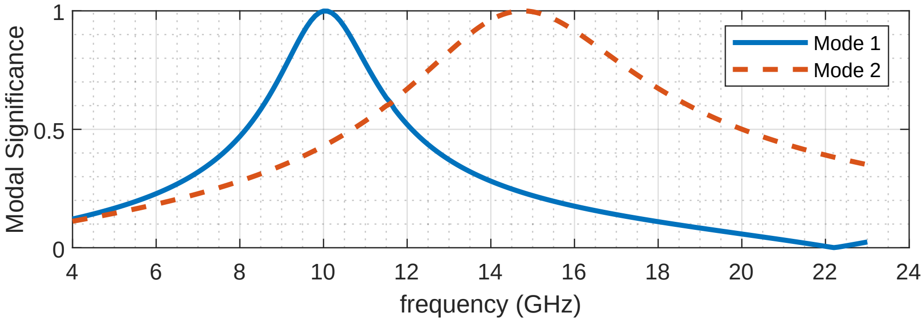

(b)

Figure 4.8: Two discrete loads applied on the circular ring element, illuminated by an x-polarized normal incidence. (a) Reflection coefficient. (b) Modal significance values.

the case of y-polarized illumination.

4.2.2 The Complementary Slot Problem

In the periodic unit cell analysis, the complementary problem of the ring-type metal element is the ring-type slot element that is cut out from the ground plane. The introduced method of finding discrete loads cannot be utilized directly on the slot-type elements. Therefore, the most logical approach would be to exploit the complementary problem. The characteristic mode analysis of aperture/slot problem has already been introduced for infinitely long apertures [88–90]. In [91], the aperture problem is formulated for MoM admittance matrix. In [92], the modal analysis of the slotted planar antenna is demonstrated over both infinite and finite ground planes. Thus the characteristic mode analysis of the slot problem can be defined by the equivalent magnetic current approach. If the MoM admittance matrix, $\mathbf{Y}$, is defined as

$$\mathbf{Y} = \mathbf{G} + j\mathbf{B} \tag{4.8}$$

the characteristic mode decomposition can be expressed as

$$\mathbf{B}\mathbf{M}_n = \lambda_n \mathbf{G}\mathbf{M}_n \tag{4.9}$$

where $\mathbf{M}_n$ is the magnetic modal current. The orthogonality relations can also be stated as

$$< \mathbf{M}^*_{\mathbf{m}}, \mathbf{G}\mathbf{M}_{\mathbf{n}} > = \delta_{mn} \tag{4.10a}$$

$$< \mathbf{M}^*_{\mathbf{m}}, \mathbf{B}\mathbf{M}_{\mathbf{n}} > = \lambda_n \delta_{mn} \tag{4.10b}$$

$$< \mathbf{M}^*_{\mathbf{m}}, \mathbf{Y}\mathbf{M}_{\mathbf{n}} > = (1 + j\lambda_n)\delta_{mn}. \tag{4.10c}$$

However, instead of computing the admittance matrix and reformulating the solution according to equivalent magnetic currents, the principle of duality can also be exploited. If the duality principle is used in the finite aperture problem, the solutions of metal patch and its complementary aperture would differ since the effect of the finite plate size cannot be omitted in the aperture problem. However, this is not the case in the unit cell solution since the unit cell problem is defined assuming infinite periodicity. Therefore, in the unit cell solution, the dual problem can be considered by converting the EFIE into its dual form [93, 94]. Dual quantities to convert the problem of the conducting element into the problem of the complementary slot element is summarized in Table 4.1. In this table, $\mathbf{A}$ refers to the magnetic vector potential as defined in (2.3) and used in the case of the electric source over the conducting element. Similarly, $\mathbf{F}$ represents the electric vector potential that utilized in the case of magnetic current sources over the slot element. By substituting dual quantities into (2.22), the impedance matrix becomes

$$\begin{aligned} \mathrm{Z}^{\mathrm{F}}_{\mathrm{mn}} = \frac{1}{j\omega\mu} \int_{Sm} d\mathbf{r} \, \left[\nabla \cdot \mathbf{f}^F_m(\mathbf{r})\right] \int_{Sn} d\mathbf{r}' \, \nabla' \cdot \mathbf{f}^F_n(\mathbf{r}') G\left(\mathbf{r}, \mathbf{r}'\right) \\ + j\omega\epsilon \int_{Sm} d\mathbf{r} \, \mathbf{f}^F_m(\mathbf{r}) \cdot \int_{Sn} d\mathbf{r}' \mathbf{f}^F_n(\mathbf{r}') G\left(\mathbf{r}, \mathbf{r}'\right) \end{aligned} \tag{4.11}$$

as the integral domain is defined over the slot region. The duality principle can also be applied on the characteristic modes. Hence the magnetic current and the radiated

Table 4.1: Dual quantities

Conducting element	Complementary slot element
$\mathbf{A}$	$\mathbf{F}$
$\mathbf{J}$	$\mathbf{M}$
$\mathbf{E^A}$	$\mathbf{H^F}$
$\mathbf{H^A}$	$-\mathbf{E^F}$
ϵ_0	μ_0
μ_0	ϵ_0

fields can be defined as weighted sums of modal dual currents and modal dual fields, respectively as

$$\mathbf{M} = \sum_n a_n^F \mathbf{M}_n \tag{4.12a}$$

$$\mathbf{E}^F = \sum_n a_n^F \mathbf{E}_n^F \tag{4.12b}$$

$$\mathbf{H}^F = \sum_n a_n^F \mathbf{H}_n^F \tag{4.12c}$$

where

$$a_n^F = \frac{< \mathbf{M}_n, \mathbf{H}^i >}{1 + j\lambda_n^F}. \tag{4.13}$$

One favorable outcome of the dual problem is that eigenvalues of both problems are equal to each other [93],

$$\lambda_n^A = \lambda_n^F. \tag{4.14}$$

This result indicates that characteristic modes of the metal element and the complementary slot element resonate at the same frequency. Therefore, by finding the loads on the metal element to shift the modal band to the desired frequency, the modal band of the slot element can also be shifted to the same frequency. As also discussed in [93], the relation between inductive/capacitive loads of the metal element and capacitive/inductive loads of the slot element can be presented as

$$C_0^F = \frac{4}{\eta^2} L_0^A \tag{4.15a}$$

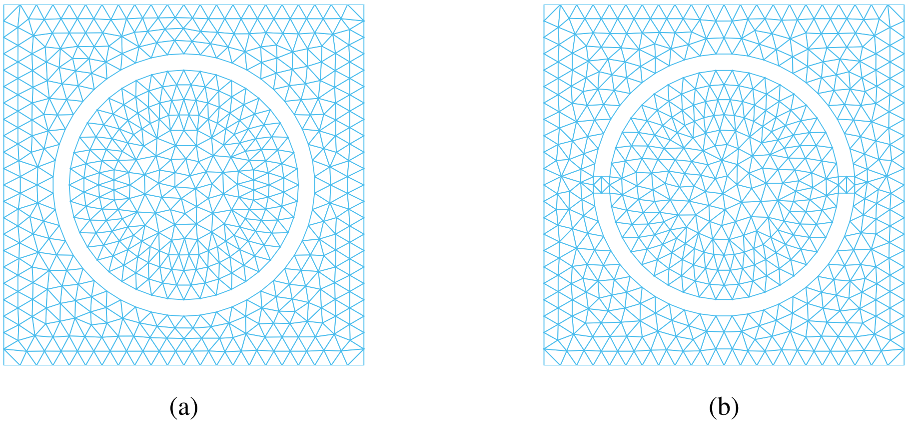
(a)

(b)

Figure 4.9: Meshing of the ring-type slot element (a) Load-free element. (b) Loaded element.

$$C_0^A = \frac{4}{\eta^2} L_0^F. \tag{4.15b}$$

Since the dual problem yields the same eigenvalues, the modal significance values in the metal element and the complementary slot element are also the same. Because amplitude and phase of the reflection coefficient values follow the modal significance and characteristic angle values of one of the dominant modes, respectively, the reflection coefficient of the slot problem can be computed by considering only the complementary metal counterpart. In this respect, the reflection coefficient of the FSS metal element becomes equal to the transmission coefficient of its complementary slot element, and vice versa. This suggests that by solving the metal ring element and finding discrete inductive loads that shift the total reflection frequency to a desired frequency, one would also obtain the discrete capacitive loads that would shift the total transmission frequency to the same frequency for the slot counterpart. Since the scattered electric field of the one problem is proportional to the scattered magnetic field of its dual, the problem of x-polarized incidence over the metal ring corresponds to the problem of y-polarized incidence over the complementary slot ring, or vice versa. Therefore the load locations on the ring-type metal element and the ring-type slot element must be 90 degrees apart.

As an example, the complementary slot of the same metal element from the previous example is utilized and illuminated by an x-polarized plane wave. Because the

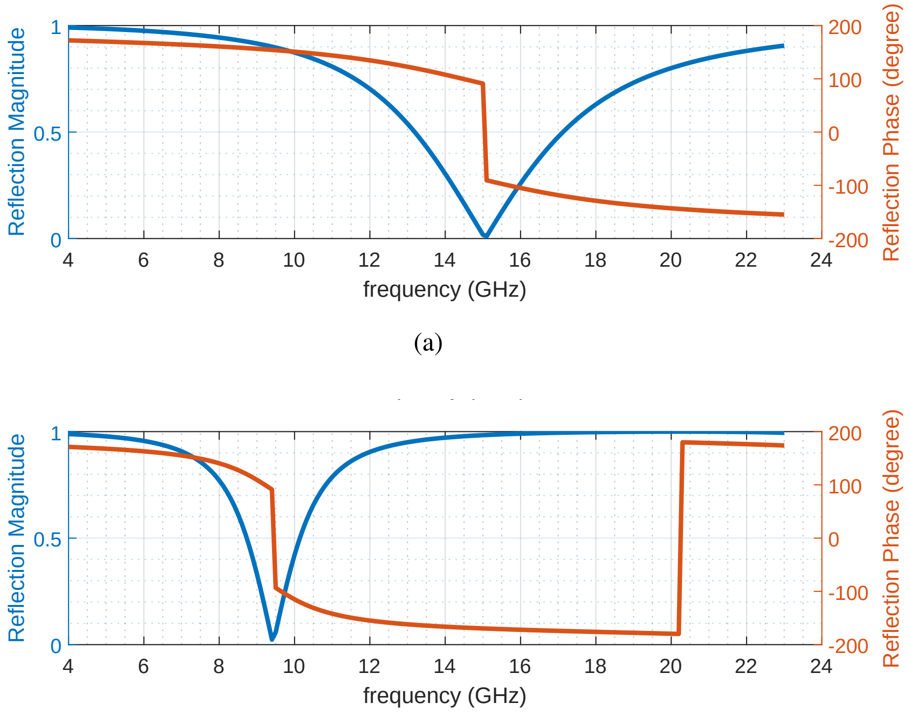

(a)

(b)

Figure 4.10: Reflection coefficient of the slot ring element, illuminated by an x-polarized normal incidence. (a) Unloaded element (b) Capacitive loaded element.

incidence is x-polarized, loads on the complementary slot element are placed at easternmost and the westernmost nodes of the slot as already discussed in Fig. 4.6b. As depicted in Fig. 4.9, additional meshes are included on the slot to be able to define loads. Because $L_0 = 2.942$ nH is the inductive load that shifts the total reflection frequency from 14.8 to 10 GHz, the value of the capacitance loads that would shift the total transmission frequency of the slot element from 14.8 to 10 GHz is found using (4.15) as $C_0^F = 82.8$ fF.

The reflection coefficients calculated for the unloaded slot element as well as the capacitive loaded slot element are plotted in Fig. 4.10. It can be seen that the total transmission frequency is 15 GHz for the unloaded slot element, whereas 9.5 GHz when the slot is loaded with the capacitance. The total transmission frequencies of the slot element in both cases are almost equal to the corresponding total reflection frequencies in the complementary metal element case. In order to validate the accuracy of the MoM solution, both metal element and its complementary slot element are also solved in FEKO with and without lumped elements that are obtained from the proposed method. As can be seen from Fig. 4.11, the produced results are in agreement with the FEKO's results. This example successfully shows that the introduced method to find discrete load elements to control the total reflection band of the ring-type metal element can also be exploited for the slot element by taking the dual case into account.

In Fig. 4.12, a flowchart is generated to briefly describe the proposed method of finding discrete load values that yield desired frequency shifts for ring-type FSS elements.

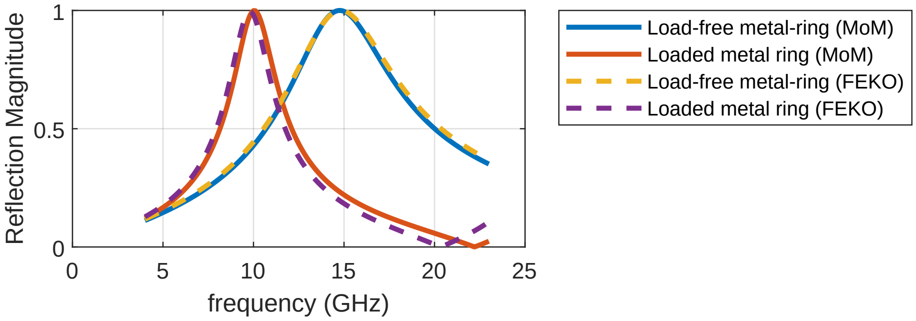

(a)

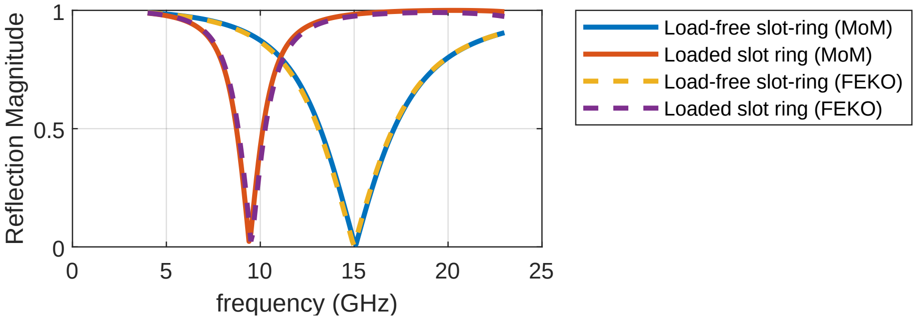

(b)

Figure 4.11: Reflection magnitude of the unloaded and loaded circular ring-type FSS elements, compared with FEKO's results. (a) Metal element. (b) Slot element.

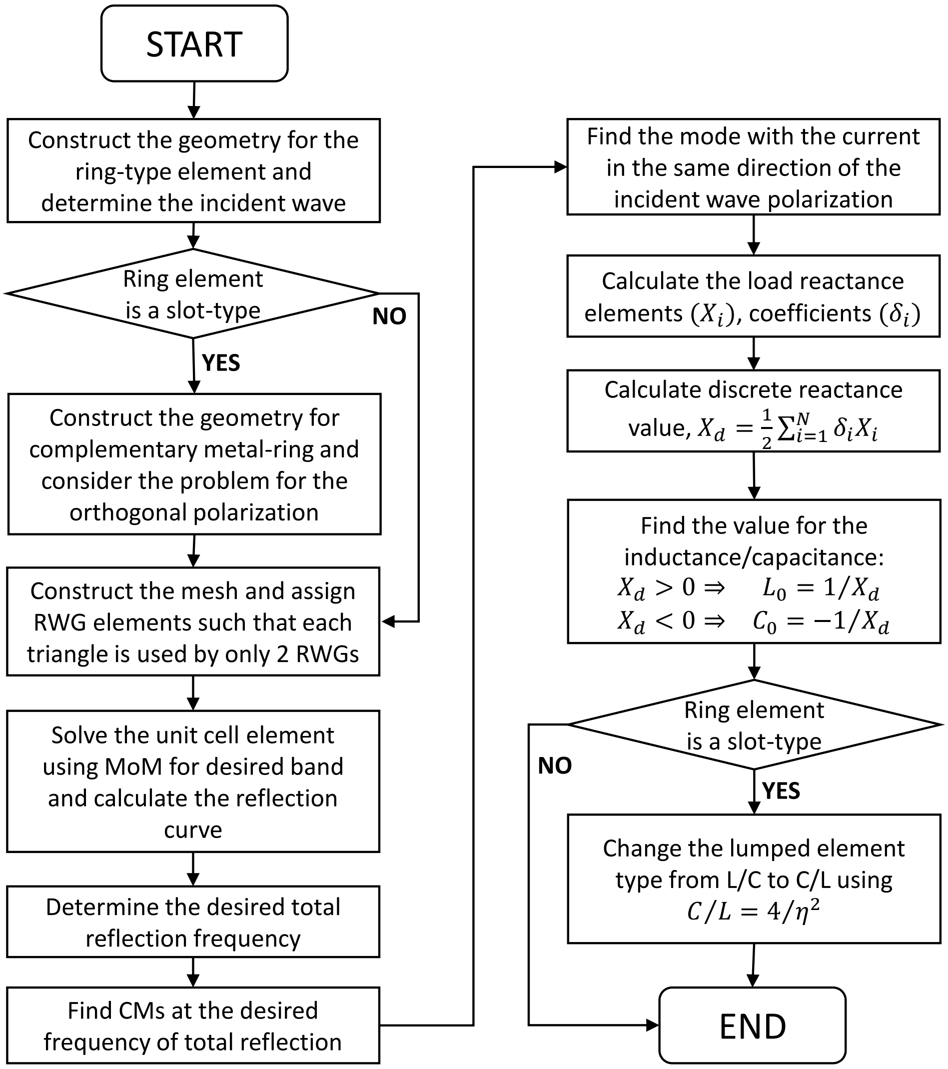

Figure 4.12: Flowchart of the proposed method.

4.3 Analyses of Various Ring-Type FSS Elements

In the previous section, the method has been demonstrated for the circular ring element, thus the discrete load values are found in advance that shifts the total reflection frequency from 14.8 to 10 GHz. However, discrete loads can also be calculated to shift the reflection band into different frequencies of interest. In this section, the analysis is performed to demonstrate the proposed method for various ring-type FSS elements considering broad band of frequencies. Hence, for each example, a wide range of inductance and capacitance values are pre-calculated in order to shift the total reflection frequency to desired frequencies. Once the load values are calculated, the accuracy of the method is also examined by the direct solution of the loaded element. The direct solution refers to the MoM solution of the loaded ring-type element where the loads that are obtained using the proposed method are applied on the element and the shifted frequency of the total reflection is calculated.

After the reactive loads are calculated for pre-determined total reflection frequencies using the proposed method, and the total reflection frequencies are calculated for pre-determined load values using the direct MoM solution, both results can be compared by plotting "total reflection frequency vs load value" response curves on the same graph. In order to find the accuracy of the proposed method relative to the direct solution, the percentage error with respect to reactive load values is also calculated to show how different the reflection frequencies that are utilized as the input for the proposed method are from the frequencies found by solving the direct solution of MoM. The relative percentage error is formulated as

$$\text{Error} = \frac{|f_0 - f_\text{m}|}{f_0} \times 100 \tag{4.16}$$

where f_0 is the value of the total reflection frequency found by the direct solution of the loaded element for predetermined loads, and f_m are the desired frequency shifts used in the developed method. Note that since the response curves obtained with the proposed method and the direct solution consist of different and unequal number of samples, the curve that is obtained from the proposed method is interpolated at the samples of the curve of the direct solution. Hence, it becomes possible to calculate the relative error of frequency with respect to different capacitive and inductive load values.

4.3.1 The Circular Element

As already been demonstrated in the previous section, the total reflection occurs at 14.8 GHz for the exemplified circular ring element when there is no applied load. To shift the total reflection frequency from 14.8 GHz to lower and higher frequencies, a wide range of inductance and capacitance values are calculated, respectively. Same to the previous example, the solution is considered for an x-polarized incident wave propagating in z direction.

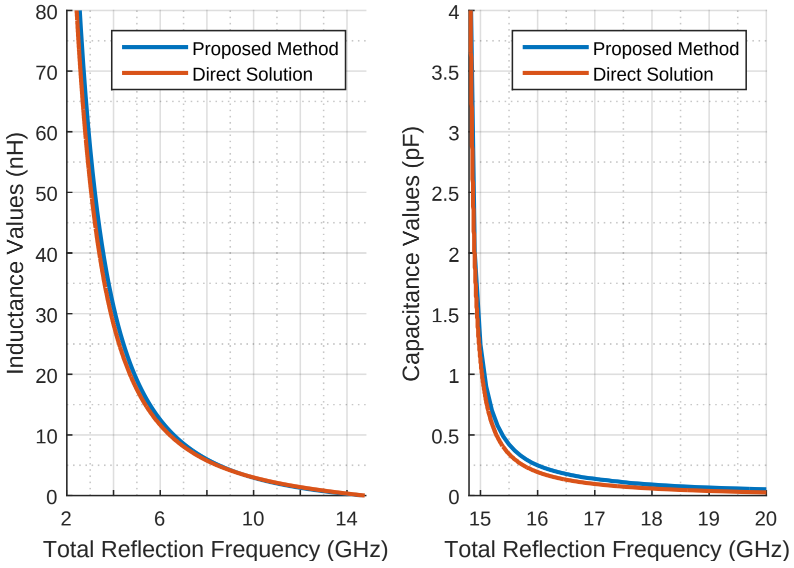

(a) (b)

Figure 4.13: The comparison of the proposed method with direct solution of the loaded element for the circular ring element. (a) Inductive values. (b) Capacitive values.

The results presented by the blue curve in Fig. 4.13 refer to the load values found by the proposed method. To calculate this response, the MoM program is initially solved for the unloaded ring element. Then the modes are tracked using the aforementioned mode tracking algorithm and subsequently load values are obtained to shift the total reflection frequency from 2 to 26 GHz. Moreover the red curve in Fig. 4.13 yields the results of the direct solution of the loaded element. In order to perform the direct solution, 1001 inductance values changing from 0 to 100 nH, as well as 1001 capacitance values from 0.1 fF to 7.5 pF are applied on the northernmost and southernmost nodes of the circular ring element. Therefore, the direct solution requires the MoM solution to be performed 2002 times. Hence, generating the red curve becomes very time-consuming compared to the generation of the blue curve which is based on the proposed method. As can be seen from the figure, the two curves are very close to each other. To have a better understanding of the accuracy, the relative error between the curves are also calculated and plotted in Fig. 4.14. According to these results, the relative error in the total reflection frequency is below 5% for inductive load values

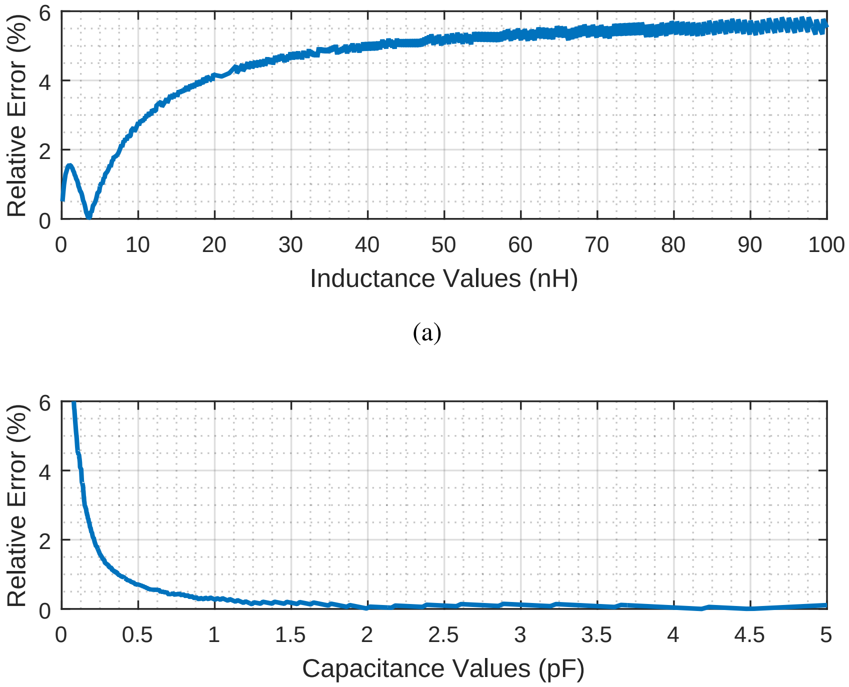

(a)

(b)

Figure 4.14: The relative error between the proposed method and the direct solution of the loaded element for the circular ring element. (a) Inductive values. (b) Capacitive values.

smaller than 43 nH and capacitive load values greater than 0.1 pF. As can be observed in Fig. 4.13, applying 43 nH and 0.1 pF corresponds to the frequencies of 3.3 GHz and 17 GHz, respectively. It means that using the proposed method, it is possible to find the load value that shifts the total reflection frequency of the circular ring element from 14.8 GHz to any frequency from 3.3 to 17 GHz with an error less than 5%.

In order to visualize the behavior of reflection within the band of interest, the amplitude of the reflection coefficient is plotted in Fig. 4.15 for different load values. 3-dB bandwidth of reflection for the circular FSS element becomes 37% when there is no applied load, whereas 8.5%, 18.5%, 33% and 27% when the element is loaded with 20 nH, 5 nH, 0.2 pF and 0.05 pF, respectively. As can be seen from the figure, the band of the FSS element becomes narrower as the reflection band shifts to the lower frequencies due to the increasing inductance value. However, even if the error of the

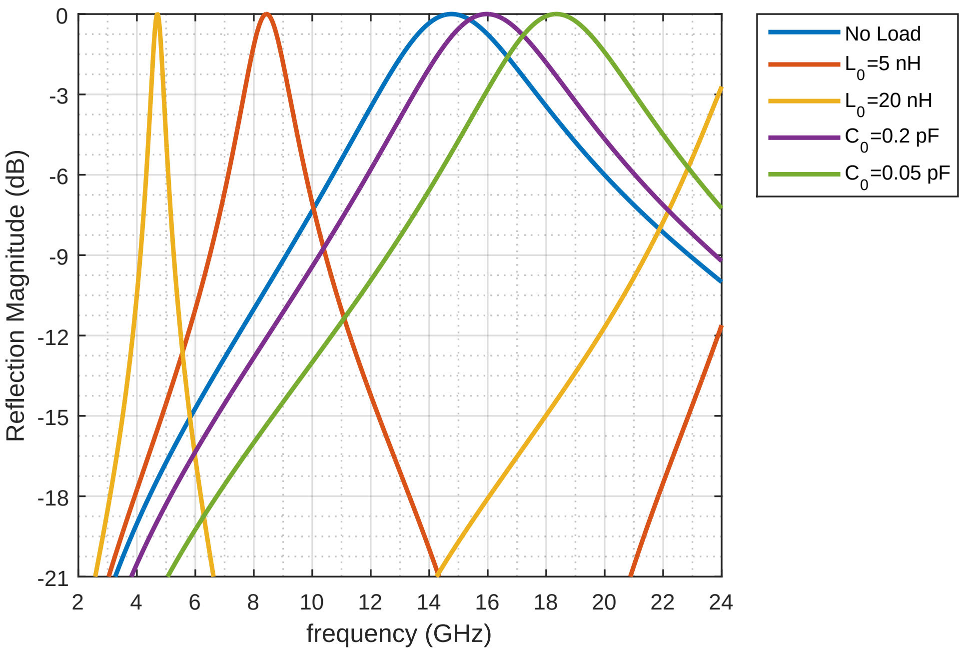

Figure 4.15: The reflection coefficient amplitude for different loading values.

proposed method also increases as the inductance increases, an error below 5% is still satisfactory. In order to observe this, the shifting of the total reflection frequency from 14.8 to 4.9 GHz can be examined. In this example, the loading value obtained from the proposed method is 20 nH in which the relative error becomes 4.1%. Due to this error, 20 nH would not shift the total reflection point from 14.8 to 4.9 GHz, but 4.7 GHz. However, even if there is no total reflection at 4.9 GHz, three quarters of the incoming power would still be reflected at this frequency. This analysis indicates that the proposed method is able to bring the reflection band of the circular ring to a value within a wide range of frequencies.

In order to complete the discussion for the circular ring element, the same element is also solved for oblique incidences. The incident wave can be defined as

$$\mathbf{E_i} = \{-\hat{\mathbf{x}}\cos\theta_i\cos\phi_i - \hat{\mathbf{y}}\cos\theta_i\sin\phi_i + \hat{\mathbf{z}}\sin\theta_i\}\, e^{jk_xx+jk_yy+jk_zz}. \tag{4.17}$$

As already discussed in the previous chapter, cut-off frequencies of the higher order modes would decrease as the incidence angle, θ_i, increases. This can cause problems in shifting the frequency band to upper frequencies since the proposed method would work only if the characteristic mode, that exhibits the same behavior as the current induced on the element surface, is being excited within the band. If the desired shift-

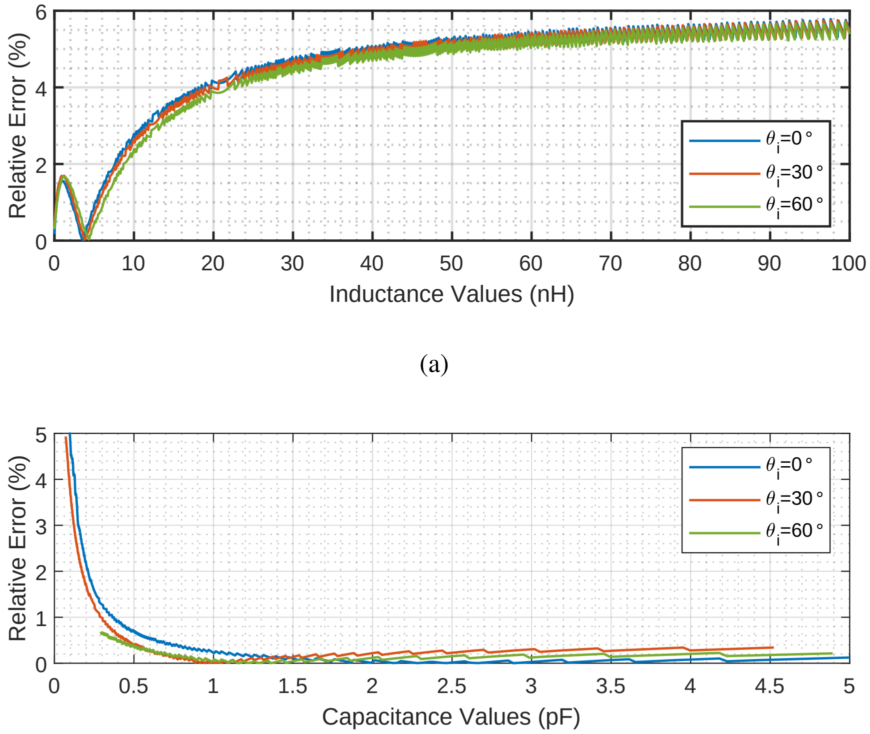

(a)

(b)

Figure 4.16: The relative error between the proposed method and the direct solution of the loaded circular ring element, illuminated by normal and oblique incidences. (a) Inductive values. (b) Capacitive values.

ing frequency is above the cut-off frequency of higher order modes, the reflection behavior would be determined by more than one mode as a combination of lower and higher order modes. In this case, the magnitude of the reflection coefficient would not be equal to the modal significance value of one of the modes. Under normal incidence, higher order modes can be excited only when the operating frequency is above 27.27 GHz. However, for oblique incidences of $\theta = 30°$ and $\theta = 60°$, the cut-off frequencies become 18.18 GHz and 14.61 GHz, respectively. Hence, the load values that are calculated with the proposed method are compared with the direct solution for the illuminations of $\theta = 0°$, $30°$ and $60°$ in order to shift total reflection frequencies from 2 to 26 GHz, from 2 to 18 GHz and from 2 to 14.5 GHz, respectively. Note that ϕ_i=0 is considered to examine the case where the electric field has a component in the x direction. As given in Fig. 4.16, the relative error values are very close to each

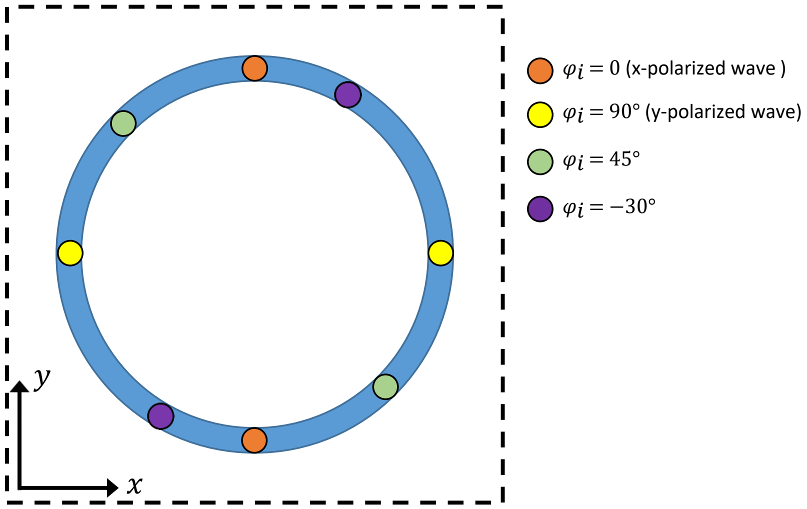

Figure 4.17: Load locations for different polarizations.

other regardless of the elevation angle. Hence, the developed method can be used effectively not only in the case of normal incidence but also for oblique incidences.

Since the geometry of the element is purely circular, the load values that are calculated with this method can be used for the incidence of any polarization. As an illustration, the locations of discrete load elements for different polarizations are depicted in Fig. 4.17. The direction of the polarization can be determined by ϕ_i for the incident wave defined in (4.17). However, in the case of non-circular ring element, the load values would become dependent on the polarization of the incident wave. In the next section, this is observed by calculating load values over square and cross-shaped ring elements.

4.3.2 The Square and Cross-Shaped Element

Due to the geometrical symmetry of square and cross-shaped elements with respect to the x and y coordinates, same loads can be used for x and y-polarized incidences. In the next example, square and cross ring FSS elements are solved for the normal incidence and polarized in the x direction as $\phi_i = 0°$ and in the diagonal direction as $\phi = 45°$. The geometry and the dimensions for both elements are given in Fig. 4.18. Both the square and the cross elements are discretized with 72 triangles.

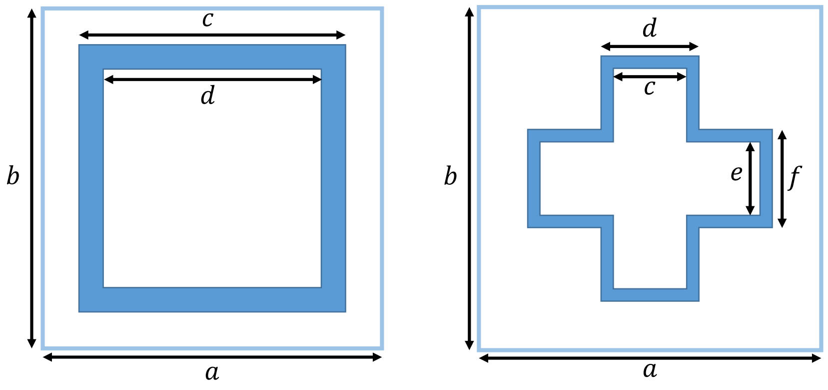

(a) (b)

Figure 4.18: Ring-type FSS elements inside the unit cell of $a = b = 14$ mm (a) Square ring element with dimensions $c = 11$ mm and $d = 9$ mm. (b) Cross ring element with dimensions $c = e = 3$ mm and $d = f = 4$ mm.

In Fig. 4.19 and 4.20, modal currents of the first 2 modes for two different polarizations are given for the square element and the cross-shaped element, respectively. Both elements are illuminated by normal incidence of $\theta_i = 0°$ at 6 GHz. In Fig. 4.19a, 4.19b, 4.20a and 4.20b, the modes are calculated for the x-polarized incidence, hence the modal currents of the first 2 modes are aligned in the x and y directions. Whereas when the elements are illuminated by a diagonal polarization of $\phi_i = 45°$, the modal currents of the first 2 modes are aligned in diagonal directions as shown in Fig. 4.19c, 4.19d, 4.20c and 4.20d. Using the proper mode that is aligned with the polarization of the illumination, reactive loads can be calculated to shift the total reflection frequency to 6 GHz.

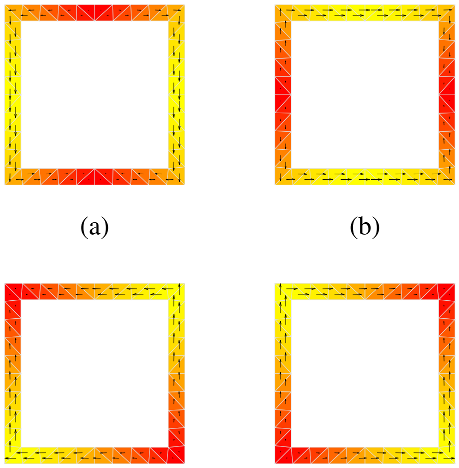

(a) (b)

(c) (d)

Figure 4.19: Modal currents of the square ring element, illuminated by (4.17) at 6 GHz. (a) Mode 1 at $\phi_i = 0°$. (b) Mode 2 at $\phi_i = 0°$. (c) Mode 1 at $\phi_i = 45°$. (d) Mode 2 at $\phi_i = 45°$.

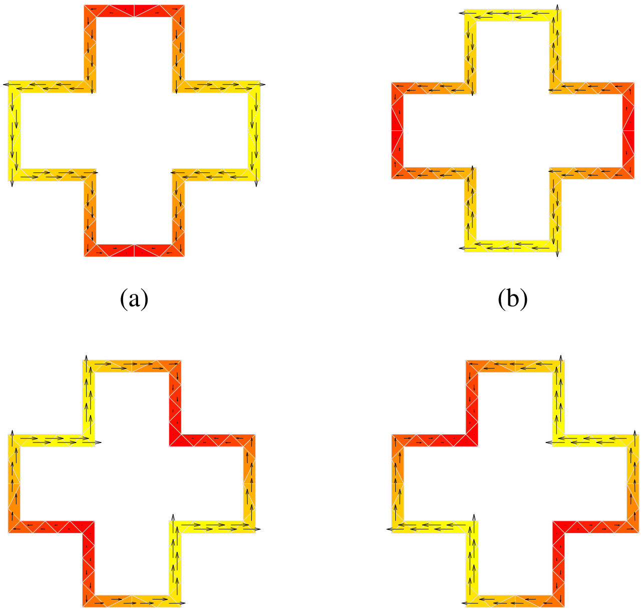

(a) (b)

(c) (d)

Figure 4.20: Modal currents of the cross ring element, illuminated by (4.17) at 6 GHz. (a) Mode 1 at $\phi_i = 0°$. (b) Mode 2 at $\phi_i = 0°$. (c) Mode 1 at $\phi_i = 45°$. (d) Mode 2 at $\phi_i = 45°$.

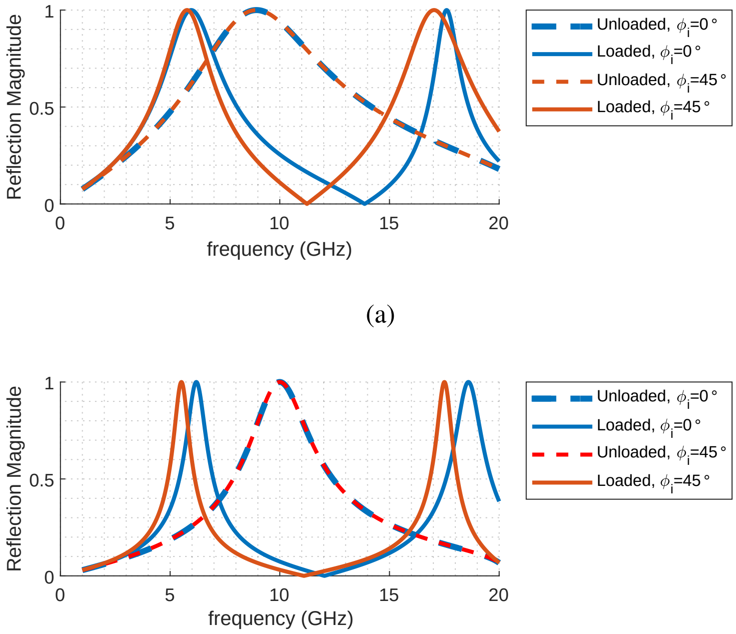

(a)

(b)

Figure 4.21: The reflection magnitude values before and after applying inductive loads that are found using the proposed method. (a) Square ring element. (b) Cross ring element.

Unlike the case of the x-polarized incidence where loads are applied on the northernmost and southernmost nodes of the element, loads must be applied on the northwestern and southeastern nodes in the case of $\phi_i = 45°$ since the magnitude of the modal current peaks at those nodes.

Following the proposed method for the square ring element, the inductance values for the desired frequency shift are calculated as $L_0 = 4.56$ nH and $L_0 = 4.39$ nH for $\phi_i = 0°$ and $\phi_i = 45°$, respectively. Similarly, the inductance values that must be applied on the cross ring element are found as $L_0 = 6.22$ nH and $L_0 = 8.29$ nH for $\phi_i = 0$ and $\phi_i = 45°$, respectively. The amplitude of the reflection coefficient before and after loading the elements are plotted in Fig. 4.21. In these results, the total reflection frequency for the square ring element is shifted from 8.93 to 5.96 GHz for $\phi_i = 0°$ and from 8.93 to 5.77 GHz for $\phi_i = 45°$. Similarly, the total reflection frequency for the cross ring element is shifted from 10 to 6.19 GHz for $\phi_i = 0°$ and from 10 to 5.51 GHz for $\phi_i = 45^\circ$. Although the results in the case of x polarization are relatively more accurate, the desired frequency shift can also be obtained in the case of $\phi_i = 45^\circ$ with reasonable accuracy.

Besides that, total reflections also occur at higher frequencies when inductive loads are applied on the both elements. As can be seen from Fig. 4.21a, total reflections from the square ring element occurs at 17.6 and 17 GHz for $\phi_i = 0^\circ$ and $\phi_i = 45^\circ$, respectively. In Fig. 4.21b, total reflections from the cross ring element take place at 18.6 and 17.5 GHz for $\phi_i = 0^\circ$ and $\phi_i = 45^\circ$, respectively. This behavior can be explained due to the resonance of a 3rd mode at these frequencies. The currents associated with this higher order mode are illustrated in Fig. 4.22 for all cases.

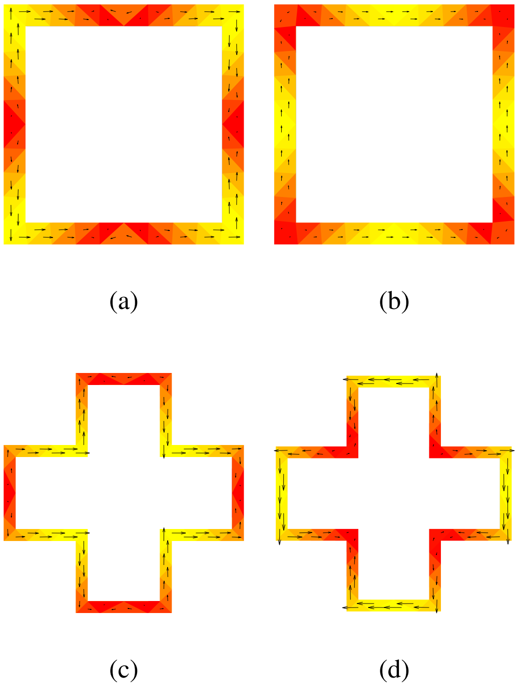

(a) (b)

(c) (d)

Figure 4.22: Modal current of the 3rd mode at higher frequencies. (a) Current on the square ring element at 17.6 GHz for $\phi_i = 0^\circ$. (b) Current on the square ring element at 17 GHz for $\phi_i = 45^\circ$. (c) Current on the cross ring element at 18.6 GHz for $\phi_i = 0^\circ$. (d) Current on the cross ring element at 17.5 GHz for $\phi_i = 45^\circ$.

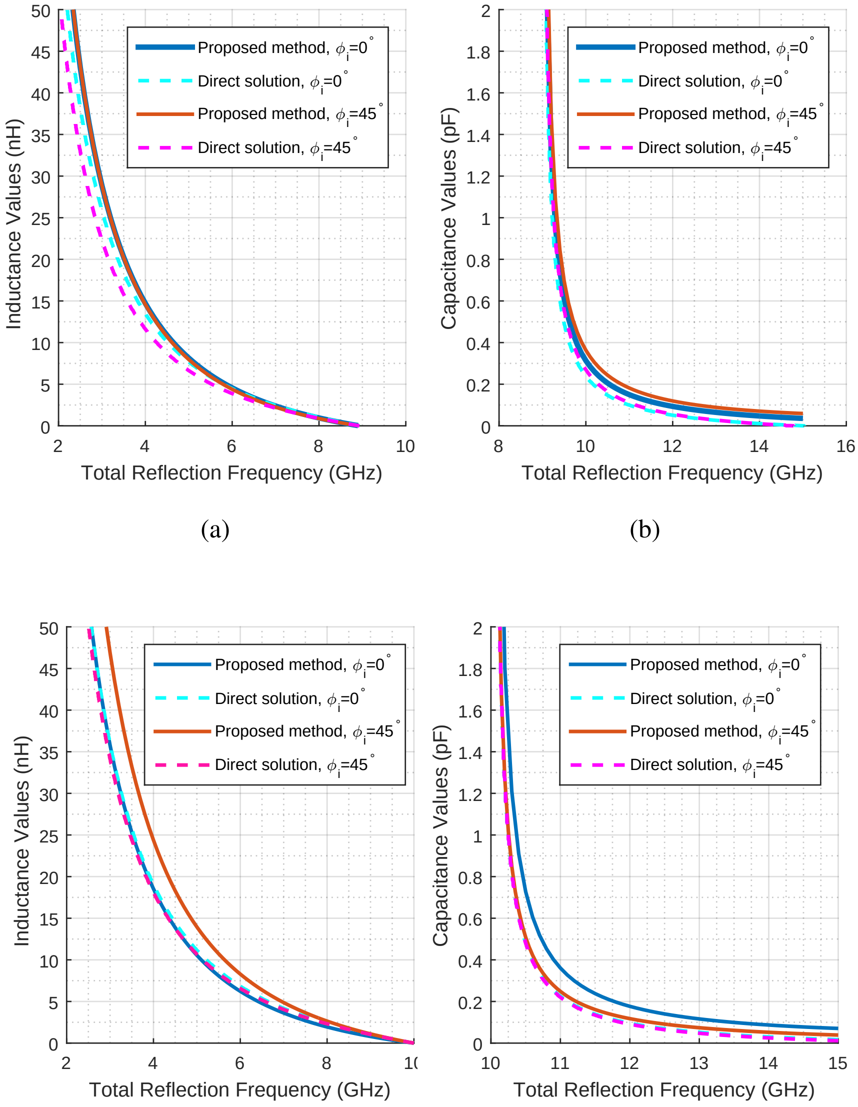

(a) (b)

(c) (d)

Figure 4.23: The comparison of the proposed method with direct solution. (a) Inductive loaded square ring element. (b) Capacitive loaded square ring element. (c) Inductive loaded cross ring element. (d) Capacitive loaded cross ring element.

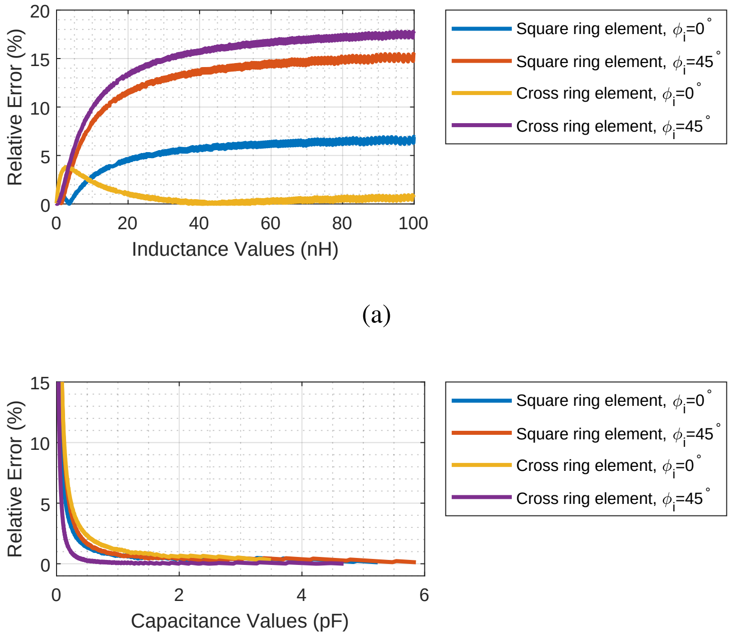

(a)

(b)

Figure 4.24: The relative error between the proposed method and the direct solution of the loaded element for the square and cross-shaped ring elements. (a) Inductive values. (b) Capacitive values.

In order to check the accuracy of the solutions over a wide band of frequencies, the proposed method is compared with the direct MoM solution for 1001 inductance values from 0 nH to 100 nH and 1001 capacitance values from 0.1 fF to 7.5 pF. In Fig. 4.23, the calculated load values are given with respect to the total reflection frequency for square and cross-shaped ring elements. To have a better insight about the accuracy of the solution, the relative error is given in Fig. 4.24 for both elements and polarizations. It can be deduced from these results that the proposed method is more accurate across the band of interest when the element is illuminated by an x-polarized plane wave. In the case of the square-element illuminated by an x-polarized incidence, the error is 5% when load values are 5.2 nH and 0.15 pF. It means that assuming less than 5% error is tolerable, total reflection frequency can be shifted from 8.93 GHz to a range of frequencies from 2.9 to 10.5 GHz. In a similar fashion, the range of the frequency shift for the cross-shaped element becomes 1.8 to 11 GHz in the case of x-polarized incidence. On the other hand, when the elements are illuminated by a

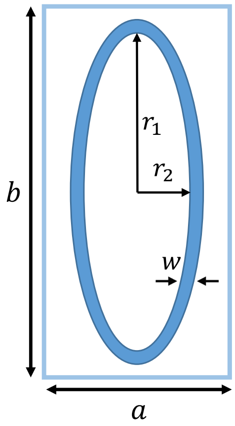

Figure 4.25: Elliptic ring-type FSS element with the dimensions $r_1 = 6$ mm, $r_2 = 2$ mm and $w = 0.5$ mm inside the rectangular unit cell of $a = 7$ mm and $b = 14$ mm.

diagonal polarization, the band of shift with an error less than 5% are from 5.4 GHz to 10.3 GHz and from 6.8 to 12.2 GHz, for square and cross-shaped ring elements, respectively. These results indicate that although the ring-type unit cell element is not circular and is not illuminated particularly by x and y-polarized plane waves, the proposed method can still be applied to find the desired load values accurately in a wide range of frequencies.

4.3.3 The Elliptic Element in Rectangular Unit Cell

In the previous examples, the unit cell elements are chosen to be same when viewed from the x and y direction. However, in this section, an elliptic ring element is examined inside a rectangular unit cell to see the validity of the proposed method. The dimensions of the elliptic ring element is given in Fig. 4.25. The element is discretized with 76 triangles, hence 76 RWG functions are defined to solve this problem. Both x and y-polarized normal incidence are considered in this example. Since the element is unsymmetrical with respect to the x and y coordinates, the corresponding modes are no longer degenerate modes, hence they would resonate at different frequencies. The modal significance values for the first 2 characteristic modes are plotted in Fig. 4.26. The 1st mode is excited when the element is illuminated by a y-polarized electric field, and similarly the 2nd mode is excited due to the x-polarized

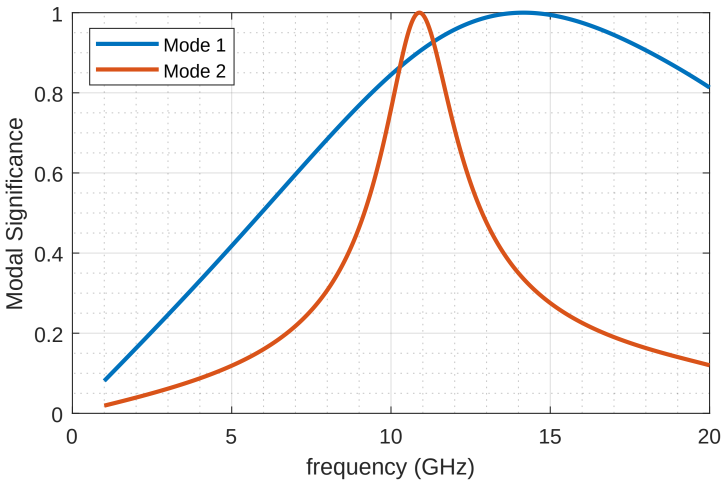

Figure 4.26: Modal significance values of the first 2 modes, illuminated by x and y-polarized plane waves.

electric field. This can be seen by observing modal currents in Fig. 4.27, where the modal surface current for the first two modes are depicted at 8 GHz. Therefore, the reflection coefficient of the FSS element follows either the 1st or the 2nd characteristic mode depending on the polarization of the incidence. Hence, in the case of y polarization, the full reflection occurs at 14.15 GHz, whereas in the case of x polarization, the full reflection happens at 10.9 GHz with relatively narrower reflection band.

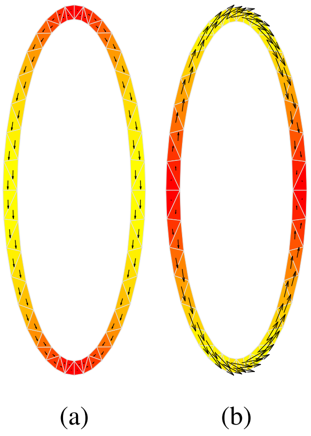
(a) (b)

Figure 4.27: Modal currents on the elliptic ring element, illuminated by an x-polarized plane wave at 8 GHz. (a) Mode 1. (b) Mode 2.

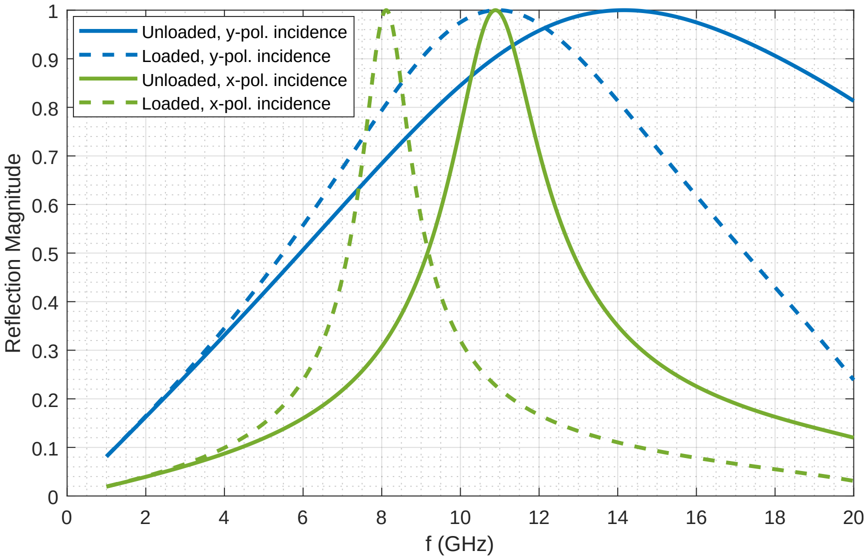

Figure 4.28: The reflection magnitude values before and after loading the elliptic ring element for the two orthogonal polarizations.

In order to demonstrate the developed method, the required load values are calculated to shift the total reflection frequency to 8 and 11 GHz in the case of x and y polarizations, respectively. Using the 1st mode, the inductance value to shift the total reflection frequency from 14.15 to 11 GHz is found as 1.8 nH. It must be applied on the easternmost and westernmost nodes of the element. Similarly with the help of the 2nd mode, the inductance value to shift the total reflection frequency from 10.9 to 8 GHz becomes 2.9 nH, which must be applied on the northernmost and southernmost nodes of the element. After loading the reactive elements accordingly, total reflection frequency is shifted from 14.15 to 11 GHz for the x-polarized plane wave and from 10.9 GHz to 8.1 GHz for the y-polarized plane wave. The curves associated with these results can be seen in Fig. 4.28. The load that is applied for one of the polarizations will not affect the reflecting behavior under the excitation of the other polarization as long as the polarization directions are orthogonal to each other. This is because the node where the load is placed for one polarization is the null region for its orthogonal polarization. Therefore, loads for both x and y-polarized incidence can be applied at the same time to change the reflection response in both directions.

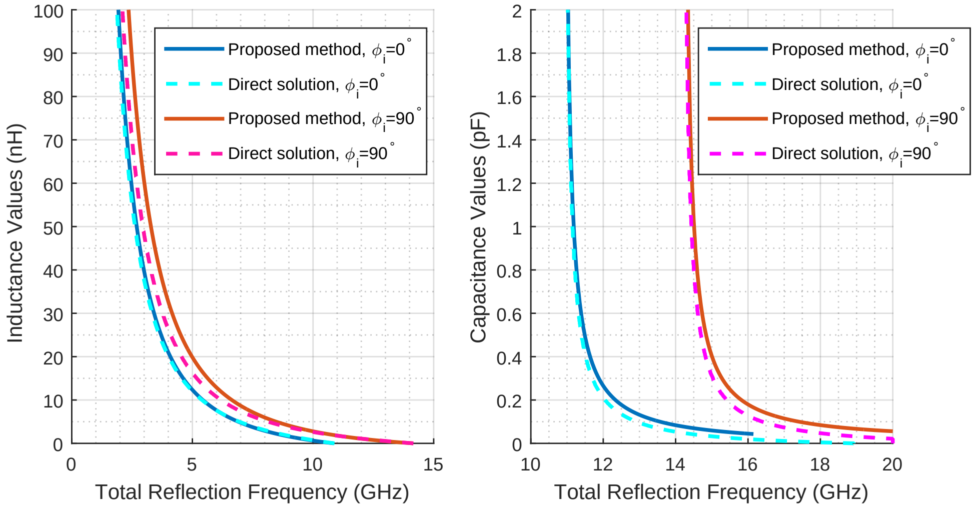

(a) (b)

Figure 4.29: The comparison of the proposed method with the direct solution for the elliptic ring element. (a) Inductive values. (b) Capacitive values.

The accuracy of the method for the elliptic ring element is also evaluated by comparing load values of the proposed method with direct MoM solution of 1001 inductance values changing from 0 to 100 nH, as well as 1001 capacitance values from 0.1 fF to 7.5 pF applied on the element. In Fig. 4.29, the load values that are calculated by the proposed method are given with respect to the shifted total reflection frequency along with the direct solution of the frequency shifts with respect to the load values. The corresponding relative error for both x and y-polarized illumination is also given in Fig. 4.30. The error is 5% for the x-polarized incidence when load values are 100 nH and 0.1 pF. It means that by assuming less than 5% error is sufficient, total reflection frequency can be shifted from 10.9 GHz to a range of frequencies from 1.8 to 12.9 GHz. Similarly in the case of y polarization, the error is 5% when the load values are 6 nH and 0.12 pF, thus the total reflection frequency can be shifted from 14.15 GHz to a range of frequencies from 7.6 to 16.1 GHz with an error less than 5%. This solution indicates that the developed method can also be utilized to change the reflection properties of ring-type elements that are not symmetrical with respect to x and y coordinates. In fact asymmetric nature of the unit cell element would give the opportunity of having different radiation characteristics for different incidences.

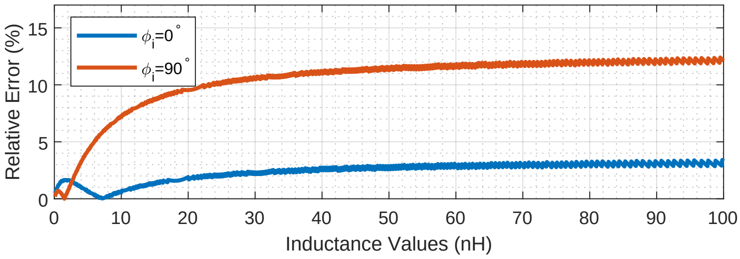

(a)

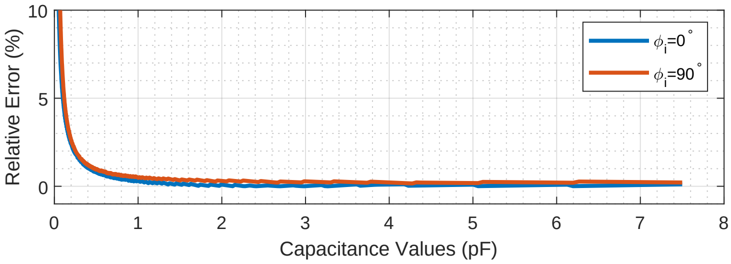

(b)

Figure 4.30: The relative error between the proposed method and the direct solution of the loaded element for the elliptic ring elements. (a) Inductive values. (b) Capacitive values.

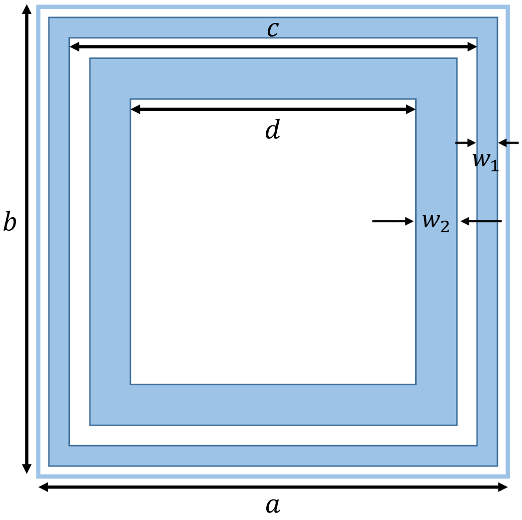

Figure 4.31: FSS element that consists of two concentric square rings with the dimensions $c = 40$ mm, $d = 28$ mm, $w_1 = 2$ mm and $w_2 = 4$ mm inside square unit cell of $a = b = 45$ mm.

4.3.4 The Element of Concentric Square Rings

After going through examples to demonstrate the proposed method for single ring elements, the next step would be to apply the proposed method to dual band FSS elements that consist of two rings inside the unit cell. In Fig. 4.31, the dimensions for an FSS element that consists of two concentric square rings are given. As discussed in [95], it is a dual-band FSS element such that the inner slot determines the higher reflection band and the outer slot determines the lower band. Under the x-polarized normal incidence, the reflection amplitude and modal significance values for the first 4 modes of the FSS element of concentric square rings are given in Fig. 4.32. As can be seen from the figure, 4 modes are excited up to 6 GHz. 1st and 2nd modes are degenerate modes that resonate around 1.4 GHz due to the outer ring element. 3rd

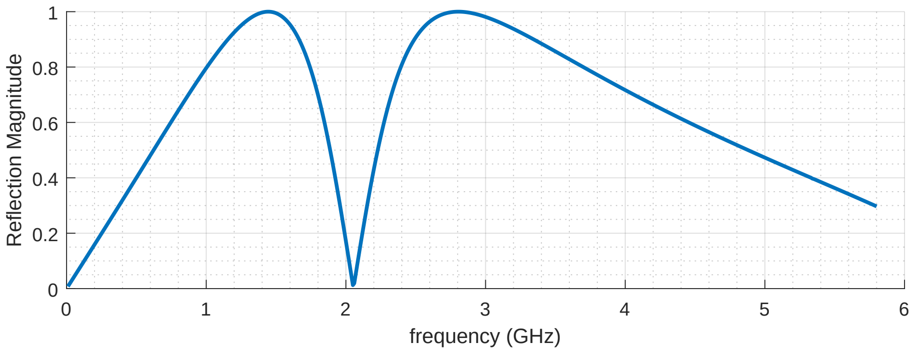

(a)

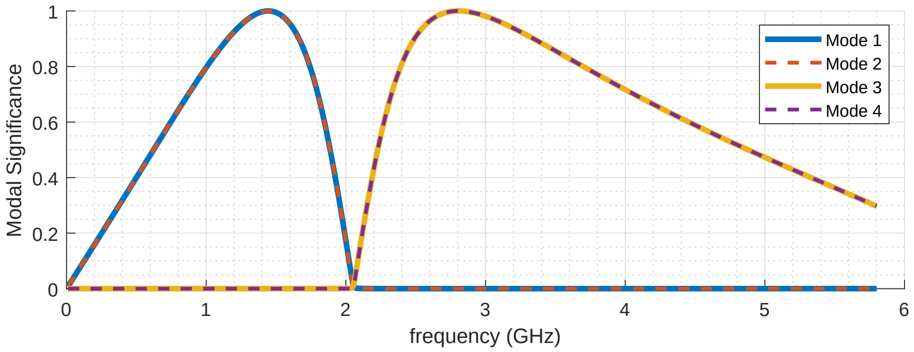

(b)

Figure 4.32: FSS element of two concentric square rings, illuminated by normal incidence in square unit cell. (a) Reflection magnitude. (b) Modal significance values.

and 4th are also degenerate modes but resonate around 2.8 GHz due to the inner ring element. As a result, the reflection coefficient is determined by the sum of one of the 1st and 2nd modes and one of the 3rd and 4th modes. In order to check which modes correspond to which polarization, the modal currents over the ring elements can be examined.

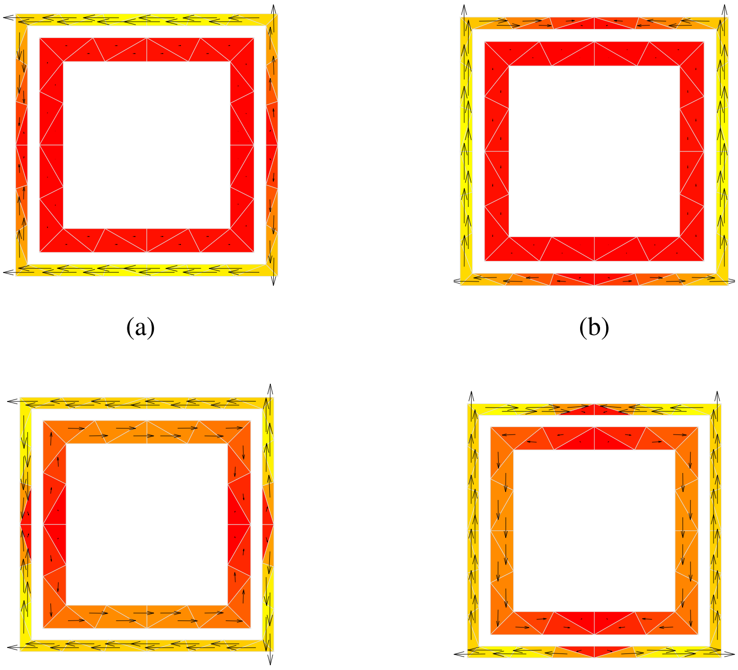

(a) (b)

(c) (d)

Figure 4.33: Modal currents on the FSS element of two concentric square rings, illuminated by normal incidence at 1.4 GHz. (a) Mode 1. (b) Mode 2. (c) Mode 3. (d) Mode 4.

In Fig. 4.33, modal currents of the first 4 modes are depicted at 1.4 GHz. By observing the current of only the outer ring element, 1st and 2nd modes correspond to the x and y polarizations, respectively. Since the 3rd and the 4th modes are not excited at this frequency, the current over the 3rd and 4th modes resemble to a high-order mode behavior. Besides that, because the inner ring is expected to resonate only at the upper band, modal currents on the inner ring are barely induced at this frequency. However, as modal currents at 2.8 GHz can also be seen from Fig. 4.34, the induced current over the inner ring element of the 3rd and 4th modes correspond to the x and y polar-

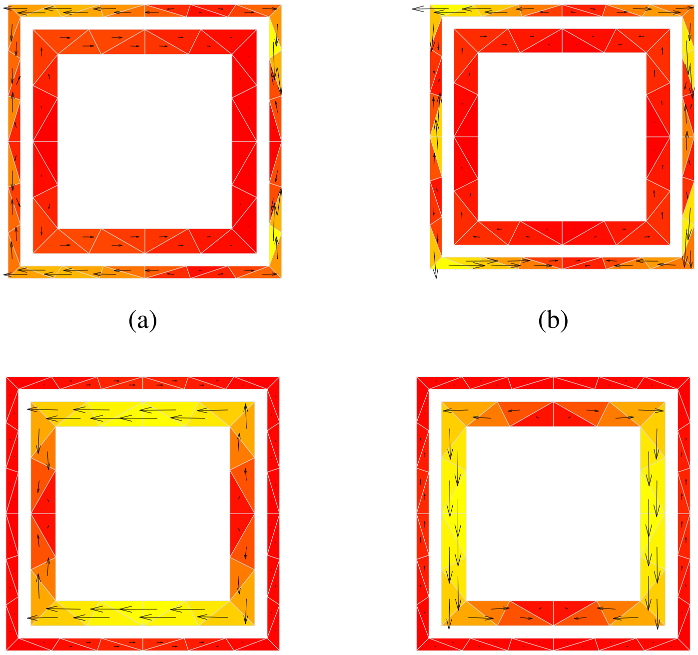

(a) (b) (c) (d)

Figure 4.34: Modal currents on the FSS element of two concentric square rings, illuminated by normal incidence at 2.8 GHz. (a) Mode 1. (b) Mode 2. (c) Mode 3. (d) Mode 4.

izations, respectively. This time modal currents are not induced by either polarization over the outer ring. Since the given example is considered for the x-polarized normal incidence, only 1st and 3rd modes are excited. The 1st mode shapes the reflection behavior of the unit cell element at frequencies below 2 GHz, whereas the 3rd mode affects the reflection behavior from 2 to 6 GHz.

The total reflection frequencies of the isolated ring elements are very close to the total reflection frequencies when both elements are solved concentrically in the same unit cell. When both rings are solved together in the same unit cell, total reflections occur at 1.44 and 2.81 GHz. However total reflections occur at slightly different frequencies when rings are solved separately, which are 1.47 and 2.82 GHz for outer and inner rings, respectively. Therefore, load values are calculated for each ring using the proposed method in order to shift the total reflection frequencies to desired frequencies. The method is demonstrated through four separate examples as described in Table 4.2. In order to modify the reflection band of the unit cell element according to this

Table 4.2: Desired frequency shifts for the dual-band FSS element of two concentric rings.

Case	Desired Shift in the Lower Band	Desired Shift in the Upper Band
I	1.44 GHz → 1.0 GHz	2.81 GHz → 2.3 GHz
II	1.44 GHz → 1.7 GHz	2.81 GHz → 3.2 GHz
III	1.44 GHz → 1.0 GHz	2.81 GHz → 3.2 GHz
IV	1.44 GHz → 1.7 GHz	2.81 GHz → 2.3 GHz

table, the proposed method is applied over both inner and outer rings separately, for the x-polarized normal incidence. After utilizing the method, the load values that shift the total reflection frequencies of the isolated inner ring from 2.82 GHz to 2.3 and 3.2 GHz are found as $L_{\text{inner}} = 5$ nH and $C_{\text{inner}} = 1.03$ pF, respectively. Applying these loads over the northernmost and southernmost nodes of the isolated inner ring element, the change of the reflection magnitude is plotted in Fig. 4.35. From these results, the total reflection frequency is shifted from 2.82 GHz to 2.37 and 3.1 GHz in

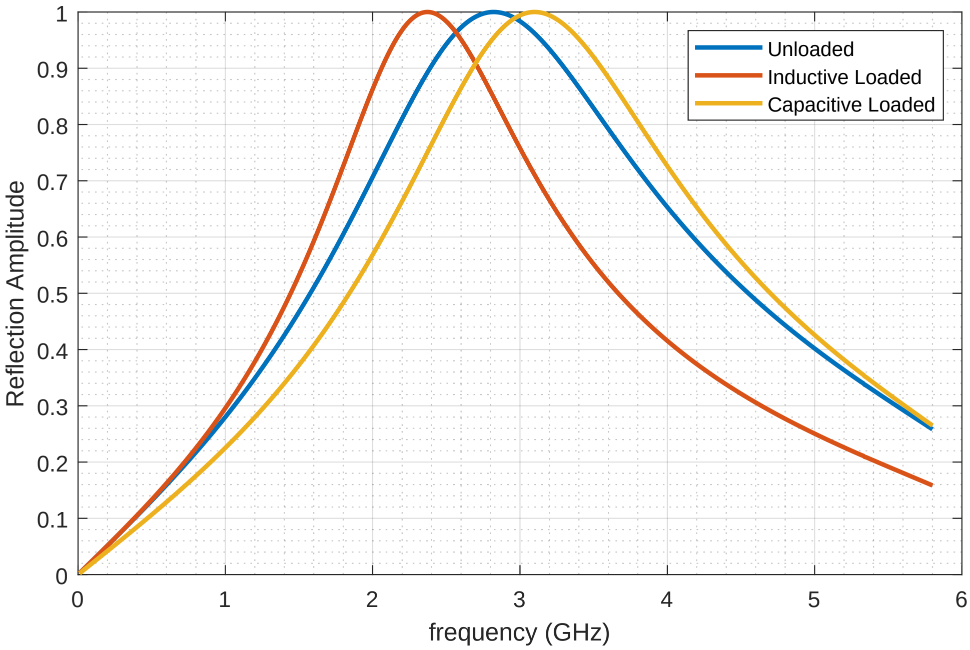

Figure 4.35: The reflection magnitude of the isolated inner ring element, unloaded and loaded with $L_{\text{inner}} = 5$ nH and $C_{\text{inner}} = 1.03$ pF.

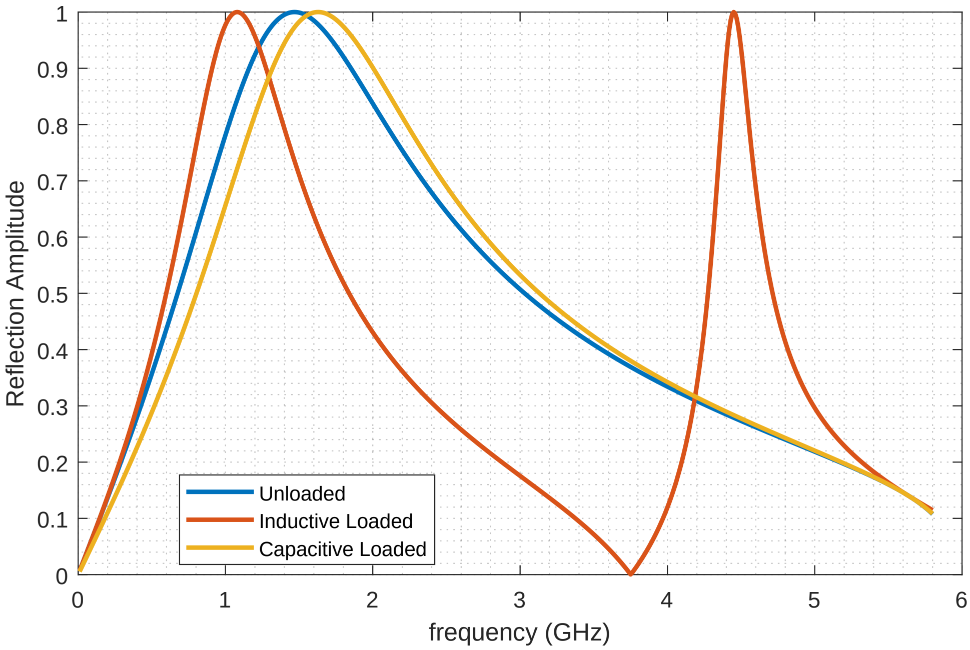

Figure 4.36: The reflection magnitude of the isolated outer ring element, unloaded and loaded with $L_{\text{outer}} = 25.7$ nH and $C_{\text{outer}} = 1.47$ pF.

the case of an inductive and a capacitive loading, respectively. Similarly, the load values that shift the total reflection frequencies of the isolated outer ring from 1.47 GHz to 1 and 1.7 GHz are found as $L_{\text{outer}} = 25.7$ nH and $C_{\text{outer}} = 1.47$ pF, respectively. Applying these loads over the northernmost and southernmost nodes of the isolated outer ring in the unit cell, the change of the reflection magnitude is also plotted in Fig. 4.36. As shown in this figure, total reflection frequency is shifted from 1.47 to 1.63 GHz in the case of the capacitive loading. Whereas in the case of the inductive loading, total reflection frequency is shifted from 1.47 to 1.08 GHz. Besides that, total reflection also occurs at 4.45 GHz due to a 3rd mode resonates at this frequency. The modal current for this higher order mode is also depicted in Fig. 4.37. Note that the resonances that cause other total reflections which are expected in this example are due to the 1st modes with modal currents flowing in the x direction. They are not also plotted for the sake of brevity. Having successfully shifted the reflection band of the isolated ring elements to desired frequencies, the next step is to apply these loads to the FSS element of two concentric rings.

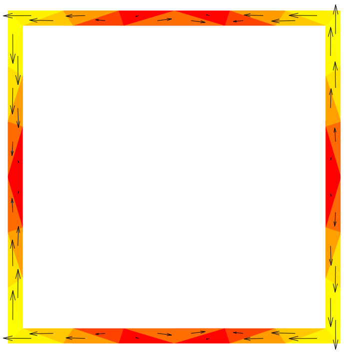

Figure 4.37: The current of the 3rd mode at 4.45 GHz due to the inductive loading of $L_{\text{outer}} = 25.7$ nH on the isolated outer ring element.

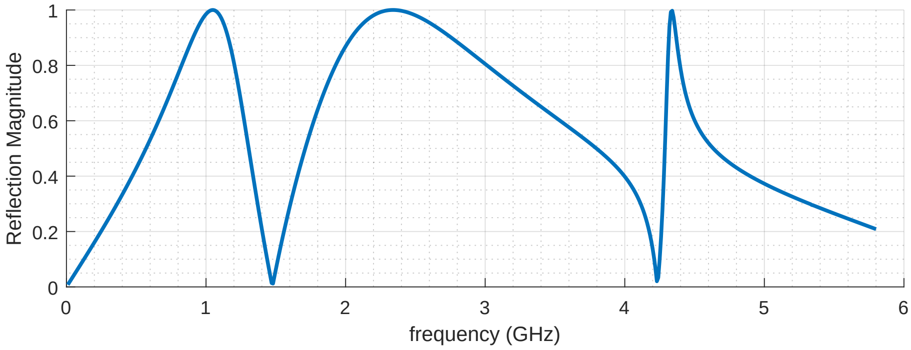

(a)

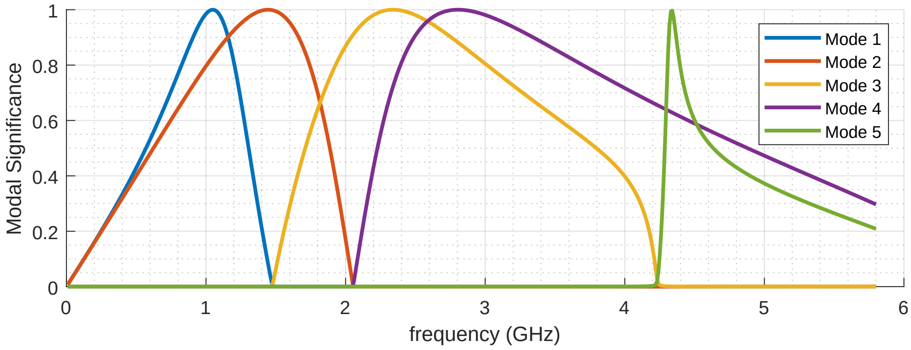

(b)

Figure 4.38: The solution of the FSS element, illuminated by an x-polarized plane wave, when inner and outer rings are loaded by $L_{\text{inner}} = 5$ nH and $L_{\text{outer}} = 25.7$ nH, respectively. (a) The reflection magnitude. (b) The modal significance values.

In the first example, 1st, 3rd and 5th modes can be excited due to the x-polarized incidence, which can be observed by comparing the characteristic modes and the resulting reflection coefficient from Fig. 4.38a and Fig. 4.38b. Due to the inductive loads applied on the outer ring, the resonance frequency of the 1st mode is shifted from 1.44 to 1.05 GHz. Similarly due to the inductive loads applied on the inner ring, the resonance frequency of the 3rd mode is shifted from 2.81 to 2.34 GHz. Hence, the total reflection frequencies of the unit cell element become 1.05 and 2.34 GHz, which is very close to the desired shifting goal of 1 and 2.3 GHz. Besides, a 5th mode is also excited due to the inductive load on the outer ring. It corresponds to the higher order mode depicted in Fig. 4.37 and causes total reflection at 4.34 GHz.

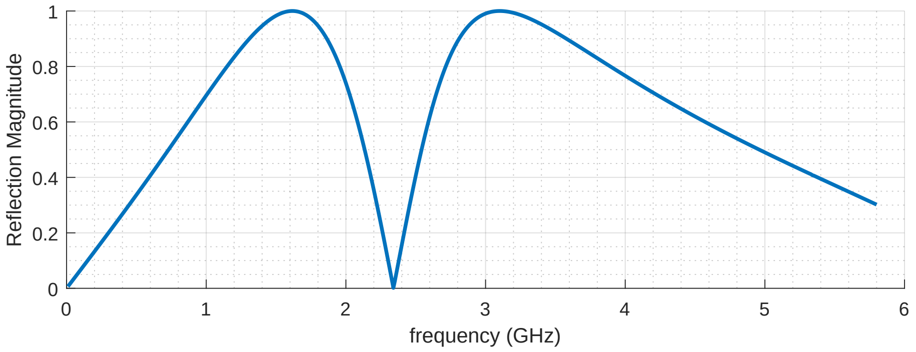

(a)

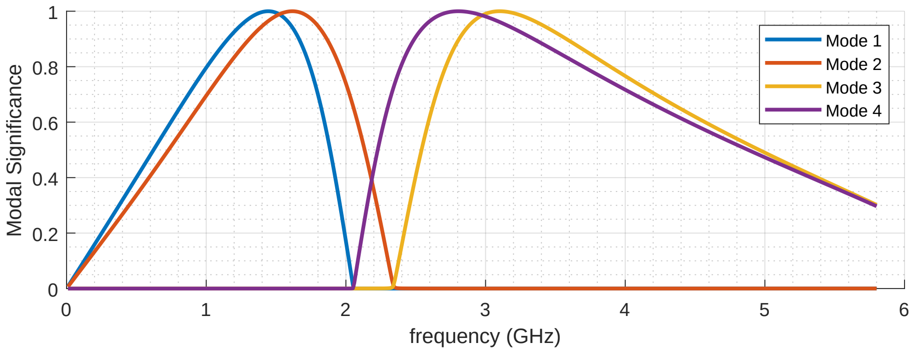

(b)

Figure 4.39: The solution of the FSS element, illuminated by an x-polarized plane wave, when inner and outer rings are loaded by $C_{\text{inner}} = 1.03$ pF and $C_{\text{outer}} = 1.47$ pF, respectively. (a) The reflection magnitude. (b) The modal significance values.

The outcome of the second example is given in Fig. 4.39 where both rings are loaded with capacitive loads. In this case, only the 2nd and 3rd modes are excited due to the x-polarized incidence in which the resonance frequency of the 2nd mode is shifted from 1.44 to 1.62 GHz due to capacitive load on the outer ring, and the resonance frequency of the 3rd mode is shifted from 2.81 to 3.1 GHz due to the capacitive load on the inner ring. As a result, the total reflection frequencies become 1.62 and 3.1 GHz, which are also close to the desired goals of 1.7 and 3.2 GHz.

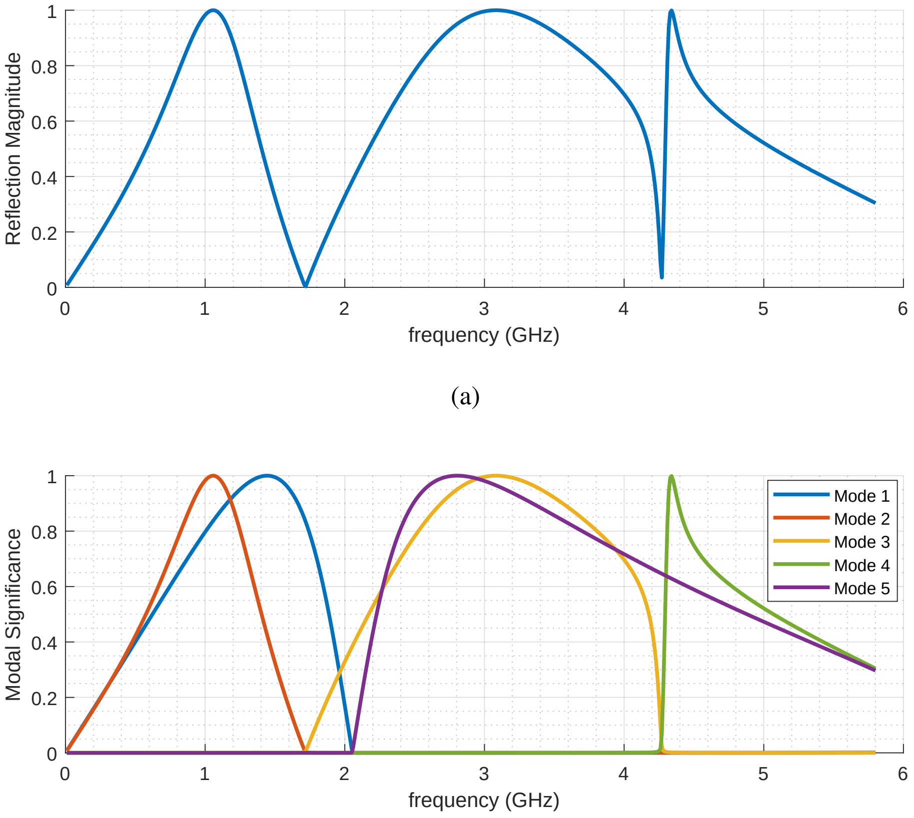

(a)

(b)

Figure 4.40: The solution of the FSS element, illuminated by an x-polarized plane wave, when inner and outer rings are loaded by $C_{\text{inner}} = 1.03$ pF and $L_{\text{outer}} = 25.7$ nH, respectively. (a) The reflection magnitude. (b) The modal significance values.

In Fig. 4.40, the results of the third example are demonstrated where an inductive load is applied on the outer ring and a capacitive load is applied on the inner ring. Hence, 2nd, 3rd and 4th modes are excited due to the x-polarized incidence, where the 2nd mode is shifted from 1.44 to 1.06 GHz due to the inductive load on the outer ring, and the resonance frequency of the 3rd mode is shifted from 2.81 to 3.08 GHz due to the capacitive load on the inner ring. Therefore, the total reflection frequencies become 1.44 and 3.08 GHz, which are also very close to the initial goals. Again, 4th mode is also excited due to the inductive loading of the outer ring as depicted in Fig. 4.37. It also causes total reflection around 4.3 GHz.

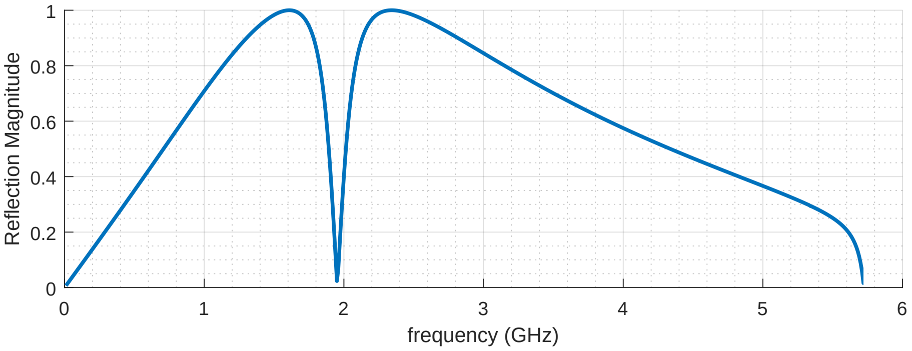

(a)

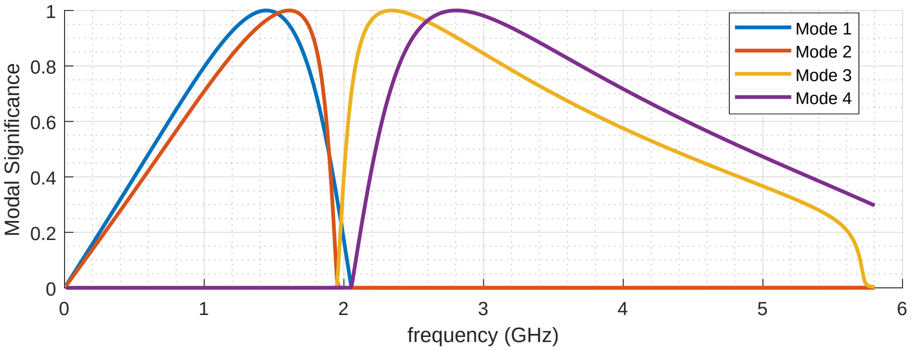

(b)

Figure 4.41: The solution of the FSS element, illuminated by an x-polarized plane wave, when inner and outer rings are loaded by $L_{\text{inner}} = 5$ nH and $C_{\text{outer}} = 1.47$ pF, respectively. (a) The reflection magnitude. (b) The modal significance values.

The last example is relatively harder to achieve since the upper and lower bands are intended to be made closer by loading the outer ring with a capacitive load and the inner ring with an inductive load. As shown in Fig. 4.41, 2nd and 3rd modes are excited due to the x-polarized incidence. Therefore, the 2nd mode is shifted from 1.44 to 1.61 GHz due to the capacitive load on the outer ring, and the resonance frequency of the 3rd mode is shifted from 2.81 to 2.34 GHz due to the inductive load on the inner ring. As expected, total reflection frequencies of the unit cell are shifted to 1.61 GHz and 2.34 GHz, which are again very close to the initially intended frequencies.

Overall, the results of these four different examples indicate that it is also possible to find load values in advance to shift the reflection of the dual-band FSS element to desired frequencies. In order to complete this discussion, the method is also performed over ring elements that are placed in different layers. Therefore in the last section of this chapter, the proposed method is examined for two metal rings as well as one metal ring and one slot ring located at two different layers.

4.3.5 The Multilayer Square Elements

In order to demonstrate the analysis of multilayer element, two square rings depicted in Fig. 4.31 are utilized again in the square unit cell of $a = b = 45$ mm under the

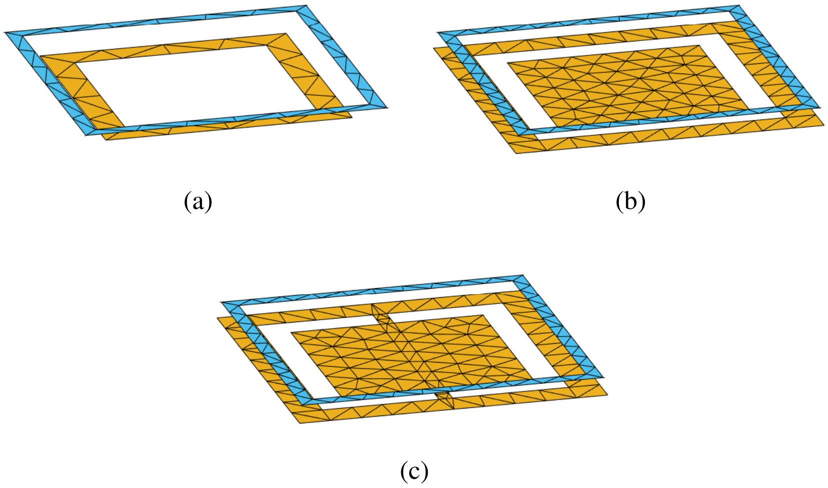
(a)

(b)

(c)

Figure 4.42: Discretization of the two-layer ring-type FSS element. (a) Ring-type metal elements on both layers. (b) Ring-type metal element on the top layer, and ring-type slot element on the bottom layer for the unloaded solution. (c) Ring-type metal element on the top layer, and ring-type slot element on the bottom layer for the loaded case.

x-polarized plane wave. However this time, the inner ring is placed 2.5 mm below the outer ring, hence the structure becomes a 2-layer FSS element. As can be recalled from 4.2.2, once the value of the reactive load is obtained for the metal ring element, the load values for the complementary slot element can be easily calculated through (4.15a) and (4.15b). Therefore, the problem can also be realized as ring-type slot elements on either layers. In this final section of this chapter, the elements on both layers are initially considered as metal rings. Then the ring-type metal element on the bottom layer is turned into its complementary slot. The triangulated forms of the elements for both problems are depicted in Fig. 4.42a and 4.42b. The mesh structure for the loaded slot element is also given in Fig. 4.42c, since the extra mesh on the slot region is needed to define the loading.

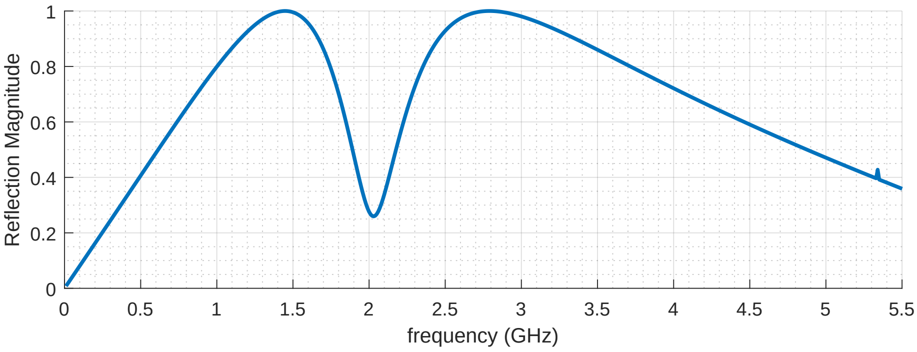

(a)

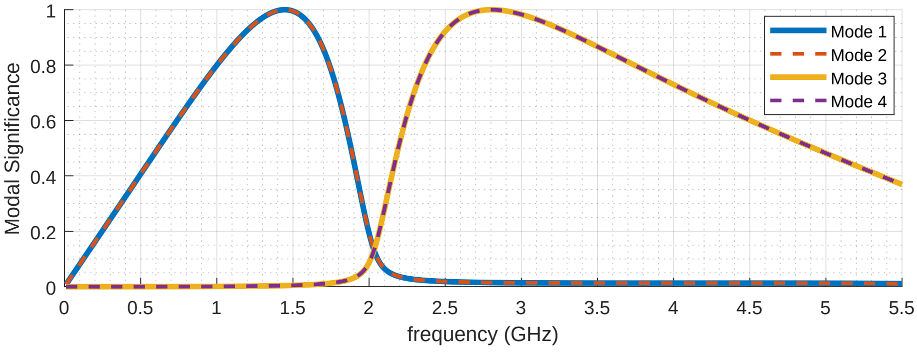

(b)

Figure 4.43: 2-layer FSS element that consists of unloaded metal ring elements on the both layers, illuminated by an x-polarized plane wave. (a) The reflection magnitude. (b) The modal significance values.

In Fig. 4.43a and 4.43b, the resulting reflection magnitude and the modal significance values of the first 4 modes are given, respectively, when the FSS element consists of ring-type unloaded metal elements on both layers. Since the larger ring on the top layer excites one of the 1st and 2nd modes, and similarly the smaller ring on the bottom layer excites one of the 3rd and 4th modes, the reflection behavior of the 2-layer element becomes very similar to the example of two concentric rings given in Fig. 4.32. Thus the total reflection frequencies become 1.44 and 2.81 GHz, similar to the example of two concentric rings.

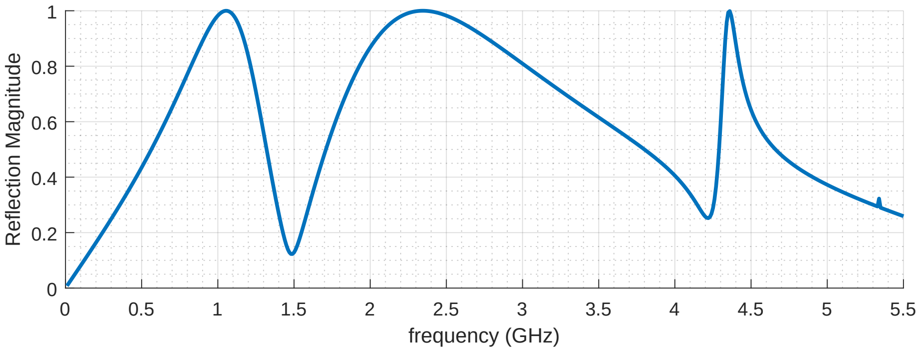

(a)

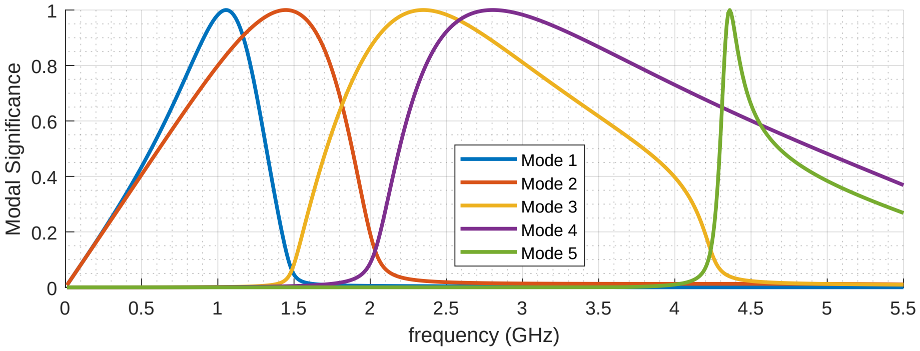

(b)

Figure 4.44: 2-layer FSS element that consists of loaded metal ring elements on the both layers, illuminated by an x-polarized plane wave. (a) The reflection magnitude. (b) The modal significance values.

In order to shift the total reflection frequency of the lower band from 1.44 to 1 GHz and the upper band from 2.81 to 2.3 GHz, ring-type metal elements on top and bottom layers are loaded with 25.7 nH and 5 nH, respectively. Note that these values are already calculated for the example of two concentric rings in the previous section. As load elements are applied on northernmost and southernmost nodes of the both metal rings, the resulting reflection magnitude and the modal significance values are shown in Fig. 4.44a and Fig. 4.44b, respectively. As can be seen from the figure, 1st, 3rd and 5th modes are excited by the x-polarized plane wave and due to the loading, the resonance frequencies of the 1st and 3rd modes are shifted to 2.35 and 1.05 GHz, respectively. As a result, total reflection frequencies are also shifted to these frequencies which are very close to the desired values.

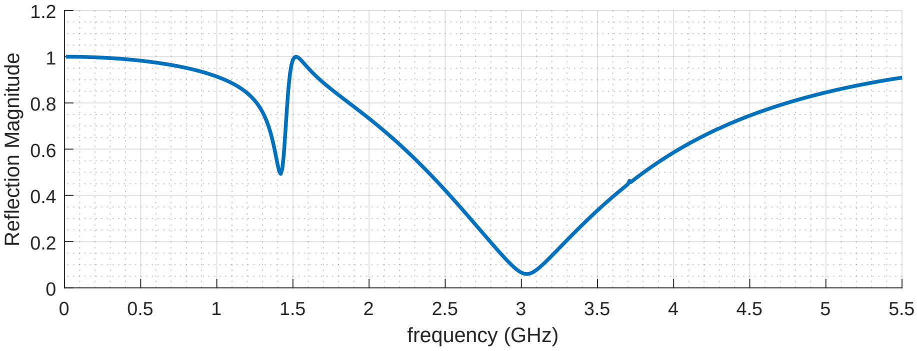

(a)

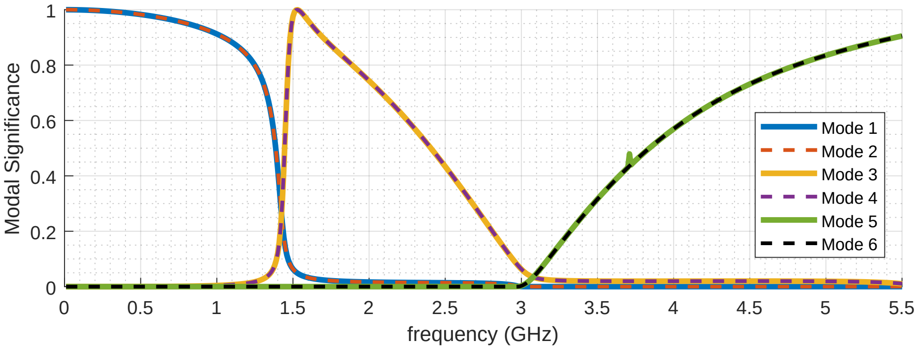

(b)

Figure 4.45: 2-layer FSS element that consists of an unloaded metal ring on the top layer and an unloaded slot element on the bottom layer, illuminated by an x-polarized plane wave. (a) The reflection magnitude. (b) The modal significance values.

In the next analysis, the unit cell element in Fig. 4.42b is solved for the x-polarized plane wave where the element on the top layer is an unloaded ring-type metal, whereas the element on the bottom layer is an unloaded ring-type slot. In Fig. 4.45, the resulting reflection magnitude and the modal significance values of the first 6 modes are given. Similar to the case of total reflection around 2.8 GHz when the element on the bottom layer is a ring-type metal, total transmission has occurred around this frequency due to the complementary slot element. The total reflection frequency due to the ring element and the total transmission frequency due to the slot element are very close to the total reflection frequencies of the problem when both elements are metal, and become 1.52 GHz and 3.04 GHz, respectively.

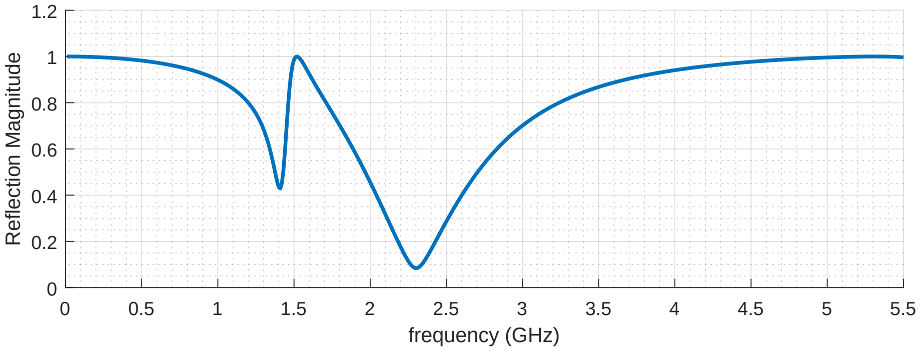

(a)

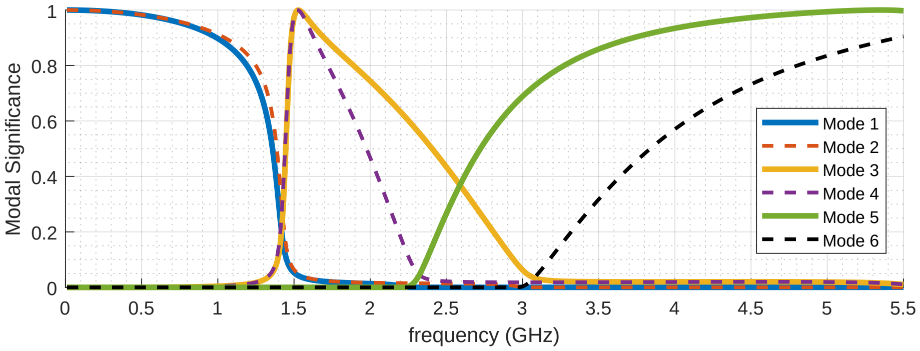

(b)

Figure 4.46: 2-layer FSS element that consists of an unloaded metal ring element on the top layer and a loaded slot element on the bottom layer, illuminated by an x-polarized plane wave. (a) The reflection magnitude. (b) The modal significance values.

Since 5 nH of inductance can be applied to shift the total reflection frequency of the upper band to 2.3 GHz, the corresponding capacitance value according to (4.15a) can also be calculated for the complementary problem to shift total transmission frequency of the upper band to 2.3 GHz as well. The capacitive load of the complementary problem is found as $C_{\text{bottom}} = 0.141$ pF and applied on the easternmost and westernmost nodes of the slot element using the mesh structure in Fig. 4.42c. In order to observe the effect of the capacitive load on the slot element only, the metal element on the top layer is initially kept unloaded. The resulting values of the reflection magnitude and the modal significance values of the first 6 modes under x-polarized incidence are shown in Fig. 4.46. As Fig. 4.46b is compared with Fig. 4.45b, it can

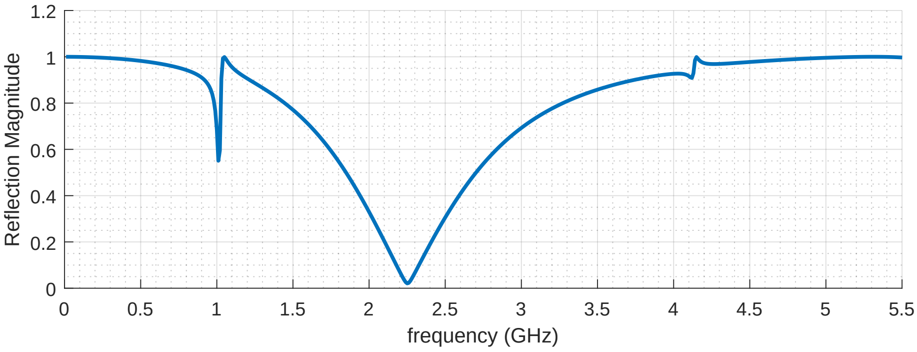

(a)

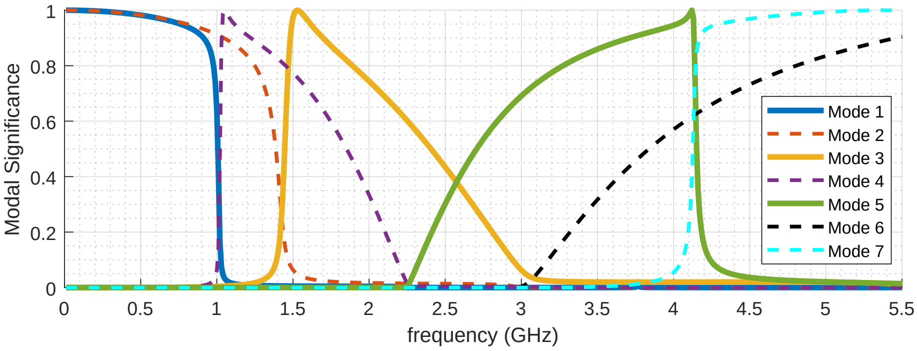

(b)

Figure 4.47: 2-layer FSS element that consists of a loaded metal ring element on the top layer and a loaded slot element on the bottom layer, illuminated by an x-polarized plane wave. (a) The reflection magnitude. (b) The modal significance values.

be seen that 4th and 5th modes are shifted together due to the load. Hence, the total transmission frequency is shifted to 2.3 GHz, which is the desired result. However, since the metal element on the top layer is not loaded, neither 1st nor the 2nd mode is shifted, hence the total reflection frequency does not change.

In order to shift the total reflection frequency to 1 GHz as well, the metal element on the top layer is also loaded with $L_{\text{top}} = 25.7$ nH while keeping the capacitive loading on the bottom layer. The reflection magnitude and the modal significance values of the first 7 modes for this case are also given in Fig. 4.47a and Fig. 4.47b, respectively. As expected, not only 4th and 5th modes are shifted but also the 1st mode due to the inductive loads on the top layer. As a result, the total transmission frequency and the total reflection frequency have become 2.25 and 1.05 GHz, respectively. These frequency values are very close to the desired values of 2.3 and 1 GHz.

As a conclusion, the proposed method has been demonstrated for ring-type FSS elements in different shapes including elements consisting of multiple rings. The analyses yield very successful results. Further discussion is given in Chapter 6.

CHAPTER 5

CHARACTERISTIC MODES AS MACRO BASIS FUNCTIONS IN LARGE ARRAYS

Fast and efficient solution of integro-differential equations is a widely studied topic. In order to obtain an accurate solution using the Method of Moments, the subdomain size must be kept between $\lambda/10$ and $\lambda/20$. This condition would cause the number of unknowns to increase as the size of the structure increases. Hence, effective acceleration methods are needed to reduce the computational burden.

In the solution of large array structures, the first approach that comes to mind for a low-cost solution is infinite array approach. As a matter of fact, the unit cell method described in the previous chapters would provide a fast and effective solution. However, the major drawbacks of the unit cell solution are that all array elements are assumed to be identical and discontinuities at the edges of the finite structure are neglected. In addition, there may be non-periodic elements in the solution domain, which cannot be included inside the unit cell boundaries.

In recent years, fast multipole method (FMM) [96] and its extended version as the multilevel fast multipole algorithm (MLFMA) [97] have been incorporated into the MoM-based integral equation solutions to reduce the computational burden. Similarly iterative methods including the adaptive integral method (AIM) [98] and the adaptive cross approximation (ACA) algorithm [99] are developed to speed up the computation time of the MoM solution. Although these methods can speed up the computation of large scattering bodies, the size of the basis function would still range from $\lambda/10$ to $\lambda/20$, which leads to large matrices. In order to reduce the number of unknowns, macro basis functions (MBFs) [15], and especially the characteristic basis function method (CBFM) [16, 17] can be considered.

Unlike the conventional MoM solution with subdomain basis functions, the geometry can be divided into larger blocks proportional to the wavelength. Defining macro basis function on each block, the impedance matrix size can be reduced, and in this fashion the electrically large structures can be solved efficiently. In the CBFM, each block must be extended to ensure the continuity between the blocks [16]. However in the solution of arrays, array elements can be considered as distinct blocks, thus macro basis functions can be expanded over them. In this method, first the primary characteristic basis functions (CBFs) are calculated from the self-interaction of each block, then the secondary CBFs are found by calculating currents induced by the primary CBFs on neighboring elements. Note that secondary CBFs due to the far interactions can be discarded and the CBFs redundant to the solution can be eliminated using the singular value decomposition (SVD). However instead of having secondary basis functions, excitation-free CBFs can also be implemented by finding primary MBFs for different excitations, especially in the solution of elements under multiple illuminations [100, 101]. Using acceleration methods including Jacobi Method [102, 103], Domain Green's Function Method [104] and MLFMA [105] within the methodology of the CBFM, much faster and cheaper solutions can be achieved.

In [18] and [19], the multilevel CBFM (MLCBFM) is also presented for the solution of large structures and arrays. Utilizing blocks in different levels, the multilevel approach would reduce the degree of freedom even further. The largest computational burden in CBFM is the filling of the reduced matrix. To reduce such a burden, ACA algorithm [106], FMM [105] and the interpolation method presented in [107] can be considered.

The characteristic modes can also be incorporated as macro basis functions. Since CM analysis is independent of the excitation, same modes can be implemented for different excitations. In [20], characteristic modes are introduced as basis functions for the microstrip array of identical elements. In [108], periodic characteristic mode analysis is proposed to perform matrix reduction for large finite periodic arrays effectively. In order to demonstrate usability of the same characteristic modes over array elements of different sizes, an analysis of reflectarray is presented in [21]. In this solution, a tabulation based on the element size and the element distance is also demonstrated, which accelerates the generation of the reduced matrix entities. Besides, it has been argued that using the first couple of modes would suffice to calculate the far field with a certain accuracy. However, when it comes to the calculation of near field and the surface current, more modes are needed for an accurate solution. In addition to this, as the difference between the size of array element becomes too large, the utilized modes would become insufficient to represent the current on the largest elements. Therefore in such case, number of modes must also be increased. However increasing the number of modes would cause larger reduced matrices.

In this chapter, characteristic modes are demonstrated as macro basis functions. The characteristic basis function method is explained and the use of characteristic modes as primary CBFs in the context of CBFM is discussed. By calculating secondary CBFs from the characteristic modes, the interactions between array elements can be represented by basis functions free of excitation. Although the inclusion of secondary CBFs increases the matrix size, using characteristic modes as primary CBFs may become advantageous over the conventional CBFM due to the excitation-free and reusable nature of the modes as discussed in [21]. This study is also reported in [109]. Afterwards the methodology of the MLCBFM is briefly described and incorporation of the characteristic modes into the MLCBFM is introduced as an original study.

5.1 The Characteristic Modes as Basis Functions

In the theory of the characteristic modes, the solution of the eigenvalue equation for $N \times N$ matrix would produce N different eigenvalues. Therefore, the number of modes are equal to the number of subdomain basis functions that is utilized in the MoM solution. However, it is sufficient to consider only a few modes of near resonance since the significant modes are more likely to make the most contribution to the solution. In order to illustrate the contribution of the significant modes, the surface current is solved over a single rectangular PEC plate of 10 cm $\times$ 4 cm. As can be recalled from Chapter 2, the modal significance values of the first 6 modes of this element from 0.5 and 5 GHz are already given in Fig. 2.7b. In this example, the rectangular plate is illuminated by a y-polarized plane wave of normal incidence at 2.4 GHz.

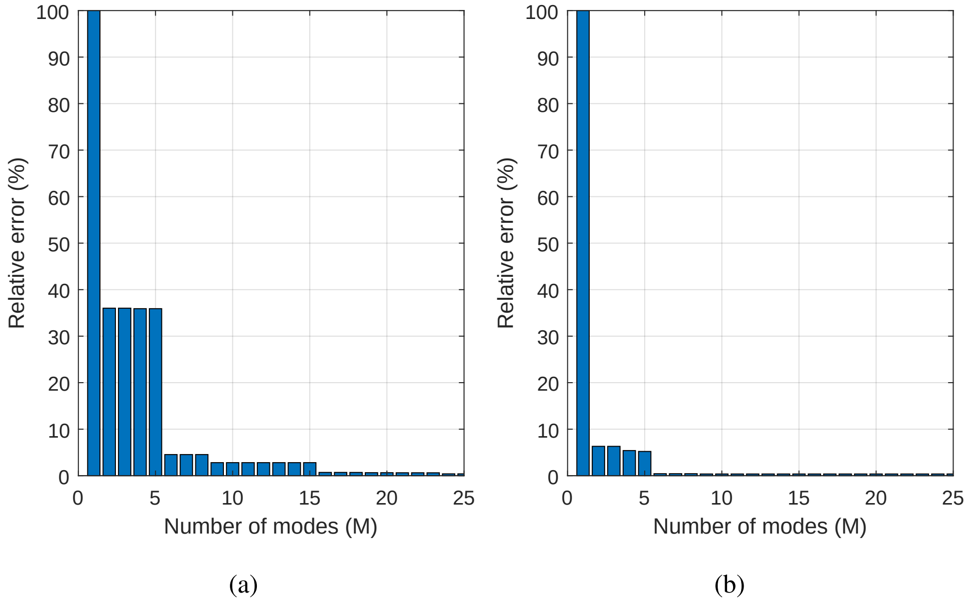

(a) (b)

Figure 5.1: Relative error of using first M CMs as basis functions. (a)The error in the absolute value of the current. (b) The error in the real part of the current.

A relative error between the solutions of the surface current, one calculated by using RWG functions in the context of the conventional MoM, and the other obtained by (2.44) using the first M modes as basis functions is given in Fig. 5.1. The relative error is formulated as

$$\text{Error} = \frac{\sqrt{\sum_{n=1}^{N} |I_n - \breve{I}_n|^2}}{\sqrt{\sum_{n=1}^{N} |I_n|^2}} \times 100 \tag{5.1}$$

where $\mathbf{I}$ is associated with the current found directly from the conventional MoM solution with RWG basis functions. Whereas $\breve{\mathbf{I}}$ is the weighted sum of first M CM basis functions as

$$\breve{\mathbf{I}} = \sum_{m=1}^{M} a_m \mathbf{J}_m. \tag{5.2}$$

As can be seen from Fig. 5.1a, the contribution of the second mode drops the relative error from 100% to 36%. However, this error comes mostly from the imaginary part of the current. In Fig. 5.1b, the relative error in the real part of the current is given, in which the contribution of the first 2 modes makes the relative error about 6%.

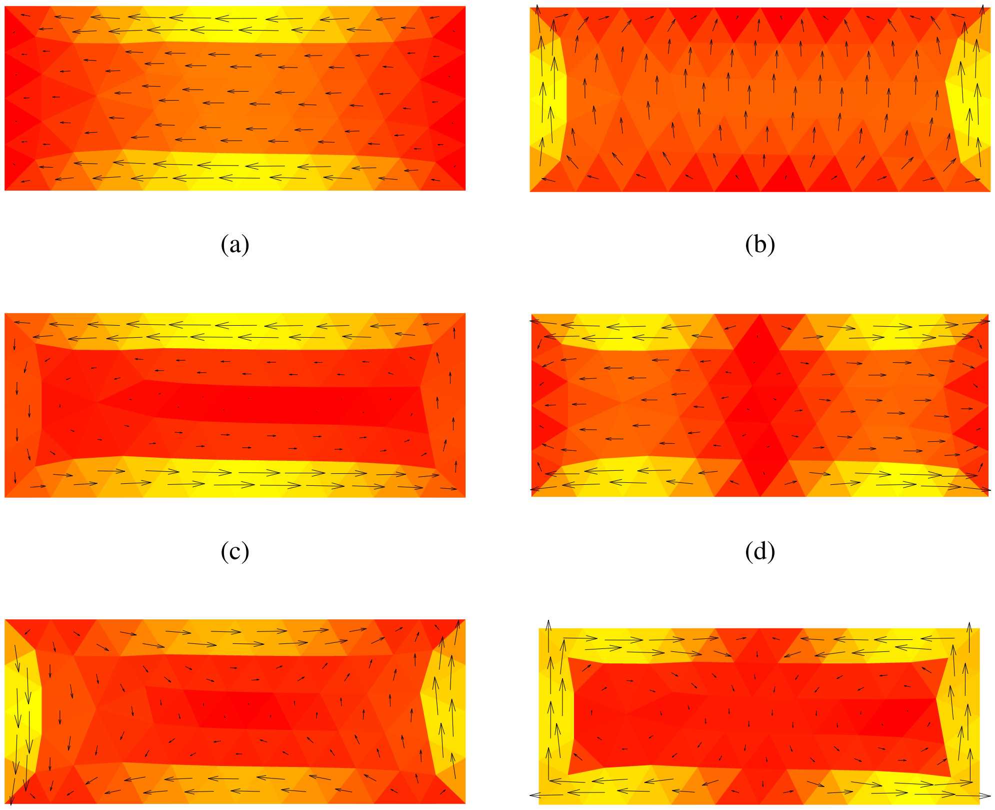
(a) (b) (c) (d) (e) (f)

Figure 5.2: Eigencurrents on rectangular PEC plate of 10 cm × 4 cm, at 2.4 GHz. (a) Mode 1. (b) Mode 2. (c) Mode 3. (d) Mode 4. (e) Mode 5. (f) Mode 6.

The numerical inaccuracies in both the MoM solution and the solution of the generalized eigenvalue equation inevitably contribute to the relative error. Hence, although the illumination over the rectangular plate mostly excites the 2nd mode, using the 2nd mode alone does not reduce the error to zero. Even when 25 CM basis function are incorporated into the solution, the relative error becomes very low but not zero. However, since only the first few modes with low eigenvalues can be excited within the given excitation, utilizing higher order modes as basis functions would not bring any significant improvement to the solution accuracy but in return, it would increase the computational burden. The modal currents of the first 6 characteristic modes are also depicted in Fig. 5.2. As expected, since the plate is excited by a y-polarized plane wave, the 2nd mode that contributes most to the solution has the current flowing in the y direction. The contributions can also be observed from the modal weighting coefficients. In Fig. 5.3, the weighting coefficients, the modal significance values as well as the characteristic angles of the first 6 modes are also plotted. The characteristic angles imply that 1st, 3rd and 6th modes are inductive, whereas 2nd, 4th and 5th modes can be regarded as capacitive modes. Note that the modal significance values do not decrease with respect to the mode index due to the mode tracking which is applied according to 0.5 GHz, as shown in Fig. 2.7b.

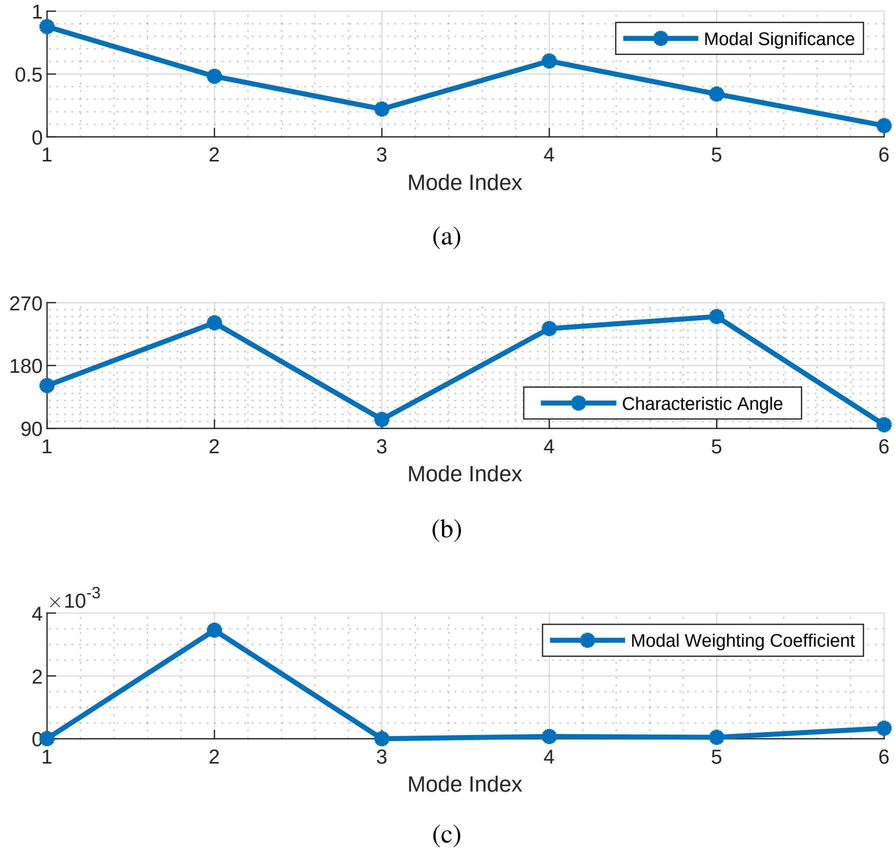

(a)

(b)

(c)

Figure 5.3: Rectangular PEC plate of 10 cm × 4 cm, illuminated by y-polarized plane wave of normal incidence at 2.4 GHz. (a) Modal significance values. (b) Characteristic angles. (c) Modal weighting coefficients.

5.2 Matrix Reduction Using Macro Basis Functions

Having successfully demonstrated that characteristic modes can be used as basis functions, this section shows how characteristic modes can be utilized as macro basis

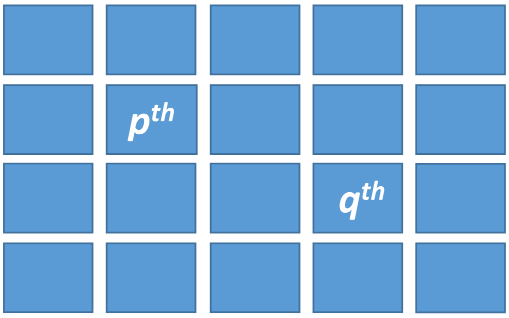

Figure 5.4: 20-element array of patch elements.

functions to reduce the number of unknowns. Therefore first, the matrix reduction technique is explained in the context of CBFM, then the advantages of using characteristic modes as macro basis functions over CBFM are discussed.

5.2.1 The Characteristic Basis Function Method (CBFM)

In the CBFM solution, the structure is divided into sub-blocks. However, in the problem of large array structures, each array element can be treated as a sub-block. As an illustration, a patch array consisting 20 elements is depicted in Fig. 5.4. Hence, this specific problem consists of 20 blocks. The MoM matrix and the excitation vector obtained using subdomain basis functions are presented in terms of sub-matrices and sub-vectors as

$$\mathbf{Z} = \begin{bmatrix} \ddots & \vdots & \vdots & \vdots & \vdots \\ \cdots & \mathbf{Z}_{pp} & \cdots & \mathbf{Z}_{pq} & \cdots \\ \vdots & \vdots & \vdots & \vdots & \vdots \\ \cdots & \mathbf{Z}_{qp} & \cdots & \mathbf{Z}_{qq} & \cdots \\ \vdots & \vdots & \vdots & \vdots & \ddots \end{bmatrix} \qquad \mathbf{V} = \begin{bmatrix} \vdots \\ \mathbf{V}_p \\ \vdots \\ \mathbf{V}_q \\ \vdots \end{bmatrix}. \tag{5.3}$$

In this representation, the diagonal sub-matrices correspond to the element solutions that are isolated from the rest of the array. In this context, $\mathbf{Z}_{pp}$ and $\mathbf{Z}_{qq}$ correspond to the MoM matrices of isolated pth and qth elements, respectively. Besides that, $\mathbf{Z}_{qp}$ and $\mathbf{Z}_{pq}$ sub-matrices correspond to the interaction between the pth and qth elements. Using the excitation vector $\mathbf{V}_p$ that corresponds to the pth element, the solution of the vector matrix multiplication,

$$\mathbf{Z}_{pp}\mathbf{I}_p = \mathbf{V}_p \tag{5.4}$$

gives the first macro basis function over the pth element as $\mathbf{I}_p$, which is called as the primary basis function.

Due to the coupling between array elements, using only one macro basis function on each array element would not be sufficient for an accurate solution. For this reason, secondary basis functions are introduced to obtain macro basis functions which are orthogonal to each other and better represent the current distribution over the array. In order to calculate secondary basis functions within the CBFM, the primary basis functions are treated as distant current sources for the neighboring array elements. Hence, the excitation on the qth element due to the current source $\mathbf{I}_p$ can be defined as

$$\mathbf{V}_{qp} = -\mathbf{Z}_{qp}\mathbf{I}_p. \tag{5.5}$$

Subsequently the induced current over the qth element due to such radiation yields the secondary basis function $\mathbf{I}^s_{qp}$, which can be calculated from the solution of the vector matrix multiplication in (5.6).

$$\mathbf{Z}_{qq}\mathbf{I}^s_{qp} = \mathbf{V}_{qp} \tag{5.6}$$

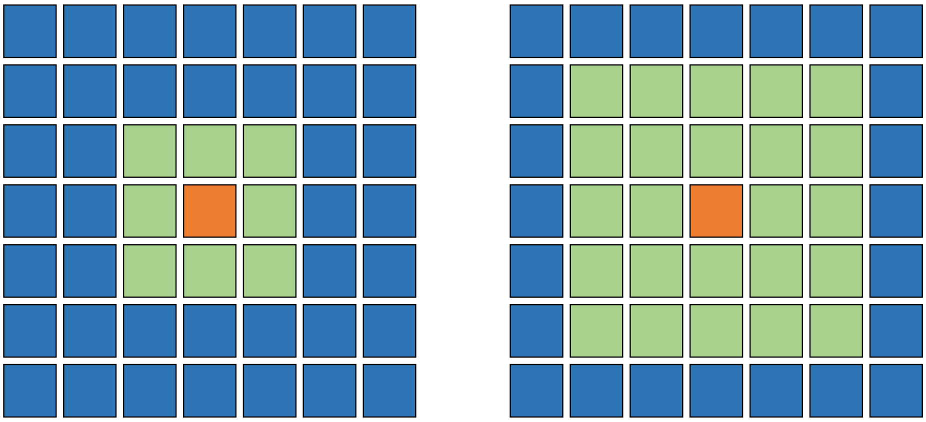

(a) (b)

Figure 5.5: (a) 1st-order neighboring. (b) 2nd-order neighboring.

In the solution of the 20-element array, 1 primary basis function can be defined along with maximum 19 secondary basis functions for each element. Therefore, if 20 MBFs are defined on each element, the size of the matrix becomes 400×400. However, the matrix can be further reduced by neglecting distant interactions at some extend. Hence in the solution of large arrays, the interactions between elements of either 1st or 2nd order neighboring can be taken into account to keep the matrix small. The cases of 1st and 2nd order neighboring are depicted in Fig. 5.5. It can be deduced from Fig. 5.5a that along with 1 primary basis function, maximum 8 secondary basis functions can be defined in the case of 1st order neighboring. Whereas in the case of the 2nd order neighboring, up to 24 secondary basis function can be defined, as shown in Fig. 5.5b. Note that unlike the depiction in Fig. 5.5, such neighboring can also be realized by neglecting the elements in farthest corners. Once primary and secondary functions are calculated for each element, the macro basis functions are grouped in matrices. For instance, the set of basis functions in matrix form that corresponds to pth element can be presented as

$$\mathbf{J}_p = \begin{bmatrix} \mathbf{I}_p & \mathbf{I}^s_{p1} & \mathbf{I}^s_{p2} & \mathbf{I}^s_{p3} & \cdots \end{bmatrix}. \tag{5.7}$$

Before the calculation of the reduced matrix, the singular value decomposition [110] is applied to the set of basis functions in order to ensure the orthogonality. After the SVD procedure, the new basis set is sorted according to the singular values. Besides that, basis functions with singular values below a certain threshold are removed from the basis set. Hence, secondary CBFs that are not adequately independent from other MBFs are being removed. Apart from reducing the matrix size even further, SVD also improves the condition number of the matrix. The singular values are also normalized as proposed in [106]. Throughout this work, the threshold of the normalized singular values is set to 10^{-3}. Once the macro basis function sets are obtained, the reduced impedance matrix and the reduced excitation vector can be calculated as given in (5.8a) and (5.8b), respectively.

$$\mathbf{Z}^{\mathrm{r}}_{pq} = \mathbf{J}^T_p \mathbf{Z}_{pq} \mathbf{J}_q \tag{5.8a}$$

$$\mathbf{V}^{\mathrm{r}}_p = \mathbf{J}^T_p \mathbf{V}_p \tag{5.8b}$$

5.2.2 The Characteristic Modes as Macro Basis Functions

As briefly discussed at the beginning of this chapter, filling the reduced impedance matrix is the most expensive part of the computation. By exploiting symmetries in the problem as well as utilizing several methods including ACA algorithm [106] and interpolation techniques [107], the computational cost of this stage is usually reduced. However, when the goal is to solve the array structure for different illuminations, MBFs and the resulting reduced matrix must be calculated over and over for different excitations. The computational burden of such problem has led to the search for excitation independent macro basis functions. In order to address this problem, using multiple primary basis functions resulting from different incidences is proposed in [101].

Nevertheless the first few significant modes in the analysis of characteristic modes are very prone to resonance by any illumination. Hence, characteristic modes become perfect candidates to be utilized as excitation independent MBFs in the matrix reduction. Therefore once the reduced matrix is obtained, the same matrix can be reused in the solution of the array for different illuminations. Moreover, when the array elements are either identical or having dimensions close to each other, it is possible to utilize exactly the same modal currents as MBFs over the elements. However, keep in mind that as the size differences between array elements increase, more modes will be needed to model the surface current on the larger elements than on the smaller elements. Using redundant modes as MBFs on smaller elements would increase the computational load, whereas using less than necessary modes over larger elements may reduce the solution accuracy. In the conventional MoM solution with RWG basis functions, if each array element consists of N RWGs, an array size of P would lead an impedance matrix of $PN \times PN$. However, as M CMs are utilized as basis functions on each element, the size of the reduce matrix would reduce from $PN \times PN$ to $PM \times PM$ where $M << N$.

In [21], a solution method is demonstrated for array of differently sized elements. In this solution, array elements are scaled and by keeping the mesh structure same on each element, same characteristic modes are used on differently sized elements. A tabulation method has also been developed in [21] to cope with the computational load of filling the reduced matrix. In this tabulation, the elements of the reduced matrix that determine the interactions between the elements are expressed as functions of the element size and the distances between the elements. Hence, only certain regions of the reduced matrix are calculated while the rest is filled using the tabulation. In this respect, characteristic modes can become very advantageous as macro basic functions.

Although using only significant modes as MBFs would be sufficient to achieve an accurate solution, the secondary basis functions resulting from CMs can also be calculated and incorporated into the solution. As already been demonstrated as a part of the work in [109], the inclusion of secondary MBFs significantly increases the size of the reduced matrix. After applying SVD, redundant secondary functions with very low singular values can still be eliminated. Since the modes are sorted according to their closeness to resonance, using only a very few modes and their corresponding secondary functions would ensure the accuracy of the solution. Using secondary basis functions obtained from characteristic modes can become more advantageous compared to the conventional CBFM when the excitation-free nature and the reusability of the modes for scaled elements are exploited well.

5.3 Application of the Matrix Reduction with CM Basis Functions

In this section, the periodic structures are initially solved using the straightforward MoM with RWG basis functions. Then the matrix reduction is performed using the characteristic modes as macro basis functions. In order to investigate the accuracy under different illuminations, the array is solved for a spectrum of plane waves of $0^\circ \leq \theta_i \leq 60^\circ$ and $0^\circ \leq \phi_i \leq 90^\circ$ with angular step of $N_\theta = 30^\circ$ and $N_\phi = 2^\circ$. The plane wave expression used in the solutions can be given as

$$\begin{aligned}\mathbf{E_i} = & \left[-\hat{\mathbf{x}}\cos\theta_i\cos\phi_i - \hat{\mathbf{y}}\cos\theta_i\sin\phi_i + \hat{\mathbf{z}}\sin\theta_i\right] \times \\ & \exp\left\{jk\left(\hat{\mathbf{x}}\sin\theta_i\cos\phi_i + \hat{\mathbf{y}}\sin\theta_i\sin\phi_i + \hat{\mathbf{z}}\cos\theta_i\right)\right\}.\end{aligned} \tag{5.9}$$

In order to determine the accuracy of the solutions, the relative error before and after the reduction is calculated using (5.1). In this case, $\breve{\mathbf{I}}$ represents the solution of the reduced matrix for array of P elements, which can be calculated as

$$\breve{\mathbf{I}}_{\mathbf{p}} = \mathbf{J}_p \mathbf{U}_P \tag{5.10}$$

where $\mathbf{U}$ is the solution of the reduced matrix,

$$\mathbf{U} = \begin{bmatrix} \mathbf{U}_1 \\ \mathbf{U}_2 \\ \vdots \\ \mathbf{U}_{P-1} \\ \mathbf{U}_P \end{bmatrix} = \{\mathbf{Z}^{\mathrm{r}}\}^{-1}\mathbf{V}^{\mathrm{r}}. \tag{5.11}$$

5.3.1 Solution of the Square Patch Array

The first example is an 8×8 array composed of square unit patch elements as depicted in Fig. 5.6a. The size of the square patch is 10 mm and the period is 15 mm both in x and y directions. The element consists of 133 RWG functions as shown in Fig. 5.6b, hence the number of unknowns for 64-element array becomes 8512.

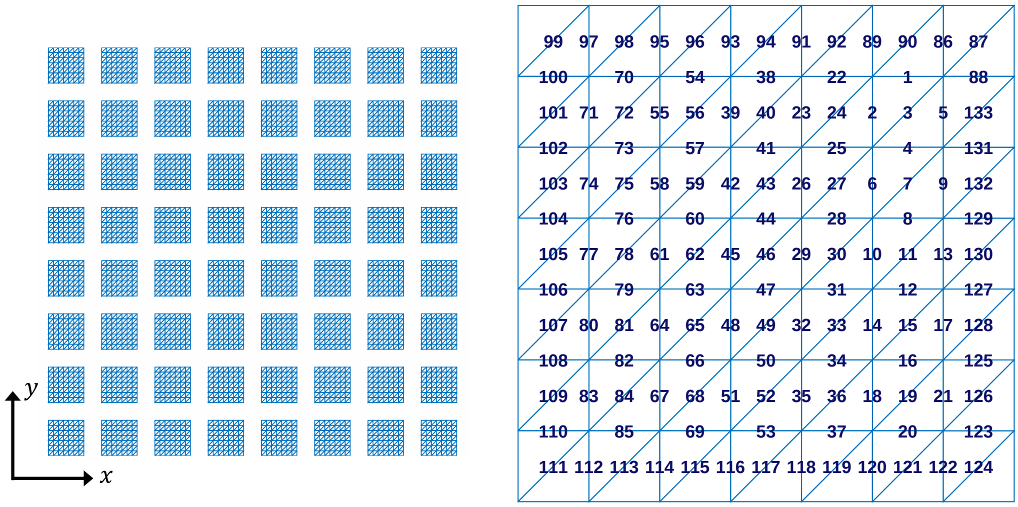

(a) (b)

Figure 5.6: (a) Meshing configuration of the 64-element array. (b) RWG basis functions on the square patch element.

In the initial analysis, the matrix reduction is performed on the 64-element square patch array at 8 and 15 GHz under normal incidence using the CMs as macro basis functions. The relative error and the reduced matrix size according to the first M number of modes are given in Table 5.1. The characteristic modes are utilized as basis functions in the order of significance. As can be seen from the table, using the first 10 modes at 8 GHz and the first 14 modes at 15 GHz, the relative error drops below 1%. The dimension of the impedance matrix is reduced from 8512 to 640 and 896 at 8 GHz and 15 GHz, respectively. The error decreases more rapidly at the lower frequency since less number of CM basis functions affect the current density on lower frequencies.

Table 5.1: Solution of 64-element square patch array using CM basis functions

# of CMs	f (GHz)	Reduced Matrix Size	Relative Error ($\%$)
2	8	128×128	24.75
4	8	256×256	22.84
6	8	384×384	22.80
8	8	512×512	1.78
10	8	640×640	0.97
12	8	768×768	0.66
14	8	896×896	0.38
16	8	1024×1024	0.33
18	8	1152×1152	0.31
20	8	1280×1280	0.31
2	15	128×128	30.63
4	15	256×256	8.04
6	15	384×384	7.88
8	15	512×512	4.28
10	15	640×640	1.85
12	15	768×768	1.56
14	15	896×896	0.73
16	15	1024×1024	0.59
18	15	1152×1152	0.53
20	15	1280×1280	0.48

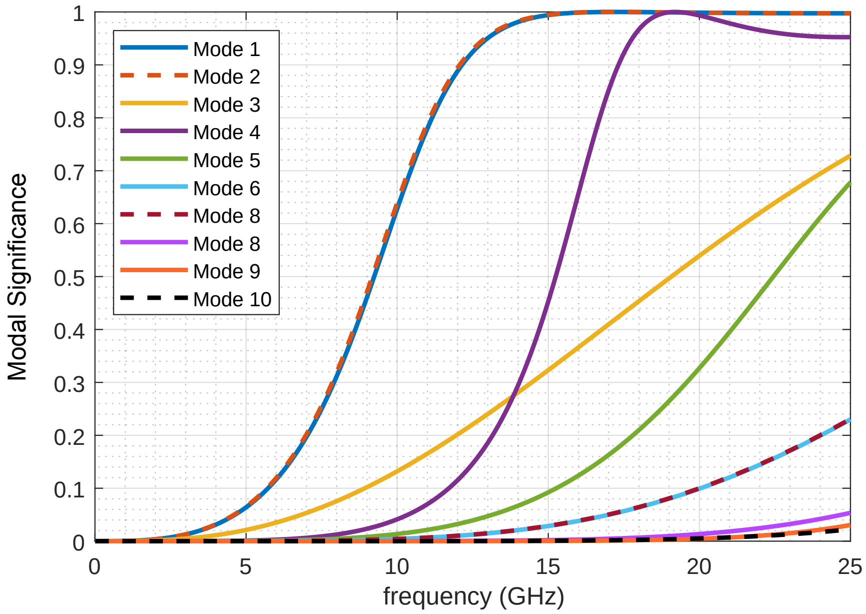

Figure 5.7: MS values of the 10 cm square element.

In Fig. 5.7, modal significance values of the 10 cm square element for the first 10 modes are plotted under normal incidence. As can be seen from the figure, only the first 4 modes have almost non-zero modal significance values at 8 GHz, however at 15 GHz, the first 2 modes are almost at resonance and more modes can be excited due to the plane wave illumination or the element interactions. Hence, more number of modes are needed at 15 GHz to model the reduced matrix solution accurately.

In the next analysis, the matrix reduction is performed at 8 GHz using the first 10 modes. Then the reduced matrix is calculated in the case of $\theta_i = \phi_i = 0$ for once and stored. Then the stored matrix is utilized in the solution of the array under different illuminations. The relative error is given in Fig. 5.8a. The same procedure is also repeated at 15 GHz using the first 14 CMs and the corresponding errors are also plotted in Fig. 5.8b. It can be seen that same reduced matrix can be utilized for different incidences and yet the relative errors according to different propagation and polarization angles become very close to each other. Note that although the reduced impedance matrix is calculated once, the reduced excitation vector still needs to be calculated for every different incidence. Nevertheless, the computational cost of the reduced excitation vector is much lower compared to the reduced matrix generation.

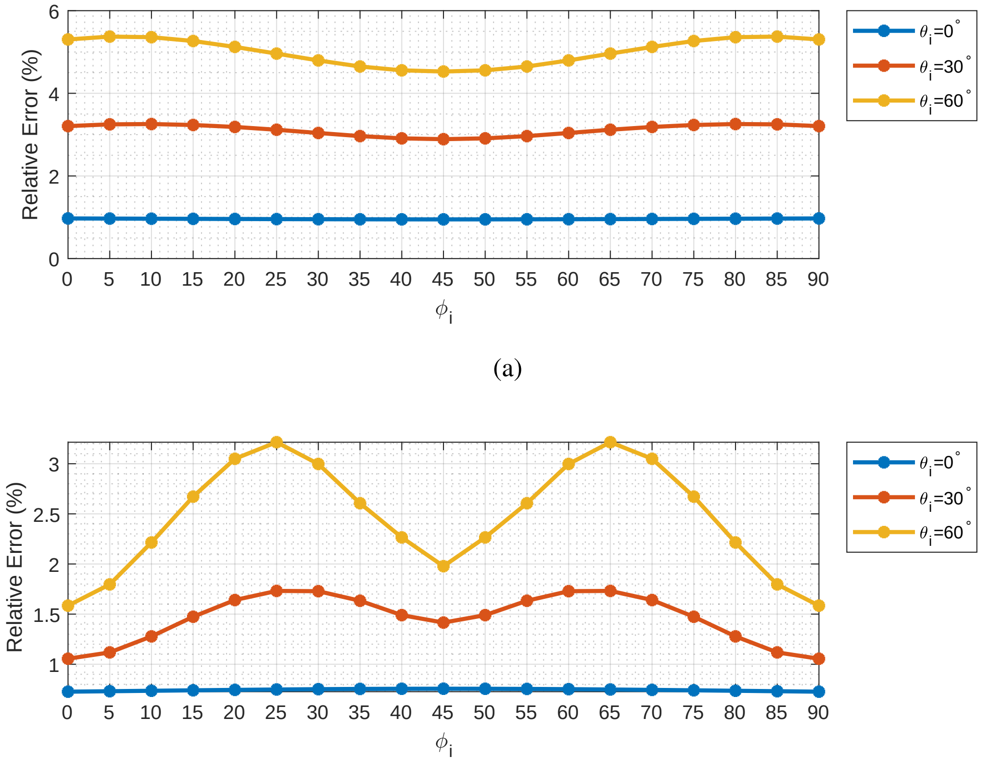

(a)

(b)

Figure 5.8: The relative error of the matrix reduction using CMs, as a function of ϕ_i. (a) The solution at 8 GHz using the first 10 CMs. (b) The solution at 15 GHz using the first 14 CMs.

Table 5.2: Solution of 64-element array using CMs as primary basis functions and secondary basis functions from the interactions of elements.

# of CMs	f (GHz)	Reduced Matrix Size	Relative Error (%)
1	8	656×656	45.03
2	8	1016×1016	3.95
1	15	800×800	55.31
2	15	1124×1124	6.63
4	15	1320×1320	1.03

Besides using the characteristic modes only as macro basis functions, the solution can also be realized by considering CMs as primary basis functions and incorporating secondary functions, that are calculated from the interaction of characteristic modes on neighboring array elements, into the solution. In Table 5.2, the relative error and the reduced matrix size according to the mode number are given for the normal incidence of $\theta_i = \phi_i = 0$. Similar to the previous solution, modes are utilized in the order of significance and 2nd order neighboring is considered. The redundant basis functions are eliminated through SVD and the threshold for normalized singular values is set to 10^{-3}. As can be seen from the table, only the first 2 characteristic modes and the first 4 characteristic modes would be sufficient to achieve a relative error around 4% and 1% at 8 GHz and 15 GHz, respectively.

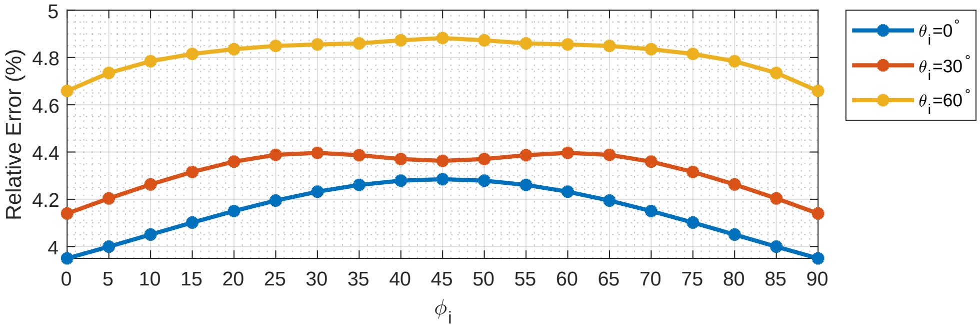

(a)

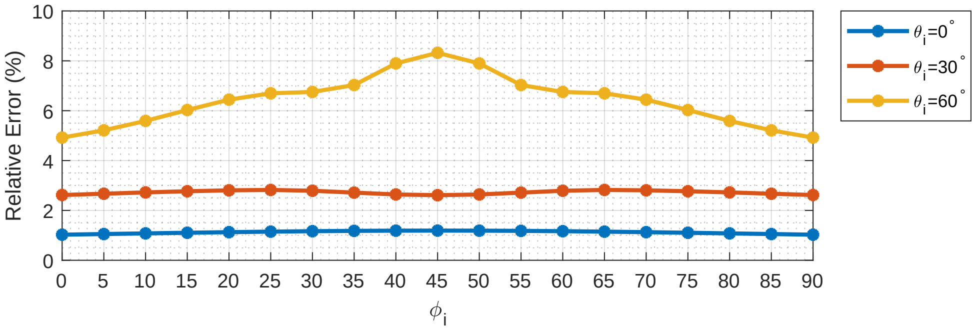

(b)

Figure 5.9: The relative error using CMs as primary basis functions and secondary basis functions from the interactions of elements. (a) The solution at 8 GHz using the first 2 CMs. (b) The solution at 15 GHz using the first 4 CMs.

Although incorporation of the secondary basis functions significantly increase the size of the reduced matrix, the secondary basis functions can still be included into the solution to ensure the accuracy. The solution is also performed for multiple excitations by implementing same basis functions. In Fig. 5.9a, relative error of the solution is shown for the first 2 CMs as primary basis functions and their secondaries at 8 GHz. Similarly in Fig. 5.9b, the relative error with the first 4 CMs and the corresponding secondary basis functions is given at 15 GHz. As can be seen, the relative error slightly increases as the elevation angle increases. Hence, more modes are needed in the case of oblique incidence.

5.3.2 Solution for Array of Identical and Scaled Ring Elements

Having successfully demonstrated CMs as excitation independent MBFs, the next step is to demonstrate the matrix reduction of the array of differently sized elements. In this analysis, a 16×8 array of circular ring elements are utilized. In the first example, the array is constructed by identical ring elements with inner radius of 2.5 cm and outer radius of 3 cm. The period is 8 cm both in x and y directions. The element is meshed in such a way that 64 RWG functions are defined on each element as shown in Fig. 5.10. Hence, the overall number of RWG basis functions used in the MoM solution is 8192. In Fig. 5.11, the characteristic modes of the first 10

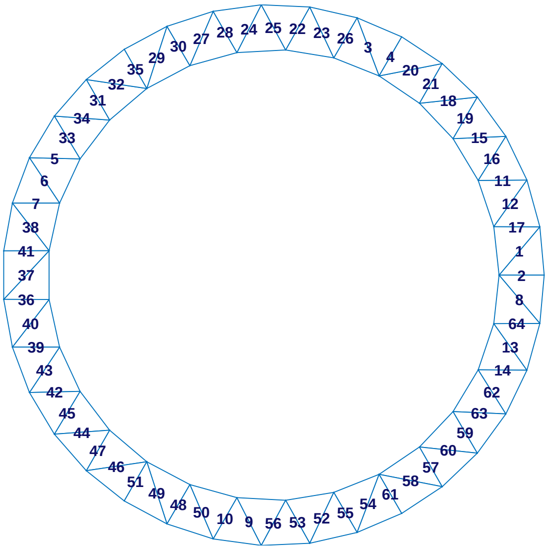

Figure 5.10: RWG basis functions on the circular ring element.

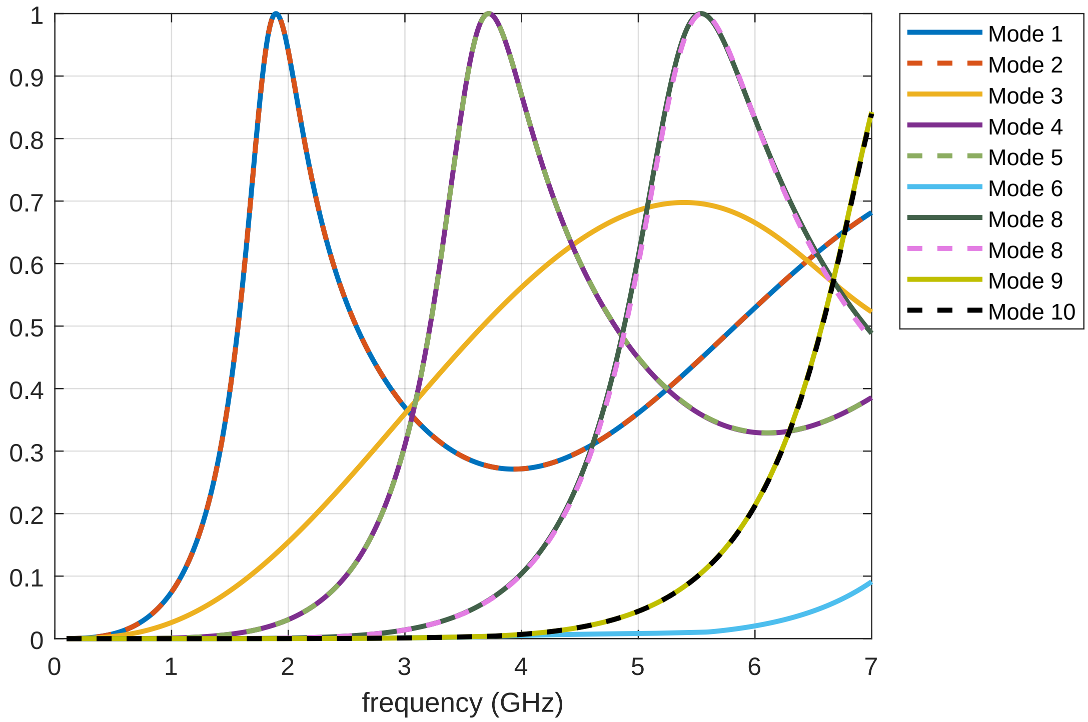

Figure 5.11: MS values of the circular ring element.

modes are given. As seen from the figure, the first 2 modes resonate at 1.9 GHz and the resonance frequencies for higher order modes are 3.7 and 5.5 GHz. In order to observe the influence of the first 2 CMs, the solution is carried out at 2 GHz, however to observe the need for more than 2 modes, the solution is also realized at 5 GHz.

In Table 5.3, the relative error and the corresponding matrix size are given according to the number of CM basis functions. In this solution, 128-element array of identical ring elements is illuminated by the normal incidence of $\theta_i = \phi_i = 0$. It can be seen that using the first 6 modes drops the relative error below 1% at 2 GHz. However at 5 GHz, first 16 CMs are needed to reduce the relative error below 1%.

Table 5.3: Solution of the 128-element array of identical circular ring elements using CMs as basis functions.

# of CMs	f (GHz)	Reduced Matrix Size	Relative Error (%)
2	2	256×256	5.00
4	2	512×512	1.57
6	2	768×768	1.13
8	2	1024×1024	0.10
10	2	1280×1280	0.10
2	5	256×256	99.96
4	5	512×512	99.95
6	5	768×768	85.20
8	5	1024×1024	7.38
10	5	1280×1280	5.26
12	5	1536×1536	4.41
14	5	1792×1792	4.38
16	5	2048×2048	0.47
18	5	2304×2304	0.35
20	5	2560×2560	0.26

In order to investigate the matrix reduction using the same characteristic modes on elements of different sizes, circular ring elements in the previous example are randomly scaled by scaling factor from 0.7 to 1.3. Similar to the previous example, the array period is kept 8 cm in both x and y directions. The resulting array structure is depicted in Fig. 5.12. The characteristic modes that have already been utilized on the array of identical elements are also utilized on the scaled elements at 5 GHz without any modification. The relative error and corresponding matrix sizes in the case of the normal incidence are given in Table 5.4. As can be seen, the relative error values for the array of differently sized elements are very close to the relative errors of the solution for the identical elements. These results indicate that CMs can be used as basis functions in the solution of reflectarray problems where the element dimensions vary as the phase tuning parameter.

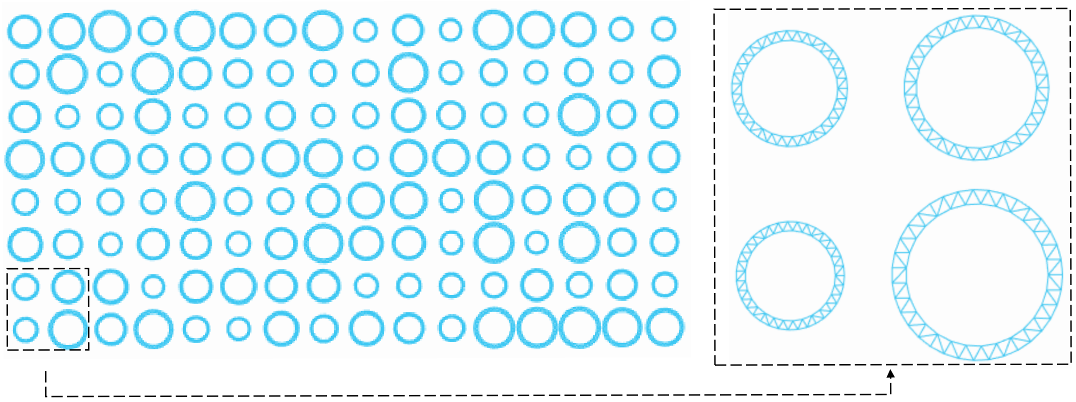

Figure 5.12: 128-element array of differently sized circular rings.

Table 5.4: Solution for the 128-element array of differently sized circular rings using CM basis functions.

# of CMs	f (GHz)	Reduced Matrix Size	Relative Error (%)
2	5	256×256	99.99
4	5	512×512	99.99
6	5	768×768	85.65
8	5	1024×1024	9.23
10	5	1280×1280	5.37
12	5	1536×1536	4.88
14	5	1792×1792	4.39
16	5	2048×2048	0.97
18	5	2304×2304	0.57
20	5	2560×2560	0.39

In the solution of reflectarray element, it is not necessary to reduce the error to 1% if the far field can be the only concern. As discussed in [21], the relative error of the far field is lower than the relative error of the surface current due to the far field approximations. However, when the near field solution is under concern, one can desire a relative error less than 1% in the stage of the matrix reduction. In the example of the array solution with ring elements, using the first 16 modes to reduce the relative error below 1% makes the reduced matrix dimension 2048, which is a quarter of the dimension of the MoM matrix that is obtained with RWG functions. Hence, especially in the calculation of the near field of large arrays, the matrix should be reduced more than the examples presented above. For this reason, multilevel matrix reduction using CM basis functions is proposed as an original work. Based on the multilevel CBFM, characteristic modes can be utilized in the first level of the matrix reduction. In the next section, the multilevel matrix reduction is briefly explained, then the results regarding the matrix reduction with CM basis functions are demonstrated.

5.4 Multilevel Matrix Reduction using Characteristic Modes

In the multilevel matrix reduction, the solution with RWG basis functions is Level-0. As can be recalled from Chapter 2, the matrix-vector multiplication in Level-0 can be represented as

$$\mathbf{Z}^{[0]}\mathbf{I}^{[0]} = \mathbf{V}^{[0]}. \tag{5.12}$$

The impedance matrix and the excitation vector for the array of P elements can be expressed as

$$\mathbf{Z}^{[0]} = \begin{bmatrix} [\mathbf{Z}_{11}^{[0]}]_{N_{0,1}\times N_{0,1}} & [\mathbf{Z}_{12}^{[0]}]_{N_{0,1}\times N_{0,2}} & \cdots & [\mathbf{Z}_{1\mathrm{P}}^{[0]}]_{N_{0,1}\times N_{0,\mathrm{P}}} \\ [\mathbf{Z}_{21}^{[0]}]_{N_{0,2}\times N_{0,1}} & [\mathbf{Z}_{22}^{[0]}]_{N_{0,2}\times N_{0,2}} & \cdots & \vdots \\ \vdots & \vdots & \ddots & \vdots \\ [\mathbf{Z}_{\mathrm{P}1}^{[0]}]_{N_{0,\mathrm{P}}\times N_{0,1}} & \cdot & \cdots & [\mathbf{Z}_{\mathrm{PP}}^{[0]}]_{N_{0,\mathrm{P}}\times N_{0,\mathrm{P}}} \end{bmatrix}_{\left\{\sum\limits_{p=1}^{P} N_{0,\mathrm{p}}\right\}\times\left\{\sum\limits_{p=1}^{P} N_{0,\mathrm{p}}\right\}} \tag{5.13a}$$

$$\mathbf{V}^{[0]} = \begin{bmatrix} [\mathbf{V}_{1}^{[0]}]_{N_{0,1}\times 1} \\ [\mathbf{V}_{2}^{[0]}]_{N_{0,2}\times 1} \\ \vdots \\ [\mathbf{V}_{\mathrm{P}}^{[0]}]_{N_{0,\mathrm{P}}\times 1} \end{bmatrix}_{\left\{\sum\limits_{p=1}^{P} N_{0,\mathrm{p}}\right\}\times 1} \tag{5.13b}$$

where $N_{0,\mathrm{p}}$ is the number of RWG elements in the pth element. If the discretization on each array element is kept the same using either identical or scaled elements, the number of RWGs on each element becomes N_0. Hence, corresponding impedance matrix and the excitation vector becomes

$$\mathbf{Z}^{[0]} = \begin{bmatrix} [\mathbf{Z}^{[0]}_{11}]_{N_0\times N_0} & [\mathbf{Z}^{[0]}_{12}]_{N_0\times N_0} & \cdots & [\mathbf{Z}^{[0]}_{1\mathrm{P}}]_{N_0\times N_0} \\ [\mathbf{Z}^{[0]}_{21}]_{N_0\times N_0} & [\mathbf{Z}^{[0]}_{22}]_{N_0\times N_0} & \cdots & \vdots \\ \vdots & \vdots & \ddots & \vdots \\ [\mathbf{Z}^{[0]}_{\mathrm{P}1}]_{N_0\times N_0} & \cdot & \cdots & [\mathbf{Z}^{[0]}_{\mathrm{PP}}]_{N_0\times N_0} \end{bmatrix}_{PN_0\times PN_0} \tag{5.14a}$$

$$\mathbf{V}^{[0]} = \begin{bmatrix} [\mathbf{V}^{[0]}_{1}]_{N_0\times 1} \\ [\mathbf{V}^{[0]}_{2}]_{N_0\times 1} \\ \vdots \\ [\mathbf{V}^{[0]}_{\mathrm{P}}]_{N_0\times 1} \end{bmatrix}_{PN_0\times 1} . \tag{5.14b}$$

As already been demonstrated for square patch and circular ring examples in the previous section, characteristic modes are utilized as Level-1 basis functions. Using the first N_1 characteristic modes of the impedance matrix $\mathbf{Z}^{[0]}_{\mathbf{pp}}$ which corresponds to any isolated element at Level-0, a set of Level-1 basis functions, $\mathbf{J}^{[1]}$, can be defined as

$$\mathbf{J}^{[1]} = \begin{bmatrix} [\mathbf{J}^{[1]}_{1}]_{N_0\times 1} & [\mathbf{J}^{[1]}_{2}]_{N_0\times 1} & \cdots & [\mathbf{J}^{[1]}_{N_1}]_{N_0\times 1} \end{bmatrix}_{N_0\times N_1} . \tag{5.15}$$

Therefore, the impedance matrix and the excitation vector at Level-1 can be expressed as

$$\mathbf{Z}^{[1]} = \begin{bmatrix} [\mathbf{Z}^{[1]}_{11}]_{N_1\times N_1} & [\mathbf{Z}^{[1]}_{12}]_{N_1\times N_1} & \cdots & [\mathbf{Z}^{[1]}_{1\mathrm{P}}]_{N_1\times N_1} \\ [\mathbf{Z}^{[1]}_{21}]_{N_1\times N_1} & [\mathbf{Z}^{[1]}_{22}]_{N_1\times N_1} & \cdots & \vdots \\ \vdots & \vdots & \ddots & \vdots \\ [\mathbf{Z}^{[1]}_{\mathrm{P}1}]_{N_1\times N_1} & \cdot & \cdots & [\mathbf{Z}^{[1]}_{\mathrm{PP}}]_{N_1\times N_1} \end{bmatrix}_{PN_1\times PN_1} \tag{5.16a}$$

$$\mathbf{V}^{[1]} = \begin{bmatrix} [\mathbf{V}^{[1]}_{1}]_{N_1\times 1} \\ [\mathbf{V}^{[1]}_{2}]_{N_1\times 1} \\ \vdots \\ [\mathbf{V}^{[1]}_{\mathrm{P}}]_{N_1\times 1} \end{bmatrix}_{PN_1\times 1} \tag{5.16b}$$

where sub-matrices and sub-vectors are calculated according to (5.17).

$$\mathbf{Z}^{[1]}_{pq} = {\mathbf{J}^{[1]}_{p}}^{T} \mathbf{Z}^{[0]}_{pq} \mathbf{J}^{[1]}_{q} \tag{5.17a}$$

$$\mathbf{V}^{[1]}_{p} = {\mathbf{J}^{[1]}_{p}}^{T} \mathbf{V}^{[0]}_{p} \tag{5.17b}$$

In the second level, the array is divided into blocks in which each block contains a group of array elements. Then the matrix reduction is done in the same way by treating each block as a single array element. Assuming that R is the number of blocks at Level-2 and each block contains equal number of array elements, the impedance matrix of Level-1 can also be represented as

$$\mathbf{Z}^{[1]} = \begin{bmatrix} [\mathbf{Z}^{[1]}_{11}]_{N_1' \times N_1'} & [\mathbf{Z}^{[1]}_{12}]_{N_1' \times N_1'} & \cdots & [\mathbf{Z}^{[1]}_{1\mathrm{R}}]_{N_1' \times N_1'} \\ [\mathbf{Z}^{[1]}_{21}]_{N_1' \times N_1'} & [\mathbf{Z}^{[1]}_{22}]_{N_1' \times N_1'} & \cdots & \vdots \\ \vdots & \vdots & \ddots & \vdots \\ [\mathbf{Z}^{[1]}_{\mathrm{R}1}]_{N_1' \times N_1'} & \cdot & \cdots & [\mathbf{Z}^{[1]}_{\mathrm{RR}}]_{N_1' \times N_1'} \end{bmatrix}_{RN_1' \times RN_1'} \tag{5.18}$$

where $N_1' = N_1 P/R$. In order to reduce the matrix in the second level, a set of basis functions is also defined at Level-2. In this stage, the basis functions are calculated as in the conventional CBFM. Hence, primary and secondary basis functions are calculated for the each block as

$$\mathbf{J}^{[2]}_r = \begin{bmatrix} [\mathbf{J}^{[2]}_1]_{N_1' \times 1} & [\mathbf{J}^{[2]}_2]_{N_1' \times 1} & \cdots & [\mathbf{J}^{[2]}_{N_{2,r}}]_{N_1' \times 1} \end{bmatrix}_{N_1' \times N_{2,r}} \quad , r = 1, 2, ..., R. \tag{5.19}$$

As a result, the reduced matrix and the excitation vector at Level-2 becomes

$$\mathbf{Z}^{[2]} = \begin{bmatrix} [\mathbf{Z}^{[2]}_{11}]_{N_{2,1} \times N_{2,1}} & [\mathbf{Z}^{[2]}_{12}]_{N_{2,1} \times N_{2,2}} & \cdots & [\mathbf{Z}^{[2]}_{1\mathrm{R}}]_{N_{2,1} \times N_{2,\mathrm{R}}} \\ [\mathbf{Z}^{[2]}_{21}]_{N_{2,2} \times N_{2,1}} & [\mathbf{Z}^{[2]}_{22}]_{N_{2,2} \times N_{2,2}} & \cdots & \vdots \\ \vdots & \vdots & \ddots & \vdots \\ [\mathbf{Z}^{[2]}_{\mathrm{R}1}]_{N_{2,\mathrm{R}} \times N_{2,1}} & \cdot & \cdots & [\mathbf{Z}^{[2]}_{\mathrm{RR}}]_{N_{2,\mathrm{R}} \times N_{2,\mathrm{R}}} \end{bmatrix}_{\left\{\sum\limits_{r=1}^{R} N_{2,\mathrm{r}}\right\} \times \left\{\sum\limits_{r=1}^{R} N_{2,\mathrm{r}}\right\}} \tag{5.20a}$$

$$\mathbf{V}^{[2]} = \begin{bmatrix} [\mathbf{V}^{[2]}_1]_{N_{2,1} \times 1} \\ [\mathbf{V}^{[2]}_2]_{N_{2,2} \times 1} \\ \vdots \\ [\mathbf{V}^{[2]}_{\mathrm{R}}]_{N_{2,\mathrm{R}} \times 1} \end{bmatrix}_{\left\{\sum\limits_{r=1}^{R} N_{2,\mathrm{r}}\right\} \times 1} \tag{5.20b}$$

where the sub-matrices and sub-vectors become

$$\mathbf{Z}^{[2]}_{pq} = \mathbf{J}^{[2]^T}_p \mathbf{Z}^{[1]}_{pq} \mathbf{J}^{[2]}_q \tag{5.21a}$$

$$\mathbf{V}^{[2]}_p = \mathbf{J}^{[2]^T}_p \mathbf{V}^{[1]}_p. \tag{5.21b}$$

5.4.1 Application of Multilevel Matrix Reduction

The proposed multilevel matrix reduction is performed on the 16×8 array of scaled ring elements shown in Fig. 5.12. The first level has already been demonstrated by treating each array element as a block and expanding characteristic modes as basis functions over the array elements. At level-2, the array is divided into 8 block where each block consists of 16 elements. The blocks at both levels are depicted in Fig. 5.13. At Level-1, 5 and 16 CMs are utilized as basis functions at 2 and 5 GHz, respectively. At Level-2, 2nd order neighboring is considered and the SVD threshold for the normalized singular values is set to 10^{-3}. The array is illuminated by normal and oblique plane wave incidences of $\theta_i = 0°, 30°$, and $60°$ as defined in (5.9). In Table 5.5, the relative error and the matrix size reduction are given at both levels at 2 and 5 GHz. It can be seen from the table that the size of the matrix is reduced from 8192×8192 to 56×56. In the first level, the error relative to Level-0 is less than $\%2$, whereas in the second level, the error relative to Level-1 becomes less than 8% for all different incidences. This example indicates that the proposed method can be utilized as an alternative to the conventional multilevel CBFM to exploit advantages of CM basis functions coming from their excitation-free nature and reusability on differently scaled elements. Further discussion on the multilevel matrix reduction using the characteristic modes is provided in Chapter 6.

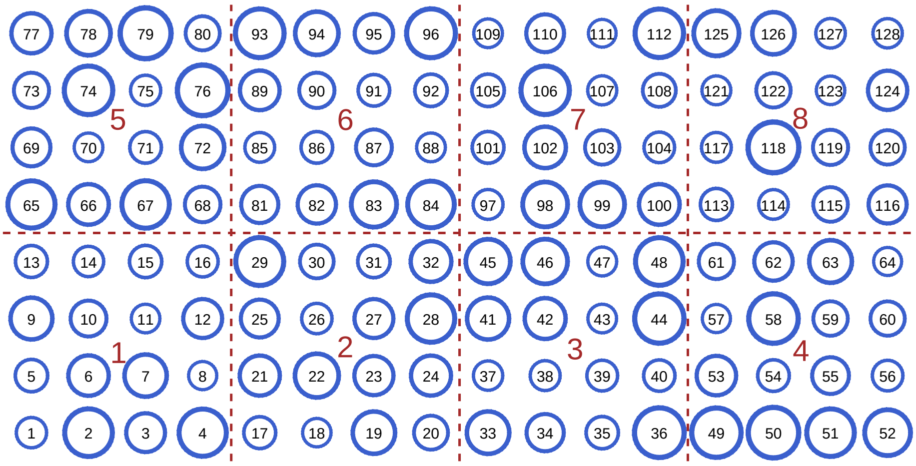

Figure 5.13: 128 blocks at Level-1 and 8 blocks at Level-2, defined for the 128-element array of differently sized circular rings.

Table 5.5: Multilevel matrix reduction for the 128-element array of differently sized circular rings.

Level	Matrix Size	f (GHz)	(θ_i, ϕ_i)	Relative Error (%)
$0 \rightarrow 1$	$8192 \times 8192 \rightarrow 640 \times 640$	2	$(0°, 0°)$	1.62
$1 \rightarrow 2$	$640 \times 640 \rightarrow 56 \times 56$	2	$(0°, 0°)$	6.57
$0 \rightarrow 1$	$8192 \times 8192 \rightarrow 640 \times 640$	2	$(30°, 0°)$	1.70
$1 \rightarrow 2$	$640 \times 640 \rightarrow 56 \times 56$	2	$(30°, 0°)$	7.75
$0 \rightarrow 1$	$8192 \times 8192 \rightarrow 640 \times 640$	2	$(60°, 0°)$	1.53
$1 \rightarrow 2$	$640 \times 640 \rightarrow 56 \times 56$	2	$(60°, 0°)$	7.67
$0 \rightarrow 1$	$8192 \times 8192 \rightarrow 2048 \times 2048$	5	$(0°, 0°)$	0.97
$1 \rightarrow 2$	$2048 \times 2048 \rightarrow 56 \times 56$	5	$(0°, 0°)$	7.10
$0 \rightarrow 1$	$8192 \times 8192 \rightarrow 2048 \times 2048$	5	$(30°, 0°)$	1.16
$1 \rightarrow 2$	$2048 \times 2048 \rightarrow 56 \times 56$	5	$(30°, 0°)$	3.55
$0 \rightarrow 1$	$8192 \times 8192 \rightarrow 2048 \times 2048$	5	$(60°, 0°)$	1.56
$1 \rightarrow 2$	$2048 \times 2048 \rightarrow 56 \times 56$	5	$(60°, 0°)$	4.08

CHAPTER 6

CONCLUSIONS

The characteristic mode analysis allows the current on any arbitrary surface to be evaluated as a weighted set of orthogonal modes. It mostly distinguishes from other modal analysis techniques due to the eigenvalues since they yield information about the resonant behavior of the modes. For this reason, the analysis of the characteristic modes provides valuable insight into the radiation and scattering problems. Therefore, it has become popular for antenna designers over the years. Characteristic mode analysis can be useful in a wide variety of antenna applications including phased array design, multiple-input-multiple-output (MIMO) systems, loaded array analysis and coupling reduction methods in finite arrays [63]. In recent years, the relationship of characteristic modes with spherical modes [22] and cavity modes have been investigated [23]. However, the periodic unit cell analysis has never been investigated using the theory of the characteristic modes. In this respect, this thesis study brings a new perspective to the unit cell solution and leads new approaches in the analysis and design of unit cell elements.

In order to calculate characteristic modes for the unit cell problem, an efficient formulation is developed. Due to the slow converging nature of both spatial domain and spectral domain periodic Green's functions, Ewald's transformation is incorporated into the solution. Hence, it paves the way for fast and effective analysis of the unit cell elements. Then, characteristic mode analysis of the FSS elements is performed. In the solution of Jerusalem Cross, first few characteristic modes show similar characteristics to the fundamental Floquet modes. Under normal incidence, modal significance and characteristic angle values correspond to the magnitude and phase of the reflected field, respectively. However, a more interesting phenomena occurs when the unit cell element is illuminated by an oblique incidence. In this case, a third characteristic mode emerges in the band of interest and changes the behavior of the reflection. Hence, the FSS element becomes dependent on angle of incidence. Nevertheless in the design of large periodic structures including FSSs, metamaterial absorbers and artificial impedance surfaces, one possible goal is to achieve polarization independence along with angle insensitivity. Thus, the angle independency can be provided only by preventing this additional characteristic mode resonating at the band of interest. In recent years, characteristic mode suppression techniques are demonstrated in antenna problems using inductive loads [46] and metasurface structures [47]. These methods can also be considered for the unit cell applications. Therefore, characteristic mode analysis of the unit cell element indicates a possible future work based on the CMA to make the unit cell element insensitive to the angle of incidence.

In the following analysis, metal-only reflectarray elements are examined. However this time, the modal analysis is not performed according to the frequency but the tuning parameters of the reflectarray element. Since the unit cell elements are backed by a ground plane, the structure can be thought of as a two-layer element. For this reason, 4 CMs are emerged. Since the aim in the design of reflectarray antennas is to acquire the desired aperture phase distribution, the phase range of the reflectarray unit cell element must be at least 360 degrees. Besides, in order to make reflectarray antenna less dependent on the production tolerances as well as the simulation inaccuracies, the phase response must change gradually with respect to the tuning parameter. Therefore for a proper design, it can be stated that the eigenvalues correspond to the excited modes must vary gradually and over a wide range with respect to the tuning parameter. This leads to the conclusion that characteristic modes can also be used in reflectarray element design. Therefore as a future study, a design methodology based on CMA can be adopted to obtain new reflectarray elements by adjusting the behavior of eigenvalues according to the tuning parameter. Since the characteristic mode analysis of the unit cell element is attempted for the first time, the examples are chosen out of simple and metal-only elements. Nevertheless, such analysis can also be extended for complex structures including multilayer metasurfaces, dielectric FSS elements and corrugated surfaces.

Undoubtedly, one of the most original contributions of this dissertation is the proposed method that calculates the required load values in advance to shift the reflection band of the ring-type FSS element to the desired band. In this method, first the reactive load matrix is calculated to change the resonance frequency of the mode-of-interest as desired. Then a novel approach is introduced that reduces the continuous load distribution into two capacitive or inductive loads. Since shifting the resonant frequency of the mode also means shifting the reflection coefficient, an original design method has emerged. It is shown that the developed method to obtain load values to have desired reflection band can be utilized for ring-type elements in different shapes, as well as for illuminations that propagate and polarize in different directions. Hence instead of assigning load values as unknown variables and running complex optimization algorithms, applying the characteristic mode analysis on the unloaded ring elements seem sufficient to find the load values that shift the reflection band to desired frequencies. Especially in the design of FSS elements that consist of multiple ring elements, the optimization algorithms would become very cumbersome, especially when there are multiple rings in the same unit cell. However, the developed method also works well on the unit cell elements that consist of multiple rings placed concentrically or placed in different layers. In the ring-type slot problem, solving the conducting surface rather than solving only the slot region would increase the computational cost drastically. Hence considering the complementary problem and solving only the complementary unloaded slot element once to find desired load values would be very advantageous in terms of time and cost. For all these reasons, the theory of characteristic mode theory has been exploited efficiently in the design of ring-type reactively loaded FSS elements.

After having successfully demonstrated the method for the ring-type FSS elements, the next step would be to develop the same method for different periodic geometries that are not ring-shaped. In fact, although the goal in this thesis work is to develop this method for periodic structures, a similar approach can also be considered in antenna problems with the help of the characteristic modes.

In the last part of the dissertation, an additional study is demonstrated that differs from the rest of the thesis study since the CMA is not applied on unit cell elements, but on isolated array elements at the open boundaries. Then the characteristic modes on an array element is utilized as a macro basis function on the entire array. In the context of the macro basis function approach, the use of characteristic modes is discussed as basis functions. Although excitation-independent CBFM techniques are available in the literature [100,101], excitation independent nature of the characteristic modes still become advantageous due to the fact that no prior knowledge regarding the excitation is needed in the construction of macro basis functions. Besides that, unlike the CBFM approach, the same modes can also be used as basis functions on the array elements of different sizes. This is successfully demonstrated in the example of reflectarray with differently sized elements.

As an original approach, the characteristic modes are treated as primary basis functions in the context of CBFM and secondary basis functions are included into the solution. Although less modes are needed in order to reduce the relative error compared to the solution where only CMs are used as basis functions, a large number of MBFs is still needed in both solutions especially at higher frequencies. Because the matrix size increases as the number of MBFs increases, the multilevel matrix reduction approach is proposed by utilizing characteristic modes at the first level and applying the conventional CBFM at the second level. In this multilevel solution, CM basis functions can also be calculated and used at the second level. However such a solution would decrease the accuracy unless most of the modes calculated at the second level are incorporated into the solution. Hence at the second level, implementing the conventional CBFM is considered. The downside of this approach is that the basis functions at the second level become dependent on the excitation. However, the first level is still independent of the excitation. Therefore, the reduced matrix of the first level can still be stored and reused for different excitations. Since filling the reduced matrix at the first level is time-consuming, using excitation independent basis functions only at the first level would still be more advantageous than using excitation-dependent basis functions at the both levels. To be able to fill the reduced matrix efficiently, several methods including the ACA algorithm [106] can be incorporated into the solution. Recently, a tabulation method is also presented in [21] for scaled reflectarray elements. As the main purpose of Chapter 5 is to present a discussion about the matrix reduction approach using the characteristic modes, application of these methods are left to the reader. In this chapter, computational aspects of the reduced matrix approach is successfully demonstrated and new approaches are proposed using characteristic modes as basis functions.

As a conclusion, an efficient analysis of periodic structures is demonstrated with the help of characteristic modes. This thesis work not only introduces new approaches and design methodologies, but also brings new perspectives to the study of periodic structures with the help of the characteristic modes.

REFERENCES

[1] B. Munk, *Frequency Selective Surfaces: Theory and Design*. Wiley, 2005.

[2] G. Guida and A. Priou, “An introduction to photonic band gap (PBG) materials,” *Progress in Electromagnetics Research*, vol. 41, pp. 1–20, 01 2003.

[3] J. Huang and J. Encinar, *Reflectarray Antennas*, ser. IEEE Press Series on Electromagnetic Wave Theory. Wiley, 2007.

[4] T. Eibert, J. Volakis, D. Wilton, and D. Jackson, “Hybrid FE/BI modeling of 3-D doubly periodic structures utilizing triangular prismatic elements and an MPIE formulation accelerated by the Ewald transformation,” *IEEE Transactions on Antennas and Propagation*, vol. 47, no. 5, pp. 843–850, 1999.

[5] R. F. Harrington, *Field Computation by Moment Methods*. IEEE Press, 1993.

[6] S. Rao, D. Wilton, and A. Glisson, “Electromagnetic scattering by surfaces of arbitrary shape,” *IEEE Transactions on Antennas and Propagation*, vol. 30, no. 3, pp. 409–418, May 1982.

[7] K. E. Jordan, G. R. Richter, and P. Sheng, “An Efficient Numerical Evaluation of the Green’s Function for the Helmholtz Operator on Periodic Structures,” *Journal of Computational Physics*, vol. 63, pp. 222–235, Mar. 1986.

[8] R. Harrington and J. Mautz, “Theory of characteristic modes for conducting bodies,” *IEEE Transactions on Antennas and Propagation*, vol. 19, no. 5, pp. 622–628, Sep 1971.

[9] ——, “Computation of characteristic modes for conducting bodies,” *IEEE Transactions on Antennas and Propagation*, vol. 19, no. 5, pp. 629–639, Sep 1971.

[10] R. Harrington and J. Mautz, “Control of radar scattering by reactive loading,” *IEEE Transactions on Antennas and Propagation*, vol. 20, no. 4, pp. 446–454, 1972.

[11] R. Harrington and J. Mautz, “Optimization of radar cross section of N-port loaded scatterers,” *IEEE Transactions on Antennas and Propagation*, vol. 22, no. 5, pp. 697–701, 1974.

[12] ——, “Pattern synthesis for loaded N-port scatterers,” *IEEE Transactions on Antennas and Propagation*, vol. 22, no. 2, pp. 184–190, 1974.

[13] R. Harrington, “Reactively controlled directive arrays,” *IEEE Transactions on Antennas and Propagation*, vol. 26, no. 3, pp. 390–395, 1978.

[14] K. A. Obeidat, B. D. Raines, and R. G. Rojas, “Application of characteristic modes and non-foster multiport loading to the design of broadband antennas,” *IEEE Transactions on Antennas and Propagation*, vol. 58, no. 1, pp. 203–207, 2010.

[15] C. Craeye, J. Laviada, R. Maaskant, and R. Mittra, “Macro basis function framework for solving Maxwell’s equations in surface integral equation form,” in *Forum for Electromagnetic Research Methods and Application Technologies (FERMAT)*, 2014.

[16] V. V. S. Prakash and R. Mittra, “Characteristic basis function method: A new technique for efficient solution of method of moments matrix equations,” *Microwave and Optical Technology Letters*, vol. 36, no. 2, pp. 95–100, 2003.

[17] R. Mittra and K. Du, “Characteristic basis function method for iteration-free solution of large method of moments problems,” *Progress in Electromagnetics Research B*, vol. 6, pp. 307–336, 01 2008.

[18] R. Maaskant, R. Mittra, and A. Tijhuis, “Multilevel characteristic basis function method (MLCBFM) for the analysis of large antenna arrays,” *URSI Radio Science Bulletin*, vol. 2011, no. 336, pp. 23–34, 2011.

[19] J. Laviada, F. Las-Heras, M. R. Pino, and R. Mittra, “Solution of electrically large problems with multilevel characteristic basis functions,” *IEEE Transactions on Antennas and Propagation*, vol. 57, no. 10, pp. 3189–3198, 2009.

[20] G. Angiulli, G. Amendola, and G. Di Massa, “Application of characteristic modes to the analysis of scattering from microstrip antennas,” *Journal of Electromagnetic Waves and Applications*, vol. 14, pp. 1063–1081, 01 2000.

[21] E. Ercil, L. Alatan, and O. A. Civi, “An efficient numerical solution method for reflectarrays of varying element sizes,” *IEEE Transactions on Antennas and Propagation*, vol. 63, no. 12, pp. 5668–5676, Dec 2015.

[22] J. Adams, “Exploiting patterns in characteristic modes for efficient analytical and numerical modeling,” in *Antenna Applications Symposium*, September 2013.

[23] K. A. Obeidat, B. D. Raines, and R. G. Rojas, “Discussion of series and parallel resonance phenomena in the input impedance of antennas,” *Radio Science*, vol. 45, no. 06, pp. 1–9, 2010.

[24] M. Cabedo-Fabres, E. Antonino-Daviu, A. Valero-Nogueira, and M. F. Bataller, “The theory of characteristic modes revisited: A contribution to the design of antennas for modern applications,” *IEEE Antennas and Propagation Magazine*, vol. 49, no. 5, pp. 52–68, Oct 2007.

[25] A. Glisson and D. Wilton, “Simple and efficient numerical methods for problems of electromagnetic radiation and scattering from surfaces,” *IEEE Transactions on Antennas and Propagation*, vol. 28, no. 5, pp. 593–603, 1980.

[26] Website: https://www.mathworks.com/products/matlab-coder.html, 2021.

[27] D. A. Dunavant, “High degree efficient symmetrical Gaussian quadrature rules for the triangle,” *International Journal for Numerical Methods in Engineering*, vol. 21, no. 6, pp. 1129–1148, 1985.

[28] D. Wilton, S. Rao, A. Glisson, D. Schaubert, O. Al-Bundak, and C. Butler, “Potential integrals for uniform and linear source distributions on polygonal and polyhedral domains,” *IEEE Transactions on Antennas and Propagation*, vol. 32, no. 3, pp. 276–281, Mar 1984.

[29] W. Gibson, *The Method of Moments in Electromagnetics*. CRC Press, 2007.

[30] Website: https://docs.plm.automation.siemens.com/tdoc/nx/, 2021.

[31] C. Balanis, *Advanced Engineering Electromagnetics, 2nd Edition*. Wiley, 2012.

[32] Y. Chen and C. Wang, *Characteristic Modes: Theory and Applications in Antenna Engineering*. Wiley, 2015.

[33] FEKO Suite 14.0, http://www.altairhyperworks.com.

[34] Website: http://www.characteristicmodes.org, 2022.

[35] Y. Chen, K. Schab, M. Čapek, M. Mašek, B. K. Lau, H. Aliakbari, Y. Haykir, Q. Wu, W. J. Strydom, N. Peitzmeier, M. Jovicic, S. Genovesi, and F. A. Dicandia, "Benchmark problem definition and cross-validation for characteristic mode solvers," in *12th European Conference on Antennas and Propagation (EuCAP 2018)*, 2018, pp. 1–5.

[36] A. Maalik, R. G. Rojas, and R. J. Burkholder, "Characteristic modal decomposition of reflection phase of a microstrip-patch reflectarray unit-cell," in *2016 IEEE International Symposium on Antennas and Propagation (APSURSI)*, June 2016, pp. 425–426.

[37] C.-C. Chen, "Transmission through a conducting screen perforated periodically with apertures," *IEEE Transactions on Microwave Theory and Techniques*, vol. 18, no. 9, pp. 627–632, Sep 1970.

[38] ——, "Scattering by a two-dimensional periodic array of conducting plates," *IEEE Transactions on Antennas and Propagation*, vol. 18, no. 5, pp. 660–665, Sep 1970.

[39] A. Bhattacharyya, *Phased Array Antennas: Floquet Analysis, Synthesis, BFNs and Active Array Systems*, ser. Wiley Series in Microwave and Optical Engineering. Wiley, 2006.

[40] S. Singh, W. Richards, J. Zinecker, and D. Wilton, "Accelerating the convergence of series representing the free space periodic Green's function," *IEEE Transactions on Antennas and Propagation*, vol. 38, no. 12, pp. 1958–1962, 1990.

[41] S. Makarov, *Antenna and EM Modeling with Matlab*. Wiley-Interscience, 2002.

[42] S. Oroskar, D. R. Jackson, and D. R. Wilton, “Efficient computation of the 2D periodic green’s function using the Ewald method,” *Journal of Computational Physics*, vol. 219, no. 2, pp. 899–911, 2006.

[43] P. Jorna, V. Lancellotti, and M. C. van Beurden, “Computational aspects of 2D-quasi-periodic-Green-function computations for scattering by dielectric objects via surface integral equations,” *Progress In Electromagnetics Research B*, vol. 63, pp. 49–66, 2015.

[44] I. Stevanovic, P. Crespo-Valero, K. Blagovic, F. Bongard, and J. R. Mosig, “Integral-equation analysis of 3-D metallic objects arranged in 2-D lattices using the Ewald transformation,” *IEEE Transactions on Microwave Theory and Techniques*, vol. 54, no. 10, pp. 3688–3697, Oct 2006.

[45] J.X. Su, X.W. Xu, M. He, K. Zhang, “Integral-equation analysis of frequency selective surfaces using Ewald transformation and lattice symmetry,” *Progress In Electromagnetics Research*, vol. 121, pp. 249–269, 2011.

[46] Q. Wu, W. Su, Z. Li, and D. Su, “Reduction in out-of-band antenna coupling using characteristic mode analysis,” *IEEE Transactions on Antennas and Propagation*, vol. 64, no. 7, pp. 2732–2742, July 2016.

[47] A. A. Salih, Z. N. Chen, and K. Mouthaan, “Characteristic mode analysis and metasurface-based suppression of higher order modes of a 2×2 closely spaced phased array,” *IEEE Transactions on Antennas and Propagation*, vol. 65, no. 3, pp. 1141–1150, March 2017.

[48] E. Carrasco and J. Encinar, “Reflectarray antennas : A review,” 2016.

[49] Y. Haykir and O. A. Civi, “Characteristic mode analysis of unit cells of metal-only infinite arrays,” *Advanced Electromagnetics*, vol. 8, no. 2, p. 134–142, Sep. 2019.

[50] ——, “Characteristic mode analysis of reflectarray unit cell,” in *12th European Conference on Antennas and Propagation (EuCAP 2018)*, 2018, pp. 1–4.

[51] R. Deng, F. Yang, S. Xu, and M. Li, “A low-cost metal-only reflectarray using modified slot-type Phoenix element with 360° phase coverage,” *IEEE Trans-*

actions on Antennas and Propagation, vol. 64, no. 4, pp. 1556–1560, April 2016.

[52] L. Moustafa, R. Gillard, F. Peris, R. Loison, H. Legay, and E. Girard, "The Phoenix cell: A new reflectarray cell with large bandwidth and rebirth capabilities," *IEEE Antennas and Wireless Propagation Letters*, vol. 10, pp. 71–74, 2011.

[53] J. Schindler, R. Mack, and P. Blacksmith, "The control of electromagnetic scattering by impedance loading," *Proceedings of the IEEE*, vol. 53, no. 8, pp. 993–1004, 1965.

[54] K. Chen and V. Liepa, "The minimization of the back scattering of a cylinder by central loading," *IEEE Transactions on Antennas and Propagation*, vol. 12, no. 5, pp. 576–582, 1964.

[55] K.-M. Chen, "Minimization of backscattering of a cylinder by double loading," *IEEE Transactions on Antennas and Propagation*, vol. 13, no. 2, pp. 262–270, 1965.

[56] J.-L. Lin and K.-M. Chen, "Minimization of backscattering of a loop by impedance loading–theory and experiment," *IEEE Transactions on Antennas and Propagation*, vol. 16, no. 3, pp. 299–304, 1968.

[57] D. Seth and Y. Chow, "On linear parasitic array of dipoles with reactive loading," *IEEE Transactions on Antennas and Propagation*, vol. 21, no. 3, pp. 286–292, 1973.

[58] R. Li, V. Fusco, and R. Cahill, "Pattern shaping using a reactively loaded wire loop antenna," *Microwaves, Antennas and Propagation, IEE Proceedings -*, vol. 148, pp. 203 – 208, 07 2001.

[59] H. Scott and V. Fusco, "Electronic beam tilting using a single reactively loaded circular wire loop antenna," *Microwaves, Antennas and Propagation, IEE Proceedings -*, vol. 149, pp. 271 – 274, 11 2002.

[60] W. Richards, S. Davidson, and S. Long, "Dual-band reactively loaded microstrip antenna," *IEEE Transactions on Antennas and Propagation*, vol. 33, no. 5, pp. 556–561, 1985.

[61] S. Maci, G. Biffi Gentili, P. Piazzesi, and C. Salvador, “Dual-band slot-loaded patch antenna,” *IEE Proceedings - Microwaves, Antennas and Propagation*, vol. 142, pp. 225–232, June 1995.

[62] A. Ali-Khan, W. Richards, and S. Long, “Impedance control of microstrip antennas using reactive loading,” *IEEE Transactions on Antennas and Propagation*, vol. 37, no. 2, pp. 247–251, 1989.

[63] M. C. Fabres, “Systematic design of antennas using the theory of characteristic modes,” Ph.D. dissertation, Polytechnic University of Valencia, 2007.

[64] R. F. Harrington, “Theory of loaded scatterers,” *Proceedings of the Institution of Electrical Engineers*, vol. 111, pp. 617–623(6), April 1964.

[65] J. Mautz and R. Harrington, “Modal analysis of loaded N-port scatterers,” *IEEE Transactions on Antennas and Propagation*, vol. 21, no. 2, pp. 188–199, 1973.

[66] K. Kumar Kishor and S. V. Hum, “A pattern reconfigurable chassis-mode mimo antenna,” *IEEE Transactions on Antennas and Propagation*, vol. 62, no. 6, pp. 3290–3298, 2014.

[67] E. Safin and D. Manteuffel, “Manipulation of characteristic wave modes by impedance loading,” *IEEE Transactions on Antennas and Propagation*, vol. 63, no. 4, pp. 1756–1764, 2015.

[68] H. Jaafar, S. Collardey, and A. Sharaiha, “Optimized manipulation of the network characteristic modes for wideband small antenna matching,” *IEEE Transactions on Antennas and Propagation*, vol. 65, no. 11, pp. 5757–5767, 2017.

[69] M. Khan and D. Chatterjee, “Analysis of reactive loading in a u-slot microstrip patch using the theory of characteristic modes,” *IEEE Antennas and Propagation Magazine*, vol. 60, no. 6, pp. 88–97, 2018.

[70] R. Langley, “Equivalent circuit model for arrays of square loops,” *Electronics Letters*, vol. 18, pp. 294–296(2), April 1982.

[71] S. Savia, “Equivalent circuit model for superdense linear dipole FSS,” *IEE*

Proceedings - Microwaves, Antennas and Propagation, vol. 150, pp. 37–42(5), February 2003.

[72] C.-H. Tsao and R. Mittra, “Spectral-domain analysis of frequency selective surfaces comprised of periodic arrays of cross dipoles and Jerusalem crosses,” *IEEE Transactions on Antennas and Propagation*, vol. 32, no. 5, pp. 478–486, 1984.

[73] R. Langley, “Improved empirical model for the Jerusalem cross,” *IEE Proceedings H (Microwaves, Optics and Antennas)*, vol. 129, pp. 1–6(5), February 1982.

[74] F. Costa, A. Monorchio, and G. Manara, “Efficient analysis of frequency-selective surfaces by a simple equivalent-circuit model,” *IEEE Antennas and Propagation Magazine*, vol. 54, no. 4, pp. 35–48, 2012.

[75] B. S. da Silva, A. L. P. d. S. Campos, and A. G. Neto, “Equivalent circuit model for analysis of frequency selective surfaces with ring and double concentric ring apertures,” *IET Microwaves, Antennas & Propagation*, vol. 14, no. 7, pp. 600–607, 2020.

[76] R. Langley, “Double-square frequency-selective surfaces and their equivalent circuit,” *Electronics Letters*, vol. 19, pp. 675–677(2), August 1983.

[77] X. Yao, M. Bai, and J. Miao, “Equivalent circuit method for analyzing frequency selective surface with ring patch in oblique angles of incidence,” *IEEE Antennas and Wireless Propagation Letters*, vol. 10, pp. 820–823, 2011.

[78] T.-K. Wu, “Four-band frequency selective surface with double-square-loop patch elements,” *IEEE Transactions on Antennas and Propagation*, vol. 42, no. 12, pp. 1659–1663, 1994.

[79] X.-D. Hu, X.-L. Zhou, L.-S. Wu, L. Zhou, and W.-Y. Yin, “A miniaturized dual-band frequency selective surface (FSS) with closed loop and its complementary pattern,” *IEEE Antennas and Wireless Propagation Letters*, vol. 8, pp. 1374–1377, 2009.

[80] V. K. Kanth and S. Raghavan, “Complementary frequency selective surface array optimization using equivalent circuit model,” in *2017 IEEE MTT-S International Microwave and RF Conference (IMaRC)*, 2017, pp. 1–4.

[81] Y. Cui, S. Zhang, M. Wang, J. Liu, X. Liu, and Y. Wang, “A novel tunable FSS of miniaturized unit cell for lower frequency,” in *2018 International Applied Computational Electromagnetics Society Symposium - China (ACES)*, 2018, pp. 1–2.

[82] T. Wei, G. Zhang, J. Ding, and C. Guo, “A novel tunable wide-band fss with varactors,” in *2017 International Applied Computational Electromagnetics Society Symposium (ACES)*, 2017, pp. 1–2.

[83] F. J. L. Vez, J. Rodriguez-Cuevas, A. E. Martynyuk, and J. I. Martinez-Lopez, “Active frequency selective surfaces based on loaded ring patches,” in *2018 IEEE International Conference on Computational Electromagnetics (ICCEM)*, 2018, pp. 1–2.

[84] D. Cure, T. Weller, F. Miranda, and P. Herzig, “One dimensional capacitive loading in a frequency selective surface for low profile antenna applications,” in *2011 IEEE International Symposium on Antennas and Propagation (APSURSI)*, 2011, pp. 2258–2261.

[85] M. Titaouine, A. Neto, H. Baudrand, and F. Djahli, “WCIP method applied to active frequency selective surfaces,” *Journal of Microwaves and Optoelectronics*, vol. 6, pp. 1–16, 06 2007.

[86] P. S. Taylor, E. A. Parker, and J. C. Batchelor, “An active annular ring frequency selective surface,” *IEEE Transactions on Antennas and Propagation*, vol. 59, no. 9, pp. 3265–3271, 2011.

[87] N. Liu, X. Sheng, C. Zhang, J. Fan, and D. Guo, “A design method for synthesizing miniaturized FSS using lumped reactive components,” *IEEE Transactions on Electromagnetic Compatibility*, vol. 60, no. 2, pp. 536–539, 2018.

[88] R. Harrington and J. Mautz, “Characteristic modes for aperture problems,” *IEEE Transactions on Microwave Theory and Techniques*, vol. 33, no. 6, pp. 500–505, 1985.

[89] K. Kabalan, R. Harrington, H. Auda, and J. Mautz, "Characteristic modes for slots in a conducting plane, TE case," *IEEE Transactions on Antennas and Propagation*, vol. 35, no. 2, pp. 162–168, 1987.

[90] K. Kabalan, R. Harrington, J. Mautz, and H. Auda, "Characteristic modes for a slot in a conducting plane, TM case," *IEEE Transactions on Antennas and Propagation*, vol. 35, no. 3, pp. 331–335, 1987.

[91] A. El-Hajj and K. Kabalan, "Characteristic modes of a rectangular aperture in a perfectly conducting plane," *IEEE Transactions on Antennas and Propagation*, vol. 42, no. 10, pp. 1447–1450, 1994.

[92] N. M. Mohamed-Hicho, E. Antonino-Daviu, M. Cabedo-Fabrés, J. P. Ciafardini, J. A. Bava, and M. Ferrando-Bataller, "Characteristic modes of slotted planar antennas," in *2017 11th European Conference on Antennas and Propagation (EUCAP)*, 2017, pp. 2668–2672.

[93] P. Liang and Q. Wu, "Duality principle of characteristic modes for the analysis and design of aperture antennas," *IEEE Transactions on Antennas and Propagation*, vol. 66, no. 6, pp. 2807–2817, 2018.

[94] P. Liang, Q. Wu, and D. Su, "Characteristic mode analysis of aperture antennas based on duality principle," in *2017 11th European Conference on Antennas and Propagation (EUCAP)*, 2017, pp. 2993–2997.

[95] G. Paul, K. Mandal, J. Acharjee, and P. Sarkar, "Reduction of mobile phone radiation exposure using multi-stopband frequency selective surface," *Progress In Electromagnetics Research M*, vol. 83, pp. 9–18, 07 2019.

[96] R. Coifman, V. Rokhlin, and S. Wandzura, "The fast multipole method for the wave equation: a pedestrian prescription," *IEEE Antennas and Propagation Magazine*, vol. 35, no. 3, pp. 7–12, 1993.

[97] W. Chew, J. Jin, E. Michielssen, and J. Song, *Fast and Efficient Algorithms in Computational Electromagnetics*, ser. Antennas and Propagation Library. Artech House, 2001.

[98] E. Bleszynski, M. Bleszynski, and T. Jaroszewicz, "AIM: Adaptive integral method for solving large-scale electromagnetic scattering and radiation problems," *Radio Science*, vol. 31, no. 5, pp. 1225–1251, 1996.

[99] K. Zhao, M. N. Vouvakis, and J. F. Lee, "The adaptive cross approximation algorithm for accelerated method of moments computations of EMC problems," *IEEE Transactions on Electromagnetic Compatibility*, vol. 47, no. 4, pp. 763–773, Nov 2005.

[100] E. Lucente, G. TIBERI, A. Monorchio, G. Manara, and R. Mittra, "The characteristic basis function method (CBFM): A numerically efficient strategy for solving large electromagnetic scattering problems," *Turkish Journal of Electrical Engineering and Computer Sciences*, vol. 16, 01 2008.

[101] E. Lucente, A. Monorchio, and R. Mittra, "An iteration-free mom approach based on excitation independent characteristic basis functions for solving large multiscale electromagnetic scattering problems," *IEEE Transactions on Antennas and Propagation*, vol. 56, no. 4, pp. 999–1007, 2008.

[102] D. J. Ludick, M. M. Botha, R. Maaskant, and D. B. Davidson, "The CBFM-enhanced Jacobi method for efficient finite antenna array analysis," *IEEE Antennas and Wireless Propagation Letters*, vol. 16, pp. 2700–2703, 2017.

[103] D. J. Ludick, M. M. Botha, R. Maaskant, and D. B. Davidson, "Accelerating the CBFM-enhanced jacobi method," in *2017 International Conference on Electromagnetics in Advanced Applications (ICEAA)*, 2017, pp. 346–349.

[104] D. J. Ludick, R. Maaskant, R. Mittra, U. Jakobus, and D. B. Davidson, "Applying the CBFM-enhanced domain Green's function method to the analysis of large disjoint subarray antennas," in *2013 International Conference on Electromagnetics in Advanced Applications (ICEAA)*, 2013, pp. 94–97.

[105] F. Catedra, E. Garcia, C. Delgado, F. S. de Adana, and R. Mittra, "Development of an efficient rigorous technique based on the combination of CBFM and MLFMA to solve very large electromagnetic problems," in *2007 International Conference on Electromagnetics in Advanced Applications*, 2007, pp. 579–582.

[106] R. Maaskant, R. Mittra, and A. Tijhuis, “Fast analysis of large antenna arrays using the characteristic basis function method and the adaptive cross approximation algorithm,” *IEEE Transactions on Antennas and Propagation*, vol. 56, no. 11, pp. 3440–3451, 2008.

[107] J. Laviada, M. R. Pino, F. Las-Heras, and R. Mittra, “Efficient calculation of the reduced matrix in the characteristic basis functions method,” in *2008 IEEE Antennas and Propagation Society International Symposium*, 2008, pp. 1–4.

[108] G. S. Cheng and C.-F. Wang, “A novel periodic characteristic mode analysis method for large-scale finite arrays,” *IEEE Transactions on Antennas and Propagation*, vol. 67, no. 12, pp. 7637–7642, 2019.

[109] Y. Haykir and O. A. Civi, “Use of characteristic modes in the CBFM for the analysis of large arrays,” in *2020 14th European Conference on Antennas and Propagation (EuCAP)*, 2020, pp. 1–4.

[110] G. H. Golub and C. Reinsch, “Singular value decomposition and least squares solutions,” *Numerische Mathematik*, vol. 14, p. 403–420, 1970.

CURRICULUM VITAE

Surname, Name: Haykır, Yiğit

EDUCATION

Degree	Institution	Year of Graduation
MS	Hacettepe University Electrical and Electronics Engineering	2015
BS	Bilkent University Electrical and Electronics Engineering	2011

FOREIGN LANGUAGES

Advanced English

PUBLICATIONS

1. Y. Haykir, A. Kallem and S. Demir, “Compact and directional printed dipole antenna pair conformed on a conical surface,” XXXIVth General Assembly and Scientific Symposium of the International Union of Radio Science (URSI GASS), pp. 1-4, 2021.

2. Y. Haykir and S. Demir, “A low-profile dielectric waveguide altimeter antenna,” XXXIIIrd General Assembly and Scientific Symposium of the International Union of Radio Science, pp. 1-3, 2020.

3. Y. Haykir and O. A. Civi, “Use of Characteristic Modes in the CBFM for the Analysis of Large Arrays,” 14th European Conference on Antennas and Propagation (EuCAP), pp. 1-4., 2020.

4. Y. Haykir and O. A. Civi, “Characteristic mode analysis of unit cells of metal-only infinite arrays,”Advanced Electromagnetics Journal, Jan, 2019.

5. Y. Haykir, S. Karadag and S. Demir, “Design and implementation of transmitting and receiving antenna pair on flat ring surface,” 18th Mediterranean Microwave Symposium (MMS), pp. 36-381, 2018.

6. Y. Haykir and O. A. Civi, “Periyodik birim hücresi karakteristik mod çözümlemesi,”URSI-TÜRKİYE 2018 IX. Bilimsel Kongresi, Konya, 2018.

7. Y.Chen, K. Schab, M. Čapek, M. Mašek, B. K. Lau, H. Aliakbari, Y. Haykir, Q. Wu, W.J. Strydom, N. Peitzmeier, M. Jovicic, S. Genovesi, F. A. Dicandia, “Benchmark problem definition and crossvalidation for characteristic mode solvers,” 12th European Conference on Antennas and Propagation (EuCAP), London, 2018.

8. Y. Haykir and O. A. Civi, “Characteristic mode analysis of reflectarray unit cell,” 12th European Conference on Antennas and Propagation (EuCAP 2018), pp. 1-4., 2018.

9. Y. Haykir and A. Köksal, “A novel singularity-free analysis of coaxial-fed thick monopole antennas,”IEEE Transactions on Antennas and Propagation, vol.63, no. 12, pp. 5860-5863, Dec. 2015.

10. Y. Haykir and A. Köksal, “A new approach for the analysis of thick wire antennas,” Antennas and Propagation & USNC/URSI National Radio Science Meeting, 2015 IEEE International Symposium, pp. 963-964, 19-24 July 2015.